DISSERTATION

SINGLE-CELL QUANTIFICATION AND STOCHASTIC MODELING OF GLUCOCORTICOID RECEPTOR TRANSPORT AND DUSP1 MRNA DYNAMICS

Submitted by

Eric M. Ron

School of Biomedical and Chemical Engineering

In partial fulfillment of the requirements

For the Degree of Doctor of Philosophy

Colorado State University

Fort Collins, Colorado

Summer 2026

Doctoral Committee:

Advisor: Brian Munsky

Tim J. Stasevich
Brian J. Geiss
Tai A. Montgomery

Copyright by Eric M. Ron 2026

All Rights Reserved

ABSTRACT

SINGLE-CELL QUANTIFICATION AND STOCHASTIC MODELING OF GLUCOCORTICOID RECEPTOR TRANSPORT AND DUSP1 MRNA DYNAMICS

The work presented in this dissertation combines quantitative single-cell experimentation with mathematical modeling to investigate glucocorticoid receptor (GR) signaling and the transcriptional regulation of the glucocorticoid-responsive gene Dual-Specificity Phosphatase 1 (DUSP1). The overall objective is to establish experimentally constrained, predictive models that describe how GR localization dynamics are linked to transcriptional activation and mRNA abundance at the single-cell level.

First, quantitative immunocytochemistry (ICC) and single-cell image analysis are used to characterize GR nucleocytoplasmic transport following glucocorticoid (GC) stimulation. Analysis of GR localization dynamics across individual cells indicates that nuclear clearance processes, rather than sustained cytoplasmic recycling, modulate nuclear GR levels. These observations restrict the class of GR transport and degradation models that are consistent with the data and emphasize the importance of nuclear turnover in shaping GR localization.

Second, endogenous DUSP1 transcriptional activity is quantified using single-molecule inexpensive RNA fluorescence in situ hybridization (smiFISH), enabling direct measurement of transcription site activity and mRNA distributions across single cells. Utilizing a chemical master equation framework, we have developed a discrete stochastic model that accurately reproduces the time-varying probability distributions of GR and DUSP1 spatiotemporal dynamics – at all times and across multiple Dex concentrations. Stochastic two-state promoter models are developed to interpret these data. Model comparisons indicate that the observed transcriptional activation of DUSP1 can be reproduced by changes in promoter switching dynamics, specifically through increased promoter activation rates, decreased promoter deactivation rates, or combinations of both.

These results suggest that modulation of transcriptional bursting provides a mechanistic explanation for the observed transcriptional response.

Third, cytoplasmic DUSP1 mRNA accumulation is examined in the context of transcription, nuclear export, and mRNA decay. Quantitative analysis supports a model in which cytoplasmic mRNA levels reflect a balance between mRNA production and export and AU-rich element-mediated decay processes. Incorporating these regulatory steps into a unified modeling framework improves agreement with experimentally observed cytoplasmic mRNA distributions and temporal dynamics.

Together, this work provides a quantitative description of GR localization dynamics, DUSP1 transcriptional activation, and post-transcriptional regulation using endogenous single-cell measurements. The resulting models establish a foundation for future studies aimed at extending these approaches to more complex regulatory interactions and perturbations in GC signaling.

ACKNOWLEDGEMENTS

Thanks to my advisor Brian Munsky, committee members, collaborators in the Munsky and Stasevich labs, the DeLuca Lab for the HeLa Kyoto cells, undergraduates and trainees, the q-bio summer school community, funding sources, and family. Figures in this dissertation were created or compiled using BioRender (biorender.com)

DEDICATION

To Haley, my future wife, for her love, patience, and partnership.

To my family: my mother Betty Petrak-Ron, my father Odie Ron, my brothers Jason and Ian Ron, and my uncle John Petrak, for a lifetime of support and for the foundation on which everything that follows was built.

To Daisy, for the insomniac comforts that only a cat can provide.

And in loving memory of those lost during this work: my grandfather Gershon Ron, my grandmother Anna Petrak, and my friends "Action" Jack Miller and Blake Geissbuhler.

TABLE OF CONTENTS

ABSTRACT ii
ACKNOWLEDGEMENTS iv
DEDICATION v
LIST OF TABLES ix
LIST OF FIGURES x

Chapter 1 Quantitative and Mechanistic Foundations of Glucocorticoid Receptor Signaling and DUSP1 Regulation 1
1.1 Glucocorticoids in Inflammation: Necessity and Limitations 1
1.1.1 The burden of acute and chronic inflammatory disease 1
1.1.2 MAPK Signaling as a Central Amplifier of Inflammatory Responses . . 5
1.1.3 Negative regulation and homeostatic control of inflammation 7
1.1.4 Glucocorticoids as broad-spectrum anti-inflammatory therapy 8
1.1.5 Clinical limitations motivating mechanistic resolution 10
1.2 The glucocorticoid receptor: structure, transport, and regulation 12
1.2.1 GR gene, isoforms, and protein architecture 12
1.2.2 Cytoplasmic GR and ligand binding 14
1.2.3 Nucleocytoplasmic transport dynamics 15
1.2.4 Transcriptional regulation by nuclear GR 17
1.2.5 GR downregulation and termination of signaling 19
1.3 DUSP1 as a GR-responsive negative regulator of MAPK signaling 21
1.3.1 The dual-specificity phosphatase family and MKP1 function 21
1.3.2 DUSP1 gene structure and transcriptional regulation 23
1.3.3 Post-transcriptional control of DUSP1 mRNA 26
1.3.4 DUSP1/MKP1 dysregulation in disease 28
1.4 Single-cell heterogeneity in glucocorticoid response 29
1.4.1 Sources of cell-to-cell variability in GR signaling 30
1.4.2 Limitations of bulk and population-averaged measurements 31
1.4.3 Quantitative single-cell measurement of endogenous targets 34
1.5 Stochastic modeling of gene expression dynamics 36
1.5.1 The chemical master equation framework 37
1.5.2 Numerical solution via finite state projection 38
1.5.3 Two-state promoter models and transcriptional bursting 39
1.5.4 Parameter inference from single-cell distributions 41
1.6 Existing computational models of GR-dependent transcription 42
1.6.1 Thermodynamic and equilibrium models 43
1.6.2 ODE and pathway-level kinetic models 43
1.6.3 Statistical and Boolean approaches 44
1.6.4 Gaps: spatial resolution, single-cell heterogeneity, and endogenous measurement 44
1.7 Dissertation objectives and overview 45

1.7.1 Research question and central hypothesis . . . 45
1.7.2 Specific aims . . . 46
1.7.3 Dissertation organization . . . 48

Chapter 2 Integrating Single-Cell Experiments and Stochastic Models to Understand and Predict Glucocorticoid Receptor Transport and *DUSP1* mRNA Expression Dynamics . . . 49
2.1 Introduction . . . 51
2.2 Results . . . 54
2.2.1 Subcellular ICC measurements reveal heterogeneous GR translocation dynamics . . . 54
2.2.2 A stochastic model of Dex-driven nuclear import and compartment-specific degradation captures GR dynamics . . . 56
2.2.3 Single-molecule measurements reveal stochastic *DUSP1* transcription dynamics . . . 58
2.2.4 Stochastic modeling shows that nuclear GR increases *DUSP1* transcription burst frequencies . . . 61
2.2.5 Subcellular measurements reveal complex dynamics of *DUSP1* mRNA transport and degradation . . . 62
2.2.6 Spatial stochastic modeling identifies ARE-mediated decay as the dominant cytoplasmic clearance mechanism . . . 63
2.2.7 Model predictions across Dex concentrations and transcriptional inhibition conditions . . . 66
2.3 Discussion . . . 67
2.4 Experimental framework, methods, and quantification . . . 73
2.4.1 GR quantification from immunocytochemistry . . . 78
2.4.2 *DUSP1* mRNA quantification from smiFISH . . . 80
2.5 Computational modeling and alternative model discrimination . . . 84
2.5.1 Modeling framework and inference . . . 85
2.5.2 Parameter glossary . . . 88
2.5.3 GR transport and model discrimination . . . 90
2.5.4 *DUSP1* transcription and model discrimination . . . 92
2.5.5 *DUSP1* cytoplasmic regulation and model discrimination . . . 96
2.5.6 Full mechanistic GR-DUSP1-TTP network . . . 100
2.5.7 Parameter uncertainty quantification . . . 102
2.5.8 Shared parameters and final parameter inventory . . . 102

Chapter 3 Synthesis, Outstanding Questions, and Future Directions . . . 115
3.1 Synthesis . . . 115
3.2 A workflow for building predictive single-cell models of signal-activated gene regulation . . . 117
3.3 Methodological refinements to strengthen future applications . . . 118
3.4 Immediate extensions and low-hanging fruit . . . 120
3.5 Additional contributions during this PhD . . . 122

Bibliography 124

LIST OF TABLES

2.1 Per-cell variability of GR fluorescence by Dex concentration and stimulation time. . . 82
2.2 Comparison of alternative GR transport and degradation models. 92
2.3 Comparison of *DUSP1* nuclear promoter-regulation models (M1–M5). 96
2.4 Fit and prediction errors for cytoplasmic *DUSP1* models. 98
2.5 Inferred parameters for the compartment-specific GR model. 109
2.6 Inferred *DUSP1* and TTP parameters across model variants. 110
2.7 Posterior parameters for the selected semi-mechanistic *DUSP1* model. 113
2.8 Posterior parameters for the mechanistic *DUSP1*–TTP model. 114

LIST OF FIGURES

1.1 Convergence of inflammatory and glucocorticoid signaling on *DUSP1*. 2
1.2 Temporal phases and possible outcomes of an immune response. 5
1.3 Temporal dynamics of MAPK signaling and ARE-mRNA stability across inflammatory regimes. 23
1.4 Transcriptional and post-transcriptional regulation of *DUSP1*. 24
1.5 Single-cell distributions distinguish responses that share a population mean. 33

2.1 Graphical overview and model schematic of GR–DUSP1 signaling. 51
2.2 Subcellular GR translocation. 55
2.3 Subcellular *DUSP1* transcriptional regulation. 59
2.4 Model fits and predictions for *DUSP1* mRNA dynamics at 100 nM Dex. 60
2.5 Model fits and predictions across Dex concentrations and transcription inhibition conditions. 65
2.6 Model fits and predictions for *DUSP1* mRNA dynamics at 1 nM Dex. 68
2.7 Model fits and predictions for *DUSP1* mRNA dynamics at 10 nM Dex. 69
2.8 *DUSP1* mRNA distributions under transcriptional inhibition by TPL. 70
2.9 Design and targeting of the *DUSP1* smiFISH probe set. 76
2.10 Data-driven illumination correction and ICC controls for GR images. 79
2.11 Segmentation and spot detection for *DUSP1* quantification. 81
2.12 Alternative GR transport and degradation models. 93
2.13 Alternative GR-dependent *DUSP1* transcription models (M1–M5). 95
2.14 Alternative models of cytoplasmic *DUSP1* mRNA degradation. 99
2.15 Mechanistic TTP-extended model schematic. 100
2.16 Joint posterior distribution for the compartment-specific GR model. 103
2.17 Marginal posterior distributions for the compartment-specific GR model. 104
2.18 Joint posterior distribution for the semi-mechanistic *DUSP1* model. 105
2.19 Marginal posterior distributions for the semi-mechanistic *DUSP1* model. 106
2.20 Joint posterior distribution for the mechanistic *DUSP1* model. 107
2.21 Marginal posterior distributions for the mechanistic *DUSP1* model. 108

Chapter 1

Quantitative and Mechanistic Foundations of Glucocorticoid Receptor Signaling and DUSP1 Regulation

This chapter establishes the clinical, molecular, and computational context for the work that follows, beginning with the burden of inflammatory disease and the pharmacology of glucocorticoids (GCs), progressing through the structural and regulatory features of the glucocorticoid receptor (GR) and its target gene dual-specificity phosphatase 1 (*DUSP1*), and concluding with the single-cell measurement and discrete stochastic modeling frameworks that together enable the mechanistic inference pursued in subsequent chapters. Figure 1.1 provides a roadmap for the chapter: it summarizes the inflammatory and glucocorticoid signaling axes that converge on *DUSP1*, each component of which is developed in the sections that follow.

1.1 Glucocorticoids in Inflammation: Necessity and Limitations

This section establishes the clinical motivation for studying GR signaling. It begins with the global burden of inflammatory disease, the role of MAPK signaling in sustaining inflammation, and the endogenous negative regulators that constrain it, and then introduces GCs as the dominant pharmacological strategy for suppressing inflammation. The clinical limitations identified at the end of the section motivate the single-cell, mechanistic approach developed in later chapters.

1.1.1 The burden of acute and chronic inflammatory disease

This subsection introduces inflammation as the proximal driver of a majority of human disease and frames the distinction between protective acute responses and pathological chronic states. The

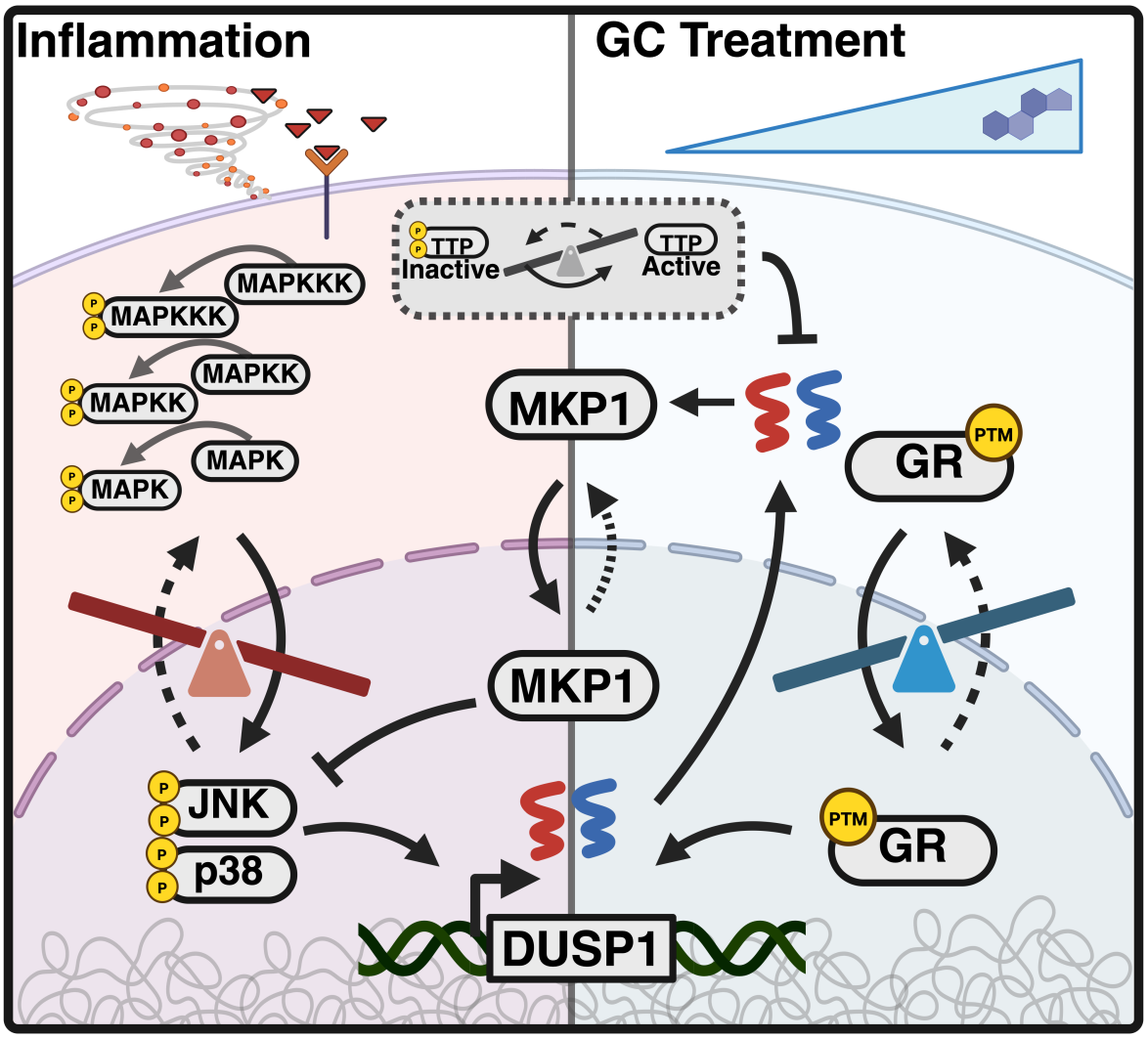


Figure 1.1: Convergence of inflammatory and glucocorticoid signaling on *DUSP1*.
Overview of the two signaling axes that regulate *DUSP1* expression, serving as a roadmap for this chapter. On the inflammatory axis (left), receptor stimulation activates the tiered MAPK cascade (Section 1.1.2), and terminally phosphorylated JNK and p38 drive *DUSP1* transcription. The DUSP1 protein product MKP1 dephosphorylates JNK and p38, forming a negative feedback loop (Section 1.3.1). On the glucocorticoid axis (right), GCs activate GR, whose transport and post-translational modification state (Section 1.2) govern its accumulation in the nucleus, where it up-regulates *DUSP1* transcription through GREs (Section 1.3.2). Both axes converge on the *DUSP1* locus, and the resulting mRNA is subject to ARE-mediated decay by TTP, whose activity is set by a phosphorylation-dependent balance between inactive and active states; by inducing MKP1 and suppressing p38, GCs shift this balance toward active, decay-promoting TTP (Section 1.3.3). This conceptual overview is developed mechanistically across the following sections and is formalized as a discrete stochastic model in Chapter 2.

transition between these states is described as a failure of the active resolution program, motivating the focus on negative regulators developed in subsequent sections.

The scope of the problem

Chronic inflammatory diseases have been recognized as the most significant cause of death in the world today, with more than 50% of all deaths being attributable to inflammation-related diseases [1]. These conditions span cardiovascular, metabolic, autoimmune, and neurodegenerative systems, indicating that the inflammatory mechanisms underlying them are not disease-specific but reflect shared dysregulation of core intracellular signaling pathways [1–3]. This burden is compounded by the global rise of known risk factors for chronic inflammation, including aging populations, increasing obesity prevalence, environmental exposures, and sedentary lifestyles [1]. The shared involvement of inflammatory signaling across this range of pathologies has motivated extensive investigation into the molecular pathways that initiate, amplify, and resolve inflammatory responses, and into the pharmacological strategies that target them [4, 5].

Health and economic impact of inflammatory disease

Beyond the clinical burden, inflammatory diseases and related conditions incur significant financial cost across the entire healthcare continuum [6]. This extends beyond direct treatment costs to encompass long-term disease management, recurring hospitalization, disability, and lost workforce productivity [4, 6]. A central factor driving this cost is that current anti-inflammatory therapies manage symptoms and suppress acute flares but rarely achieve long-term resolution [7]. Addressing this challenge requires not only improved therapeutics but also deeper mechanistic understanding of the signaling networks that sustain chronic inflammatory states.

Acute versus chronic inflammation: distinct signaling and resolution dynamics

Acute inflammation is protective and self-limiting. Inflammation is a fundamental protective response to pathogens and tissue damage [8, 9]. The inflammatory response unfolds across distinct temporal phases, from rapid onset through active resolution to a longer-term outcome that either

restores tissue homeostasis or progresses to chronic inflammation (Figure 1.2). Acute inflammatory stimuli trigger rapid, high-amplitude activation of innate immune pathways, recruitment of immune cells to sites of injury or infection, and local production of pro-inflammatory mediators. These responses are propagated through conserved intracellular signaling pathways, including NF-κB and the mitogen-activated protein kinases (MAPKs), which integrate extracellular stimuli into transcriptional and post-transcriptional responses [10].

Resolution is an active, regulated process. The defining feature of acute inflammation is that it resolves: the same signaling networks that initiate the response also activate negative regulatory programs that terminate it once the threat is cleared [11]. Resolution of inflammation is not a passive process driven by decay of pro-inflammatory signals but an actively coordinated program requiring the timely induction of anti-inflammatory mediators and negative regulators. These include anti-inflammatory lipid mediators such as lipoxins and resolvins, anti-inflammatory cytokines such as IL-10, phagocytic clearance of apoptotic cells, and induction of negative-feedback phosphatases that directly inactivate pro-inflammatory signaling cascades. Among these, the dual-specificity phosphatases (DUSPs) that dephosphorylate and inactivate MAPKs represent a critical node linking transcriptional regulation to inflammatory resolution [12].

Chronic inflammation as a failure of resolution When the resolution program is insufficient, overwhelmed, or actively suppressed, acute inflammation transitions to a chronic state. Chronic inflammation is characterized by persistent accumulation of mononuclear immune cells, ongoing tissue injury, and progressive remodeling including fibrosis [2, 4]. At the signaling level, chronic inflammation is maintained by sustained activation of the same kinase cascades that drive acute responses, without the counterbalancing induction of negative regulators that would normally terminate signaling [2, 11]. This self-sustaining signaling underlies the persistent, progressive nature of the diseases described above, and it is the target of the anti-inflammatory pharmacology discussed in the following sections.

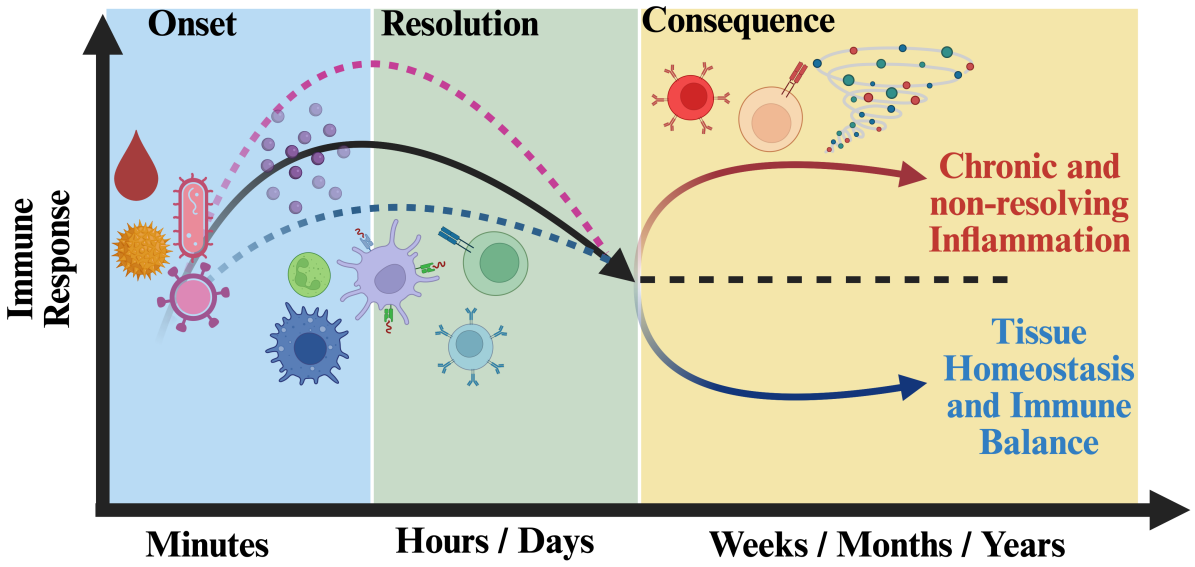


Figure 1.2: Temporal phases and possible outcomes of an immune response.
Schematic of immune response magnitude over time, progressing through three phases. During **onset** (minutes), tissue damage, pathogens, and allergens trigger a rapid innate response. During **resolution** (hours to days), innate and adaptive effectors, including antigen-presenting cells, lymphocytes, and antibodies, coordinate clearance as the response subsides. The **consequence** phase (weeks to years) reflects the long-term outcome: a properly regulated response (blue) returns to baseline and restores tissue homeostasis and immune balance, whereas a dysregulated response (red) fails to resolve and progresses to chronic, non-resolving inflammation. The dashed line marks the pre-stimulus baseline. Adapted from [9].

1.1.2 MAPK Signaling as a Central Amplifier of Inflammatory Responses

This subsection reviews the architecture of the MAPK cascades that transduce inflammatory stimuli into transcriptional and post-transcriptional outputs, with emphasis on the stress-responsive p38 and JNK arms that are most relevant to inflammatory pathology. The compartmentalization, crosstalk, and feedback regulation of these pathways are discussed as the substrate on which the DUSP1-mediated negative feedback studied in later chapters acts.

The MAPK kinase cascade architecture

At the core of this regulatory architecture are the mitogen-activated protein kinase (MAPK) cascades, which function as tiered kinase cascades that transmit external signals into intercellular signaling dynamics [13–16]. Upon ligand binding, tyrosine kinase domains dimerize initiating the kinase cascade. Activated receptor phosporylates MAP3ks, which phosphorylate MAP2k,

and termianlly phosphorlated MAPKs translocate into the nucleus to modulate transcription. The three main arms of the MAPK signaling pathway are named after their respective terminal kinase, ERK, p38 nad JNK. This architecture provides signal amplification, integration, and noise filtering, and the same kinase modules are reused across distinct stimuli to generate stimulus-specific outputs [16].

p38 and JNK as stress-responsive inflammatory effectors

The p38 and JNK arms of the MAPK network integrate upstream kinase activation into transcriptional programs that promote cytokine production, cellular stress adaptation, and immune effector function [13, 15–18]. These pathways are activated by inflammatory cytokines such as IL-1 and TNF, by oxidative stress, and by pathogen-associated molecular patterns recognized through pattern-recognition receptors. Once activated, p38 and JNK phosphorylate transcription factors including ATF2, c-Jun, and members of the AP-1 family, and they also act post-transcriptionally through downstream kinases such as MK2 that stabilize cytokine mRNAs. The combined transcriptional and post-transcriptional outputs of p38 and JNK place these kinases at a central position in the amplification of inflammatory responses.

Subcellular compartmentalization, crosstalk, and feedback

p38 and JNK operate across both nuclear and cytoplasmic compartments, with regulated nuclear translocation, scaffold-mediated localization, and extensive crosstalk and feedback regulation [19, 20]. Active MAPKs accumulate in the nucleus to phosphorylate transcription factors, but they also retain cytoplasmic substrates including MK2 and several RNA-binding proteins. The relative balance of nuclear and cytoplasmic activity is determined by phosphorylation-dependent nuclear import, regulated nuclear export, and the activity of scaffold proteins that locally tether MAPK signaling components [16, 21]. This distributed architecture is itself a target of negative regulation, and the dephosphorylation of MAPKs by phosphatases (DUSPs) is one of the principal mechanisms by which MAPK signaling is constrained in space and time [22–24].

Persistent MAPK activation in inflammatory and autoimmune disease

Persistent or excessive activation of p38 and JNK signaling is a defining feature of numerous inflammatory and autoimmune conditions, including asthma, chronic obstructive pulmonary disease, rheumatoid arthritis, inflammatory bowel disease, and sepsis [15, 18, 25]. In each of these contexts, the duration and magnitude of MAPK activity, rather than its initial onset, is the proximal driver of pathological cytokine production and tissue damage [26]. This observation underscores the importance of the negative regulatory mechanisms that terminate MAPK signaling, and it provides the clinical context for the DUSPs that are the focus of later chapters [27–30].

1.1.3 Negative regulation and homeostatic control of inflammation

This subsection reframes inflammatory signaling as a dynamically regulated control problem in which the magnitude and duration of a response are set by the timing and strength of negative regulators. The principal classes of endogenous negative regulators acting on MAPK signaling are introduced, with DUSP1 highlighted as the central node studied in this dissertation.

Inflammation as a dynamically regulated control problem

The behavior of inflammatory signaling networks is most usefully understood not as a static on/off switch but as a dynamically regulated control problem [11]. Pro-inflammatory stimuli act as inputs to a system whose output is shaped by the combined action of feedforward amplifiers, negative feedback regulators, and integral and derivative-like elements arising from transcriptional induction, mRNA stability, and protein turnover [10]. From this perspective, the magnitude and duration of an inflammatory response are determined less by the initial stimulus than by the relative timing and strength of these regulatory elements [7, 11]. This framing motivates a quantitative approach to inflammatory regulation, in which the kinetics of induction, degradation, and feedback are measured directly and used to constrain predictive models [31, 32].

Endogenous negative regulators of MAPK signaling

The cell encodes multiple classes of endogenous negative regulators that act on MAPK signaling at distinct levels [12]. At the level of kinase activity, dual-specificity phosphatases (DUSPs, also known as MAPK phosphatases or MKPs) dephosphorylate both the threonine and tyrosine residues of the MAPK activation loop, returning the kinase to its inactive state [22, 33]. The best characterized DUSP being dual-specifictity phosphatase 1 (DUSP1) and its protein product mitogen kinase phosphatase 1 (MKP1). At the post-transcriptional level, RNA-binding proteins including tristetraprolin (TTP), AUF1, and KSRP recognize AU-rich elements (AREs) in the $3'$ untranslated regions (UTR) of cytokine and immediate-early gene transcripts and recruit decay machinery that destabilizes these messages [34, 35]. At the transcriptional level, inhibitory transcription factors and chromatin modifiers limit the duration of pro-inflammatory gene expression. Among these regulators, DUSP1 (also known as MKP1) occupies a particularly central position: it is rapidly induced by inflammatory stimuli and by GCs [23,36], it directly dephosphorylates p38 and JNK, and it is itself subject to post-transcriptional control through AREs in its $3'$ UTR [12,37]. The remainder of this chapter develops the experimental and mechanistic context for DUSP1 as the primary GR-responsive negative regulator studied in this dissertation.

1.1.4 Glucocorticoids as broad-spectrum anti-inflammatory therapy

This subsection traces the history of GC therapy and identifies the pharmacological and pharmacokinetic variables that determine clinical effectiveness. Acute applications such as ARDS and COVID-19 are discussed alongside chronic applications such as asthma and rheumatoid arthritis to establish the breadth of clinical contexts in which GR-driven transcriptional programs are therapeutically engaged.

Brief history: from cortisone to dexamethasone

The therapeutic potential of GCs was established in the late 1940s through the work of Hench, Kendall, and Reichstein, whose demonstration that cortisone produced rapid clinical improvement in rheumatoid arthritis launched GCs as a class of broad-spectrum anti-inflammatory agents [5].

Subsequent medicinal chemistry generated synthetic derivatives with improved receptor affinity, longer half-lives, and reduced mineralocorticoid activity. Dexamethasone (Dex) emerged from this effort as a high-affinity, long-acting GC that has since become both a clinical mainstay and a benchmark compound for mechanistic studies [38]. Throughout this dissertation, Dex is used as the prototypical GC ligand because its high affinity, and well-characterized pharmacology make it well suited for single-cell experiments.

Determinants of clinical effectiveness

The clinical effectiveness of GC therapy depends on a combination of pharmacological and pharmacokinetic variables, including the choice of agent, the route of administration, the timing of treatment relative to disease progression, the dose, the duration and tapering schedule, and the use of co-therapies [5, 7, 26, 39]. Each of these variables shapes the trajectory of receptor activation in target tissues, and small differences in any of them can produce large differences in clinical outcome [40]. The complexity of this dose-response landscape, together with the heterogeneous response observed across patients and across cells within a given tissue, motivates the development of predictive mechanistic models that connect dosing decisions to molecular outcomes at the single-cell level.

Acute applications: ARDS, COVID-19, and other emergencies

GCs are used in the most severe acute inflammatory conditions, typically when first-line non-steroidal anti-inflammatory drugs are insufficient [41]. Acute respiratory distress syndrome (ARDS) is an acute inflammatory syndrome of the alveoli and capillaries, characterized by alveolar epithelial and capillary endothelial injury with subsequent inflammatory exudation into the alveolar space [40]. Systemic GCs are used in ARDS because they downregulate inflammatory mediator production and the related pathways implicated in lung injury and, in some patients, in later fibroproliferative processes [26, 42].

The clinical relevance of GCs was reinforced during the COVID-19 pandemic, when the RECOVERY randomized controlled trial demonstrated that Dex reduced 28-day mortality among

patients receiving invasive mechanical ventilation or supplemental oxygen, although not among patients who did not require respiratory support [43]. Comparative analysis of transcriptomic responses to GCs and to SARS-CoV-2 infection has further suggested that ARE-dependent post-transcriptional regulation, including the destabilization of cytokine transcripts by TTP-related mechanisms, is a likely contributor to the therapeutic benefit observed in COVID-19 [37]. These findings highlight the importance of quantitative, mechanistic understanding of the genes and pathways that mediate the GC response.

Chronic applications: asthma, COPD, RA, and IBD

GCs are also a mainstay of chronic anti-inflammatory therapy [5]. Bronchial asthma, a chronic inflammatory disease of the airways that affects more than 300 million people worldwide, is treated primarily with inhaled corticosteroids, which improve symptom control and lung function in most patients [44]. Add-on therapies are commonly required in patients with severe asthma or with GC intolerance [45]. Chronic obstructive pulmonary disease, rheumatoid arthritis, and inflammatory bowel disease similarly rely on GCs for management of disease activity, although long-term use is constrained by the development of resistance and by accumulating adverse effects (see Section 1.1.5) [18]. In each of these chronic settings, GCs act in part by inducing negative regulators of MAPK signaling, including DUSP1, that limit the duration of pro-inflammatory cytokine production [12].

1.1.5 Clinical limitations motivating mechanistic resolution

This subsection reviews the limitations of current GC therapy, including the adverse effect profile of chronic exposure, the heterogeneous response across patients and within tissues, and the limited success of dissociated-ligand approaches. These limitations together motivate a quantitative, single-cell mechanistic framework as the foundation for improved understanding of GR-driven gene regulation.

Adverse effects of chronic glucocorticoid therapy

The clinical utility of GCs is constrained by a well-characterized profile of adverse effects that accumulate with chronic exposure, including metabolic disturbance, osteoporosis, immunosuppression, suppression of the hypothalamic-pituitary-adrenal axis, and neuropsychiatric effects [5, 46, 47]. These adverse effects are not off-target consequences of imprecise pharmacology but on-target consequences of the broad transcriptional reach of the glucocorticoid receptor (GR), which regulates expression of thousands of genes across nearly all tissues [48]. This recognition motivates strategies aimed at improved selectivity rather than at the abandonment of GR as a therapeutic target [49, 50].

Glucocorticoid resistance and inter-patient variability

A substantial fraction of patients respond poorly to GC therapy or develop reduced sensitivity over time, a phenomenon collectively referred to as GC resistance or GC insensitivity [47, 51]. Proposed mechanisms include shifts in the balance of GR isoforms toward the dominant-negative GRβ, altered patterns of GR phosphorylation and other post-translational modifications, changes in chromatin state at GR target loci, and overactivation of MAPK signaling that interferes with GR function [7, 52–54]. The variability of GC response across patients underscores the need for mechanistic understanding at the level of individual cells, since the molecular events that drive resistance are unlikely to be uniform across a tissue or a patient population.

Heterogeneous response within tissues and cell populations

Even within a clonal cell population exposed to identical conditions, the response to GC stimulation is heterogeneous: individual cells differ in the timing, magnitude, and duration of GR translocation and target gene induction [55, 56]. This heterogeneity is invisible to bulk biochemical measurements, which report only population averages, but it is a candidate explanation for the variable clinical outcomes described above [57]. A central premise of this dissertation is that quantitative single-cell measurement, combined with discrete stochastic modeling, is the appropriate framework for resolving and interpreting this cell-to-cell variation.

Limitations of selective GR modulators and dissociated ligands

Significant effort has been directed toward the development of selective glucocorticoid receptor agonists (SEGRAs) and so-called dissociated ligands, intended to preserve the anti-inflammatory trans-repression activity of GR while reducing the trans-activation activity associated with metabolic and other adverse effects [47, 58, 59]. Despite extensive preclinical effort, these molecules have not produced ligands with clinically meaningful improvements over conventional GCs, in part because the mechanistic distinction between trans-activation and trans-repression is less clean than was originally proposed [50, 60]. The limited success of this approach motivates a complementary path, in which cell-resolved mechanistic understanding of GR signaling provides the quantitative foundation for predicting and ultimately improving therapeutic outcomes.

1.2 The glucocorticoid receptor: structure, transport, and regulation

The GR is the principal mediator of GC action in mammalian cells [47, 61, 62]. As a ligand-activated transcription factor, GR translates the binding of circulating or therapeutic GCs into changes in the expression of thousands of target genes that collectively shape the metabolic, developmental, and immunomodulatory effects of this class of hormones [48, 49]. The mechanistic events that link ligand binding to transcriptional output are distributed across multiple cellular compartments [63] and involve protein folding, regulated nuclear import and export [56, 64], chromatin engagement [65, 66], coregulator recruitment [67, 68], and receptor turnover [69–71]. This section reviews the structural, kinetic, and regulatory features of GR that are relevant to the experimental and modeling work in subsequent chapters, with particular attention to the features that contribute to single-cell variability in GC response.

1.2.1 GR gene, isoforms, and protein architecture

This subsection introduces the *NR3C1* gene and the GR isoforms it encodes, summarizes the three-domain architecture of GRα, and reviews the post-translational modifications that shape its

functional state. These features establish the molecular starting point for the transport and transcriptional behaviors discussed in subsequent subsections.

The NR3C1 gene and GR isoforms

GR is encoded by the *NR3C1* gene, which produces multiple receptor isoforms through a combination of alternative splicing and alternative translation initiation [62, 72]. The two principal splice variants, GRα and GRβ, share their N-terminal and DNA-binding domains but differ in their C-terminal sequences. GRα is the canonical, ligand-binding receptor that mediates the classical genomic actions of GCs, while GRβ lacks a functional ligand-binding pocket and acts in some contexts as a dominant-negative regulator of GRα activity [73, 74]. Additional translational isoforms (GR-A through GR-D) arise from alternative initiation within the GRα transcript and differ in their N-terminal sequences and transcriptional activities [53]. The relative abundance of these isoforms varies across cell types and is implicated in the variable GC sensitivity observed across tissues and patients [62]. The work in this dissertation is performed in HeLa cells, in which GRα is the dominant isoform and is the focus of the modeling framework developed in subsequent chapters.

GR domain organization

GRα is a 777 amino acid protein organized into three principal domains: an N-terminal domain (NTD) that harbors the major transcriptional activation function AF-1, a central DNA-binding domain (DBD) consisting of two zinc-finger motifs, and a C-terminal ligand-binding domain (LBD) that contains AF-2 and the hormone-binding pocket [47, 49, 75]. A short hinge region between the DBD and LBD contains the principal nuclear localization sequence and is the target of multiple post-translational modifications. The NTD is intrinsically disordered and adopts ensembles of conformations rather than a single defined structure [76]. This structural plasticity provides a flexible interface for coregulator recruitment and is increasingly recognized as a determinant of the dynamic chromatin engagement behavior discussed in Section 1.2.4.

Post-translational modifications and functional consequences

GR is subject to extensive post-translational regulation, including phosphorylation, acetylation, ubiquitination, and SUMOylation, that modulates ligand sensitivity, nuclear localization, transcriptional activity, and protein turnover [70, 77, 78]. Phosphorylation at multiple serine residues in the NTD, mediated by kinases including CDK, GSK3, p38, and JNK, alters both the magnitude and gene-specific pattern of GR transcriptional output [79–81]. Acetylation in the hinge region has been shown to regulate the ability of GR to repress NF-κB-dependent transcription [70, 82]. Lysine residues in the LBD, including K419 in human GR, serve as sites for ubiquitination that targets the receptor for proteasomal degradation following ligand activation [78]. The combinatorial nature of these modifications produces a population of GR molecules with heterogeneous regulatory states, and contributes to the cell-to-cell variation in GR function discussed in Section 1.4.

1.2.2 Cytoplasmic GR and ligand binding

This subsection describes the cytoplasmic chaperone complex that maintains unliganded GR in a ligand-binding-competent state, the conformational consequences of GC binding, and the resulting exposure of nuclear localization sequences. Together these events couple ligand binding to the nuclear import process examined in the following subsection.

The HSP90/FKBP chaperone complex

In the absence of ligand, GR is maintained in the cytoplasm as part of a multiprotein chaperone complex that includes HSP90, HSP70, p23, and immunophilins such as FKBP51 and FKBP52 [47, 49]. This complex stabilizes the LBD in a high-affinity, ligand-binding-competent conformation and simultaneously masks the principal nuclear localization sequence in the hinge region, retaining the receptor in the cytoplasm. The composition of the chaperone complex is a determinant of GR ligand sensitivity: FKBP51 and FKBP52 compete for binding to the same site and exert opposing effects on GR activity, with FKBP52 promoting and FKBP51 antagonizing the receptor response. Cell-to-cell variation in chaperone composition is therefore a candidate source of heterogeneity in apparent GC sensitivity, even before considering downstream regulatory variation.

Ligand binding kinetics and conformational change

GC binding to the LBD induces a coordinated conformational rearrangement, most notably the repositioning of helix 12 of the LBD into the agonist position that completes the AF-2 coactivator interface [75]. This conformational change is communicated through the LBD to the chaperone complex, triggering its dissociation and exposing the previously masked nuclear localization sequence. Dex is a high-affinity synthetic GC with a slow dissociation rate from GR, properties that make it well suited for the controlled stimulation experiments described in Chapter 2 [38]. The kinetics of ligand binding and chaperone dissociation are fast on the time scale of the transcriptional response and are therefore not the rate-limiting steps for nuclear accumulation of GR following Dex treatment.

Exposure of nuclear localization sequences

GR contains two nuclear localization sequences, designated NL1 and NL2 [49, 64, 83]. NL1, located in the hinge region adjacent to the DBD, is a classical bipartite NLS that mediates rapid, importin-dependent nuclear import. NL2, distributed across the LBD, mediates slower import that is less well characterized mechanistically. In the unliganded state, both signals are masked by the chaperone complex and by intramolecular contacts within the LBD. Ligand binding, by triggering chaperone dissociation and conformational reorganization of the LBD, exposes NL1 and renders the receptor competent for active transport into the nucleus. This ligand-dependent exposure of import signals provides the molecular basis for the rapid, ligand-induced nuclear translocation that is the central observation of the GR transport experiments in Chapter 2.

1.2.3 Nucleocytoplasmic transport dynamics

This subsection reviews the importin-mediated nuclear import of ligand-bound GR, the CRM1-dependent export pathways and their recent reinterpretation in light of nuclear degradation data, and the continuous shuttling behavior revealed by live-cell imaging. These dynamics motivate the discrete stochastic transport model developed in Chapter 2.

Importin-mediated nuclear import

Ligand-bound GR is imported into the nucleus through the classical importin-α/importin-β pathway [64, 83]. The NL1 sequence in the hinge region is recognized by importin-α, which then associates with importin-β to dock the cargo complex at the nuclear pore. Translocation through the pore is energetically coupled to the RanGTP gradient that is maintained across the nuclear envelope, and cargo release in the nucleus is driven by RanGTP-mediated dissociation of the importin complex. The observed rate of nuclear accumulation of GR following GC stimulation is therefore the convolution of ligand binding, chaperone dissociation, NLS recognition, and pore translocation. Each of these steps imposes a kinetic constraint, but at typical GC concentrations the overall import rate is fast relative to the timescales of transcriptional activation and mRNA accumulation that are the central observables in Chapter 2.

CRM1-dependent nuclear export

Nuclear GR has classically been described as exported back to the cytoplasm through CRM1-dependent pathways that recognize leucine-rich nuclear export signals in the receptor [48]. This export is suppressed by ligand binding, both because the chaperone complex that normally promotes cytoplasmic retention has dissociated, and because the ligand-induced conformational state of the LBD reduces the accessibility of the export signal [64, 83]. A widely cited regulatory layer on this pathway is JNK-mediated phosphorylation of GR at S226, which enhances CRM1-driven export after hormone withdrawal and has been proposed to terminate GR-mediated transcription through cytoplasmic recycling of the receptor [84, 85]. More recent live-cell and pulse-chase work in prostate cancer cells has complicated this recycling picture: hormone withdrawal was shown to trigger nuclear GR degradation rather than nuclear-to-cytoplasmic export, and unliganded GR was imported into the nucleus and degraded there without ever returning to the cytoplasm [71]. Although S226-dependent export remains a valid mechanism, these findings suggest that under typical stimulation conditions GR transport is closer to a one-way trip in which nuclear clearance is governed largely by degradation. The steady-state nuclear occupancy of GR following stimulation therefore reflects a balance between fast import and the clearance processes discussed in

Section 1.2.5, and the question of whether any residual cytoplasmic GR reflects ongoing return flux or simply the not-yet-imported pool is one that single-cell joint distributions of nuclear and cytoplasmic GR are well positioned to address.

Continuous shuttling and residence-time models

Although GR is often described as undergoing a simple cytoplasm-to-nucleus translocation in response to ligand, modern live-cell imaging and single-molecule tracking studies have established that GR is in continuous flux between the two compartments, even in the presence of ligand [66, 86, 87]. Fluorescence recovery after photobleaching (FRAP) and single-particle tracking measurements indicate that individual GR molecules engage chromatin transiently, with residence times that follow power-law rather than exponential distributions, and that the receptor cycles between bound and unbound states on second to minute timescales. This shuttling behavior has important implications for the interpretation of fixed-cell measurements: an observed nuclear GR level reflects not a static accumulation but a dynamic steady state set by the rates of import, export, and degradation. Chapter 2 develops a discrete stochastic model that captures this dynamic steady state and uses single-cell distributions to discriminate among alternative mechanisms by which it can be established.

1.2.4 Transcriptional regulation by nuclear GR

This subsection reviews the modes by which nuclear GR regulates transcription, including direct GRE binding, tethering and negative GRE interactions, and coregulator recruitment with chromatin remodeling. Recent power-law and IDR-mediated descriptions of GR-chromatin engagement are introduced as context for the effective two-state promoter models used in later chapters.

GRE binding and direct transactivation

The canonical mode of GR action involves binding as a homodimer to glucocorticoid response elements (GREs), short DNA sequences with a consensus palindromic motif that occurs at thou-

sands of sites across the mammalian genome [56, 75]. Direct GRE binding recruits coactivators, chromatin remodeling complexes, and components of the basal transcription machinery, leading to transcriptional activation of nearby genes. The occupancy of any particular GRE is a function of GR concentration, GRE affinity, and local chromatin accessibility, and the saturation behavior of individual loci across a range of nuclear GR concentrations has been shown to depend on these factors in combination [88]. The DUSP1 promoter, which is the principal target gene examined in this dissertation, contains GR-binding sites that have been characterized in detail and are addressed in Section 1.3.

Tethering, negative GREs, and trans-repression

Beyond canonical GRE binding, GR also regulates transcription through several non-canonical modes, including binding to negative GREs that mediate direct transcriptional repression, and tethering interactions with other transcription factors such as AP-1 and NF-κB [47, 75]. Tethering was historically proposed as the principal mechanism of GC anti-inflammatory action and as a mechanism that could be pharmacologically separated from the trans-activation responsible for metabolic adverse effects. However, recent genetic studies using GR DNA-binding-deficient mutants have shown that direct DNA recognition is required for both transactivation and trans-repression in many contexts, and that the assembly of a functional coregulator complex at GR-bound DNA is essential for both outputs [89]. This finding has substantially revised the mechanistic basis of GC anti-inflammatory action and underlies the limited success of dissociated-ligand pharmacology described in Section 1.1.5.

Coregulator recruitment and chromatin remodeling

GR engagement at chromatin recruits a large set of coregulator proteins, including the histone acetyltransferases p300 and CBP, SWI/SNF chromatin remodeling complexes, and mediator subunits, that together remodel nucleosome positioning and modify histone tails to permit productive transcription [55, 67, 68, 90]. Chromatin accessibility upstream of GR binding is itself a strong determinant of where GR engages the genome, with pre-existing accessible regions being prefer-

entially occupied [91]. The kinetics of coregulator recruitment and chromatin remodeling are rapid relative to the timescale of measurable transcriptional output, and live-cell studies have shown that individual chromatin engagement events are transient and that productive transcription requires the integration of multiple short-lived binding events. These observations motivate the two-state promoter model frameworks developed in Chapter 2, in which the kinetics of promoter switching are inferred from the statistical properties of single-cell transcript distributions.

Power-law and IDR-mediated transcription factor dynamics

Recent single-molecule tracking studies have established that GR engagement with chromatin is best described not by the simple exponential residence time distributions assumed in classical kinetic models, but by power-law distributions that arise from a broad spectrum of binding lifetimes [66]. The intrinsically disordered N-terminal domain of GR has been shown to mediate transient confinement and clustering at active chromatin sites, providing a molecular basis for the observed deviation from exponential kinetics [76]. Although the discrete stochastic models developed in Chapter 2 use exponential transition rates for tractability, the observed transcript distributions reflect the integrated effect of these complex underlying dynamics, and the inferred promoter switching rates should be interpreted as effective rates that summarize the net behavior of the system on the timescale of mRNA accumulation [92].

1.2.5 GR downregulation and termination of signaling

This subsection reviews ligand-induced ubiquitination and proteasomal degradation as the dominant clearance mechanism for activated GR, and discusses the compartment-specific consequences of nuclear versus cytoplasmic degradation. The discriminative power of single-cell joint distributions for resolving these alternatives is identified as a central methodological contribution of Chapter 2.

Ligand-induced proteasomal degradation

The dominant mechanism for terminating GR signaling is ligand-dependent ubiquitination and proteasomal degradation of the receptor [69, 78, 93]. Ligand binding promotes phosphorylation and ubiquitination of GR, with the K419 residue in human GR identified as the principal ubiquitin acceptor that targets the receptor for 26S proteasome-mediated degradation [78]. Pharmacological inhibition of the proteasome stabilizes GR protein and prolongs transcriptional responses, consistent with proteasomal turnover being the dominant clearance pathway for activated GR. Combined with the observation that hormone withdrawal triggers nuclear degradation rather than export (Section 1.2.3) [71], this places ligand-induced proteasomal turnover as the principal negative feedback limiting the duration of GR signaling, and as a key parameter in the kinetic models developed in Chapter 2.

Compartment-specific clearance and its functional consequences

The location of ligand-induced GR degradation, whether predominantly nuclear, cytoplasmic, or both, has been a long-standing question with direct consequences for the dynamics of nuclear GR occupancy [69, 78, 86, 87]. Biochemical and live-cell work in prostate cancer cells has recently argued for a nuclear-dominant clearance pathway, in which both unliganded and post-withdrawal GR are degraded within the nucleus rather than exported back to the cytoplasm [71]. Even given this updated view, alternative compartmental architectures (nuclear degradation that limits residence time at chromatin versus cytoplasmic recycling that depletes the import-competent pool) predict different shapes for the joint distribution of nuclear and cytoplasmic GR across single cells, and these distribution-level differences provide a fluctuation-based handle on the question that bulk biochemistry cannot access. One of the central results of Chapter 2 is that endogenous single-cell joint distributions of nuclear and cytoplasmic GR in HeLa cells discriminate among these alternatives, and that the experimentally observed distributions are most consistent with nuclear clearance as the dominant pathway, independently corroborating the picture emerging from the biochemical literature in a different cell type and through an orthogonal method.

1.3 DUSP1 as a GR-responsive negative regulator of MAPK signaling

DUSP1, also known as MKP1, occupies a privileged position in the regulatory architecture introduced in the preceding sections. It is a direct transcriptional target of GR, it acts as a phosphatase that inactivates the p38 and JNK MAPKs whose chronic activation drives many of the inflammatory pathologies that GCs are used to treat, and it is itself subject to post-transcriptional control through AREs in its 3′ UTR. DUSP1 therefore sits at the intersection of GR-driven transcriptional activation, MAPK-driven inflammatory signaling, and ARE-mediated mRNA decay, and its abundance at any given time reflects the joint operation of these regulatory layers. This section reviews the biochemistry of DUSP1 and its place in inflammatory regulation, the features of its gene and promoter that are relevant to transcriptional modeling, and the post-transcriptional mechanisms that shape DUSP1 mRNA distributions in the cell.

1.3.1 The dual-specificity phosphatase family and MKP1 function

This subsection introduces the DUSP/MKP family architecture, the substrate preference of MKP1 for p38 and JNK, and the delayed negative feedback loop in which MKP1 expression is induced by the same pathways it inactivates. These features establish DUSP1 as the principal GR-responsive negative regulator of MAPK signaling.

DUSP/MKP family architecture and substrate specificity

The dual-specificity phosphatases (DUSPs) are a family of enzymes that dephosphorylate both phosphothreonine and phosphotyrosine residues within a single catalytic event, distinguishing them from the more restricted protein tyrosine phosphatases and serine/threonine phosphatases [94, 95]. A functionally defined subset of the DUSP family, known as the MAPK phosphatases (MKPs), specifically target the dual phosphorylation of the TXY activation motif in the MAPK activation loop and are therefore the principal enzymes responsible for terminating MAPK signaling. Mammalian MKPs are organized into nuclear and cytoplasmic subfamilies that differ in subcel-

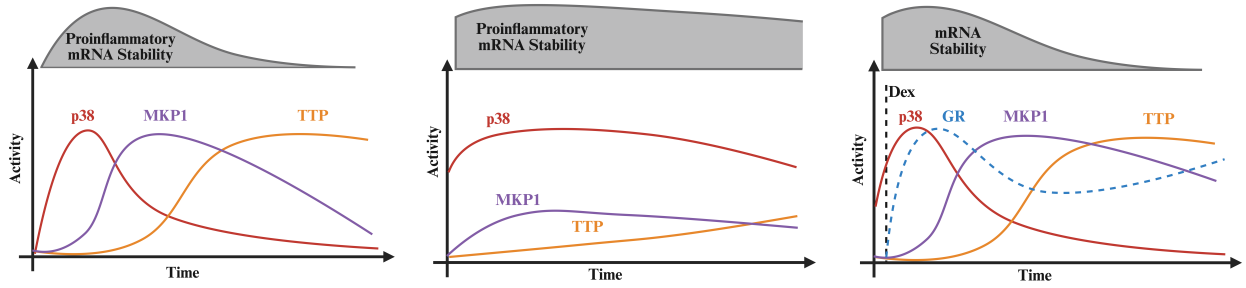
lular localization, substrate preference, and inducibility, and that together provide compartment-specific control over the duration and amplitude of MAPK activity [28, 95]. Within this family, DUSP1/MKP1 is a nuclear, inducible MKP whose expression is rapidly upregulated by a wide range of stress and inflammatory stimuli, including GC treatment.

MKP1 dephosphorylation of p38 and JNK

MKP1 preferentially dephosphorylates p38 and JNK, with lower activity against ERK, and is therefore positioned as a selective negative regulator of the stress-responsive arms of the MAPK network described in Section 1.1.2 [28, 96]. Mice deficient in DUSP1 exhibit prolonged and exaggerated p38 and JNK activation in response to inflammatory stimuli, together with elevated production of pro-inflammatory cytokines, establishing a direct, non-redundant role for DUSP1 in constraining MAPK-driven inflammation [23, 33]. The selectivity of MKP1 for p38 and JNK over ERK is consistent with the broader observation that stress and inflammatory signals are preferentially controlled by inducible negative regulators, while proliferative ERK signaling is regulated by constitutively expressed phosphatases.

The DUSP1-MAPK negative feedback loop in inflammation

DUSP1 expression is itself induced by p38 and JNK activity through the same inflammatory stimuli that activate these kinases, creating a delayed negative feedback loop in which transient MAPK activation drives its own attenuation [12, 97]. The kinetics of this feedback are central to determining whether an inflammatory response resolves or progresses to a chronic state: insufficient DUSP1 induction permits sustained MAPK activity and persistent cytokine production, while appropriately timed induction restores homeostasis (Fig. 1.3a,b). GC stimulation amplifies this feedback by inducing DUSP1 transcription through GR-dependent mechanisms that are partially independent of MAPK activity (Fig. 1.3c), and this amplification is believed to be a principal molecular basis of the anti-inflammatory action of GCs [23, 33]. The remainder of this section develops the gene-level and post-transcriptional regulatory features that determine DUSP1 abundance under these conditions.



(a) Acute inflammation **(b)** Chronic inflammation **(c)** Glucocorticoid treatment

Figure 1.3: Timing of MAPK signaling and ARE-mRNA stability distinguishes acute, chronic, and glucocorticoid-treated inflammation. Illustrative (non-quantitative) time courses of p38 MAPK, MKP1, and TTP activity, and in (c) activated GR, together with the resulting stability envelope of proinflammatory AU-rich-element (ARE) mRNAs (gray). **(a)** In acute inflammation, a transient p38 burst drives proinflammatory transcription; delayed induction of MKP1 dephosphorylates p38 and JNK, and TTP shifts to its active, decay-promoting state, together destabilizing ARE-mRNAs so the response resolves. **(b)** In chronic inflammation, sustained p38 activity with insufficient or mistimed MKP1 and TTP activity fails to destabilize ARE-mRNAs; the stability envelope stays elevated and the response does not resolve. **(c)** Glucocorticoid treatment: dexamethasone (Dex, dashed vertical line) activates GR (blue dashed), inducing *DUSP1*/MKP1 and shifting TTP toward its active state, restoring the timed decay of ARE-mRNAs and resolution. The kinetics of this GR–*DUSP1* axis are the focus of Chapter 2.

1.3.2 DUSP1 gene structure and transcriptional regulation

This subsection describes the genomic organization of human DUSP1, the GR-binding sites and coactivators at its promoter, and the transcriptional bursting behavior observed at endogenous GR target loci. These features motivate the two-state promoter modeling approach applied to DUSP1 in Chapter 2. Figure 1.4 summarizes the transcriptional and post-transcriptional control points discussed in this subsection and the next.

Genomic organization of human DUSP1

The human *DUSP1* gene is located on chromosome 5q35.1 and is organized into four exons and three introns spanning approximately 3.1 kilobases of genomic sequence on the reverse strand (GRCh38) [98]. The mature DUSP1 mRNA encodes a protein of 367 amino acids that contains an N-terminal regulatory domain, a central catalytic phosphatase domain, and a C-terminal region that mediates substrate recognition [94, 99]. The *DUSP1* mRNA contains multiple AREs within its $3'$ UTR that contribute to rapid post-transcriptional regulation and mRNA turnover [37], as

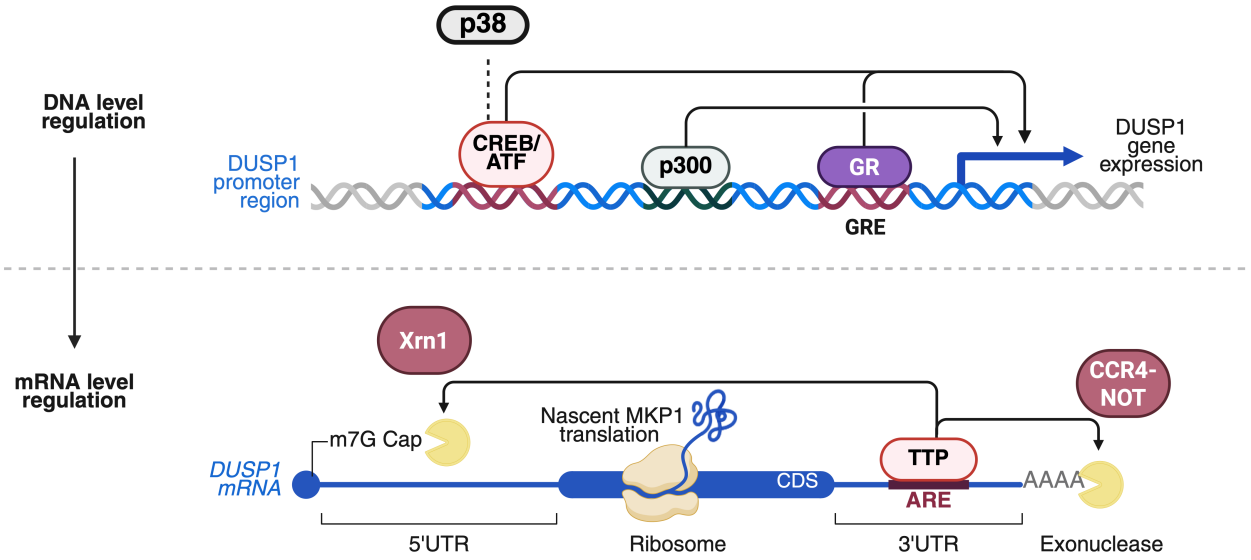


Figure 1.4: Two levels of *DUSP1* regulation. Schematic of the DNA-level (transcriptional) and mRNA-level (post-transcriptional) control points that together set *DUSP1* expression. **(Top) DNA-level regulation.** At the *DUSP1* promoter, multiple inducible inputs converge on the transcription start site: the glucocorticoid receptor (GR) bound at a glucocorticoid response element (GRE), CREB/ATF acting downstream of p38 MAPK signaling (dashed line), and the histone acetyltransferase coactivator p300. Their combined engagement drives *DUSP1* transcription, illustrating that promoter output reflects the integrated activity of several concurrent signaling inputs rather than GR alone. **(Bottom) mRNA-level regulation.** The mature *DUSP1* transcript carries a 5′ m7G cap, a coding sequence (CDS) translated by the ribosome to produce nascent MKP1, and a 3′ UTR containing an AU-rich element (ARE). Tristetraprolin (TTP) binds the ARE and recruits the CCR4–NOT deadenylase complex, promoting poly(A) tail shortening and subsequent exonucleolytic decay, while decapping exposes the transcript to 5′-to-3′ degradation by Xrn1. Transcript abundance therefore reflects a balance between synthesis and ARE-directed decay.

discussed in Section 1.3.3 [100]. The promoter region upstream of the DUSP1 transcription start site contains binding sites for multiple inducible transcription factors, including GR, AP-1, and CREB, that together account for the responsiveness of DUSP1 to a broad spectrum of stress and hormonal stimuli.

GR binding sites and coactivator recruitment at the DUSP1 promoter

The DUSP1 promoter contains characterized GR-binding sites that mediate direct GR-dependent transcriptional activation, and chromatin immunoprecipitation studies have established that GR occupancy at the DUSP1 locus increases rapidly following GC stimulation [33, 101]. GR engagement at the DUSP1 promoter is accompanied by recruitment of the histone acetyltransferase

coactivators p300 and CBP, by remodeling of the local chromatin landscape, and by recruitment of the basal transcription machinery [23]. DUSP1 expression *in vivo* is best understood not as a direct function of nuclear GR concentration but as the integrated output of multiple concurrent signaling inputs converging on the same promoter, including AP-1 and CREB-driven activation downstream of MAPK signaling alongside direct GR engagement (Fig. 1.4, top). These inputs can act concordantly to drive rapid DUSP1 induction under combined hormonal and inflammatory stimulation, but they originate from upstream pathways with opposing physiological roles, and the resulting transcriptional output reflects a convolution of signals rather than a single regulatory axis. The experimental design in Chapter 2 isolates the GR-dependent component of this response by stimulating HeLa cells with Dex in the absence of additional inflammatory inputs, allowing the kinetics of GR-driven DUSP1 transcription to be characterized independently of parallel signaling contributions.

Transcriptional bursting at endogenous GR target loci

Live-cell imaging of nascent transcription at endogenous GR target genes, together with snapshot single-molecule FISH measurements of transcription site activity, has established that GR-driven transcription occurs in discrete bursts rather than as a continuous process [55, 102]. Individual cells undergo periods of active transcription, during which multiple nascent transcripts accumulate at the locus, separated by intervals of transcriptional silence. The frequency, duration, and intensity of these bursts vary substantially across cells, even within a clonal population, and this variation is the dominant source of cell-to-cell heterogeneity in transcript abundance for many inducible genes [92, 103]. The work in Chapter 2 uses smiFISH measurements of transcription site activity at the DUSP1 locus, together with discrete stochastic modeling, to infer the kinetic parameters of this bursting behavior and to discriminate among alternative mechanisms by which GR drives DUSP1 induction.

1.3.3 Post-transcriptional control of DUSP1 mRNA

This subsection reviews the AREs in the DUSP1 3′ UTR, the destabilizing and stabilizing ARE-binding proteins that compete at these sites, and the central role of TTP in coupling MAPK signaling to DUSP1 mRNA decay. The GC-induced reshaping of this regulatory landscape motivates the integrated transcription and decay model developed in Chapter 2.

AU-rich elements in the DUSP1 3′ UTR

The DUSP1 mRNA 3′ UTR contains multiple ARE motifs, characterized by the consensus pentamer AUUUA embedded in U-rich sequence context, that function as recognition sites for trans-acting RNA-binding proteins that regulate mRNA stability and translation [12, 104]. AREs are a defining feature of a class of inflammation-associated transcripts that also includes pro-inflammatory cytokines, immediate-early gene products, and several other negative feedback regulators of MAPK signaling. Importantly, AREs are recognized by both destabilizing and stabilizing classes of RNA-binding proteins, and the net effect on transcript half-life at any given time reflects the balance of these competing activities rather than the action of a single regulator. In the case of DUSP1, the destabilizing proteins TTP and AUF1 compete with the stabilizing protein HuR for binding to overlapping sites in the 3′ UTR, and the apparent stability of DUSP1 mRNA is therefore set by the relative occupancy and activity state of these factors [100, 104]. The presence of these elements means that DUSP1 mRNA abundance at any given time is determined not only by the rate of transcription but also by the rate of decay, with both rates subject to dynamic regulation by inflammatory and hormonal signals.

ARE-binding proteins and the CCR4-NOT decay pathway

ARE-containing transcripts are recognized by a set of trans-acting RNA-binding proteins (ARE-BPs) with opposing effects on transcript stability and translation [35, 104]. The destabilizing ARE-BPs, including TTP (ZFP36), AUF1, and KSRP, recruit the CCR4-NOT deadenylase complex to the target transcript, initiating decay through poly(A) tail shortening followed by 3′-to-5′ exonucleolytic degradation by the exosome and decapping-mediated 5′-to-3′ degradation

by Xrn1 (Fig. 1.4, bottom) [105]. The stabilizing ARE-BP HuR (ELAVL1), in contrast, binds AREs with overlapping specificity and shields target transcripts from decay machinery while also promoting their translation. For DUSP1 specifically, HuR has been shown in HeLa cells to bind the 3′ UTR and to stabilize DUSP1 mRNA and enhance its translation in response to stress, and HuR silencing markedly reduces DUSP1 induction at the protein level [100]. The net effect of these competing activities on DUSP1 mRNA abundance is therefore set by both the absolute expression of each ARE-BP and by their post-translational regulatory state, with phosphorylation playing a central role for both TTP and HuR [12, 104]. In the GC-stimulated condition examined in this dissertation, HuR expression is not appreciably altered, while TTP is transcriptionally induced as a direct GR target, shifting the balance of ARE-BP occupancy toward destabilization [37]. The detailed regulation of TTP, which is the principal driver of GC-dependent destabilization of DUSP1 mRNA, is described below.

Tristetraprolin: structure, regulation, and role in mRNA destabilization

TTP is a small, intrinsically disordered protein whose central tandem zinc-finger domain recognizes ARE motifs with high specificity, while its disordered N- and C-terminal regions mediate interactions with the CCR4-NOT complex and with regulatory kinases [35, 105]. The activity of TTP is regulated by phosphorylation: p38 MAPK, acting through its downstream kinase MK2 (also known as MAPKAPK2), phosphorylates TTP at multiple sites, including S52 and S178, that recruit 14-3-3 proteins and sequester phosphorylated TTP away from its mRNA targets [12, 30, 106]. This phosphorylation effectively inactivates the decay-promoting function of TTP and stabilizes ARE-containing transcripts under conditions of active p38 signaling. DUSP1-mediated dephosphorylation of p38 reduces MK2 activity and thereby reverses TTP phosphorylation, restoring TTP-driven decay of ARE-containing transcripts, including DUSP1 itself [107]. The result is a coupled feedback in which the same phosphatase that terminates MAPK signaling also reactivates the decay of its own transcript, producing a self-limiting expression dynamic that is one of the central modeling targets in Chapter 2.

Glucocorticoid-mediated reshaping of the ARE-mRNA landscape

Beyond its effects on transcriptional induction, GC treatment globally reshapes the abundance of ARE-containing transcripts through coordinated effects on transcription, ARE-BP expression, and ARE-BP activity [37]. Recent transcriptome-wide analyses have shown that GC treatment destabilizes a substantial fraction of ARE-containing pro-inflammatory transcripts, in part through GC-induced changes in TTP expression and activity, and that DUSP1 itself is among the transcripts that are post-transcriptionally destabilized by GCs despite being transcriptionally induced [37]. The net abundance of DUSP1 mRNA in GC-treated cells therefore reflects a balance between strong transcriptional activation and partially counteracting post-transcriptional destabilization. This finding directly motivates the modeling framework developed in Chapter 2, in which DUSP1 mRNA distributions are interpreted as the joint output of transcriptional, export, and decay processes rather than as a direct readout of transcriptional activity alone.

1.3.4 DUSP1/MKP1 dysregulation in disease

This subsection summarizes the clinical contexts in which altered DUSP1 expression has been implicated, including inflammatory and autoimmune disease, GC resistance, and the host response to COVID-19. These observations reinforce the value of predictive, mechanistic models of GC-induced DUSP1 dynamics.

Inflammatory and autoimmune disease

Altered expression or activity of DUSP1 has been implicated in a broad range of inflammatory and autoimmune conditions, including asthma, chronic obstructive pulmonary disease, sepsis, inflammatory bowel disease, and rheumatoid arthritis [12, 23]. In several of these settings, reduced DUSP1 induction or sustained TTP inactivation has been associated with prolonged MAPK signaling and persistent cytokine production, providing a mechanistic link between negative feedback failure and clinical disease severity. DUSP1 has also been implicated in the development of GC resistance: in some cell systems, sustained DUSP1 expression maintains the activity of downstream transcription factors such as IRF1 and contributes to a reduced apparent GC response [108].

The crosstalk between p38 and GR in epithelial cells from inflammatory airway disease provides an additional clinical context in which the DUSP1-MAPK feedback loop has been studied as a determinant of treatment response [109].

Implications for COVID-19 and beyond

The clinical importance of DUSP1 dynamics was reinforced during the COVID-19 pandemic, when the RECOVERY trial demonstrated that Dex reduced mortality among hospitalized patients requiring respiratory support [43]. Comparative transcriptomic analysis of the host response to SARS-CoV-2 infection and to GC treatment identified ARE-mediated post-transcriptional regulation as a likely contributor to the observed therapeutic benefit, with DUSP1 induction and TTP-driven decay of cytokine transcripts both implicated in the resolution of cytokine-driven lung pathology [37, 110]. These findings highlight the value of predictive, mechanistic models of GC-induced DUSP1 expression that incorporate both transcriptional and post-transcriptional regulation, and they motivate the integrated modeling approach developed in subsequent chapters.

1.4 Single-cell heterogeneity in glucocorticoid response

The mechanisms described in the preceding sections, including GR transport, transcriptional activation at the DUSP1 promoter, and ARE-mediated mRNA decay, operate within individual cells, and the parameters governing each step vary across cells in a population. The behavior of any one cell at a given time therefore reflects the local realization of these stochastic and variable processes, and the response of a population is the aggregate of these individual realizations rather than a uniform average behavior. This section reviews the principal sources of cell-to-cell variability in GR signaling, the limitations that population-averaged measurements impose on the recovery of mechanistic parameters, and the experimental approaches that allow endogenous GR and DUSP1 responses to be measured at single-cell resolution.

1.4.1 Sources of cell-to-cell variability in GR signaling

This subsection identifies the principal sources of variability in the GR response, including stable differences in receptor abundance, isoform composition, and chaperone state, and intrinsic stochasticity in gene expression and chromatin state at target loci. These sources together shape the single-cell distributions that the modeling framework in Chapter 2 is designed to interpret.

Receptor abundance, isoform composition, and cell cycle variability

Even within a clonal cell population grown under uniform conditions, individual cells differ substantially in the molecular determinants of GR responsiveness, and several of these differences are stable on the timescale of an experiment. Total GR protein abundance varies cell to cell, and although this variation is not sufficient on its own to determine the qualitative shape of the dose-response, it contributes to the magnitude of the response when combined with downstream variability in chaperone composition, coregulator availability, and chromatin state [56, 88]. The relative abundance of GR isoforms, including the GRα to GRβ ratio and the distribution among the GR-A through GR-D translational isoforms introduced in Section 1.2.1, provides a second axis of variability that influences both ligand sensitivity and target gene selectivity, since these isoforms differ in transcriptional activity despite sharing the same DNA-binding domain [62, 72]. Variation in the composition of the cytoplasmic chaperone complex, particularly in the relative expression of FKBP51 and FKBP52, exerts opposing effects on ligand sensitivity and acts upstream of nuclear translocation. Finally, asynchronous cell cycle progression imposes a further source of variability: GR abundance, chromatin accessibility at target loci, and the activity of cell cycle-coupled kinases that modify GR all change with cell cycle phase, so a population of unsynchronized cells samples a distribution of cycle-dependent states at the moment of stimulation [111]. These stable, cell-intrinsic differences combine with the stochastic timing of the response to shape the nuclear GR distributions observed in fixed-cell snapshots.

Stochastic gene expression and transcriptional bursting

A second, mechanistically distinct source of variability is the inherently stochastic nature of gene expression itself [92, 112]. Transcription occurs in discrete bursts driven by the random opening and closing of the promoter, and each burst produces a small, integer number of mRNA molecules whose subsequent processing, export, and decay are also discrete and random events. The cell-to-cell variation that arises from these processes, even when all upstream signaling is identical, is referred to as intrinsic noise and is distinguishable in principle from extrinsic variation in cell state through dual-reporter experiments. Intrinsic noise is particularly pronounced for inducible genes such as DUSP1 that exhibit low basal expression and large fold-induction, and the burst structure of their transcriptional output is the principal source of the wide cell-to-cell distributions observed in single-cell measurements [102, 113].

Chromatin state heterogeneity at GR target loci

The chromatin landscape at GR target loci is itself variable across cells, providing a third source of response heterogeneity that acts at the level of regulatory accessibility [55, 114]. Joint profiling of chromatin accessibility and transcription in single cells has shown that the same genomic locus can occupy different accessibility states across cells in a clonal population, and that these state differences predict the magnitude of subsequent transcriptional response to inducing stimuli. For GR specifically, pre-existing chromatin accessibility at GR-binding sites is a strong predictor of where the receptor engages the genome and how productively transcription is initiated. This chromatin-level variability contributes to the long-tailed distributions of transcriptional output observed at GR target genes and is incorporated phenomenologically into the two-state promoter models developed in Chapter 2.

1.4.2 Limitations of bulk and population-averaged measurements

This subsection establishes that population-averaged measurements obscure mechanistically informative features of the response and cannot in general discriminate among kinetic models that produce identical means. The fluctuation fingerprint of single-cell distributions is introduced as the

discriminative signal that motivates the experimental and modeling approach taken in subsequent chapters.

Mechanism-masking by averaging

Population-averaged measurements report only the mean of the distribution of single-cell outputs, and this averaging obscures features of the response that are mechanistically informative [31, 92]. A bimodal population, in which a fraction of cells respond strongly and the remainder not at all, can produce the same population mean as a unimodal population in which all cells respond at an intermediate level, and these two scenarios imply very different regulatory mechanisms. Bulk biochemistry, including Western blotting and bulk RNA-seq, is unable to distinguish between them. The distributions of single-cell transcript counts and protein levels contain information about both the magnitude and the structure of the response, and access to this information is a prerequisite for inferring the underlying kinetic mechanisms.

Failure to discriminate among kinetic models with identical means

The limitation imposed by averaging is not merely a matter of resolution but extends to formal model identifiability [32, 103]. Distinct kinetic models of transcriptional regulation can be constructed that produce identical mean trajectories while predicting different distribution shapes, and mean-level data are therefore insufficient to discriminate among them. A change in transcript abundance produced by an increase in burst frequency is indistinguishable from the same change produced by an increase in burst size when only the mean is observed, but the two scenarios produce different variances, different distribution shapes, and different temporal correlations. Distribution-level data are therefore necessary, not merely helpful, for the mechanistic discrimination that motivates this dissertation.

The fluctuation fingerprint as a discriminative signal

The cell-to-cell variability that bulk measurements average away can be reframed as a fluctuation fingerprint that constrains kinetic parameters far more tightly than the mean response

alone [31, 115]. The shape of the single-cell distribution, including its variance, skewness, and the position of any modes, depends sensitively on the rates of promoter switching, transcription, and mRNA decay, and these dependencies often resolve parameter combinations that are unidentifiable from mean-level fitting. There is a fundamental limit on the precision with which kinetic parameters can be inferred from any finite amount of single-cell data, set by the stochastic dynamics of the underlying network [116], but in practice the information content of single-cell distributions is sufficient to discriminate among the alternative mechanistic models considered in Chapter 2.

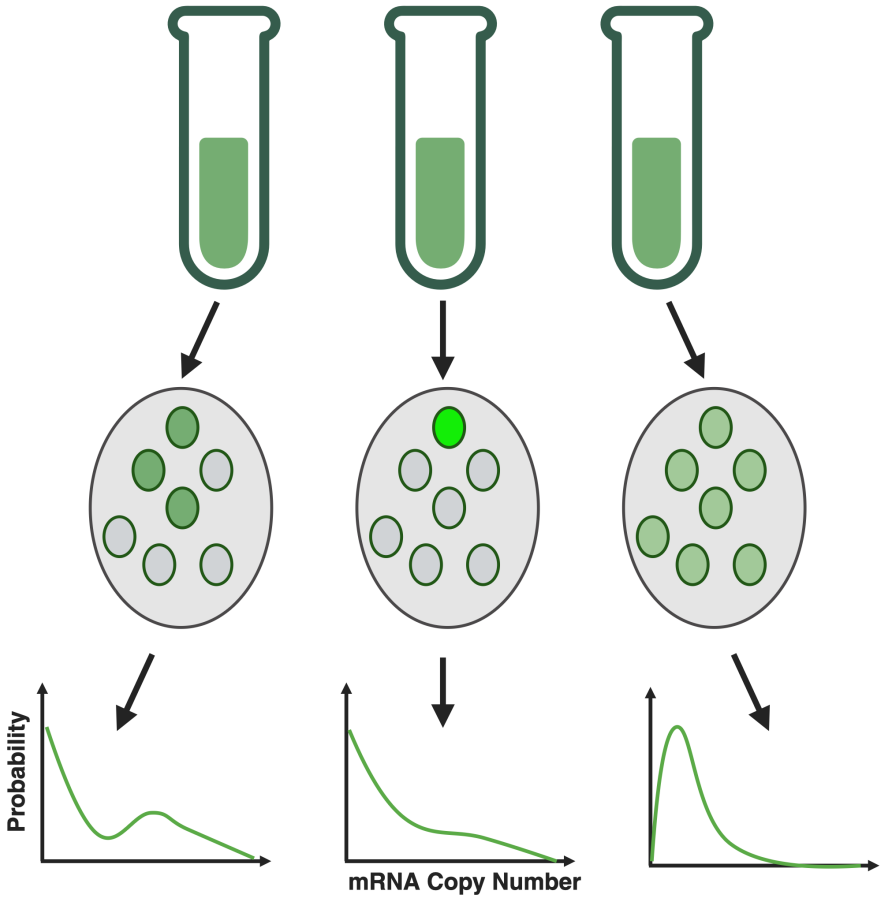


Figure 1.5: Single-cell distributions distinguish responses that share a population mean.
Three cell populations with identical bulk expression (top, equal mean signal) can arise from distinct underlying single-cell distributions (middle), which a population-averaged measurement cannot separate. Resolving expression at the single-cell level recovers the full distribution of mRNA copy number (bottom), whose shape, including bimodality, skewness, and variance, reports regulatory features that the mean alone obscures. This distribution-level signal is the fluctuation fingerprint exploited throughout this dissertation to discriminate among kinetic mechanisms [31, 92].

1.4.3 Quantitative single-cell measurement of endogenous targets

This subsection reviews smFISH and smiFISH for absolute mRNA quantification and quantitative ICC for endogenous protein measurement, with emphasis on the practical issues that must be addressed before these methods can be coupled to discrete stochastic models. The tradeoffs versus live-cell reporters are then summarized to motivate the fixed-cell endogenous measurement strategy adopted in Chapter 2.

smFISH and smiFISH for absolute mRNA quantification

Single-molecule fluorescence in situ hybridization (smFISH) enables direct, absolute counting of individual mRNA molecules in fixed cells using sets of short oligonucleotide probes complementary to the target transcript, each labeled with a fluorophore. The conventional smFISH approach requires the synthesis of large probe sets in which each probe carries a directly conjugated fluorophore, which becomes costly when many genes or conditions must be screened. The smiFISH variant addresses this by using unlabeled gene-specific primary probes that carry a shared docking sequence, to which a small number of fluorescently labeled secondary FLAP oligonucleotides hybridize. This decoupling of probe specificity from fluorophore identity reduces cost and allows flexible relabeling without re-synthesizing the gene-specific probes [117]. Two practical issues shape the analysis. Parameter optimization for Big-FISH [118] does not scale cleanly to the large image sets generated across many conditions and replicates, since thresholds tuned on one field of view often fail to generalize. A custom processing pipeline was therefore built around Big-FISH to batch large datasets and apply additional signal-to-noise filtering, both compartment-specific and on total spot intensity, to suppress false-positive detections. The DUSP1 probe set also targets exonic sequence rather than introns, so transcription sites cannot be isolated through a dedicated nascent-RNA channel and are instead recovered as large, bright nuclear clusters of mRNA whose integrated intensity reports the number of nascent transcripts at the locus. To partition cytoplasmic and nuclear counts in the absence of a protein-based cytoplasmic stain, dual-color smiFISH was performed with DUSP1 probes labeled in Cy5 and GAPDH exonic probes labeled in Cy3 to provide a cytoplasmic marker, with DAPI used for nuclear segmentation 2. Extension of

this protocol to combined smiFISH/ICC for joint protein and mRNA measurement, and adaptation to automated microscopy for higher-throughput acquisition, are discussed in Chapter 3.

Quantitative immunocytochemistry for endogenous protein

Endogenous protein abundance and subcellular localization can be measured in fixed cells using immunocytochemistry (ICC), in which primary antibodies specific for the target protein are detected through fluorescently labeled secondary antibodies and quantified by image analysis [119]. For GR specifically, ICC enables measurement of the nuclear and cytoplasmic distributions of the endogenous receptor without requiring fluorescent fusion constructs that may perturb function, localization, or expression [120]. Quantitative ICC poses several experimental challenges that must be addressed before single-cell intensities can be interpreted as molecular abundances. Antibody specificity must be validated against secondary-only and isotype controls to exclude off-target binding that would inflate apparent receptor abundance. In the absence of a dedicated cytoplasmic stain, cytoplasmic regions must be approximated from the nuclear mask using a pseudo-cytoplasmic ring, which sets the geometric basis for partitioning nuclear and cytoplasmic signal. Uneven illumination across the field of view must be corrected so that intensity comparisons are not confounded by position-dependent excitation, and day-to-day variation in imaging intensity must be normalized across replicates to enable pooled analysis. Finally, calibrated intensities must be discretized into molecular counts so that the resulting per-cell measurements can serve as inputs to discrete stochastic models. The protocol development and validation for GR ICC in this work, including the controls, masking strategy, illumination correction, between-day normalization, and intensity-to-count calibration, are described in detail in Chapter 2.

Tradeoffs versus live-cell reporters

Live-cell measurement of GR and target gene dynamics is possible through complementary approaches, including fluorescent fusions of GR for direct receptor tracking and MS2 or PP7 stem-loop systems for nascent transcript visualization at the locus [67, 87]. Live-cell methods provide temporal trajectories from individual cells, which fixed-cell snapshots cannot directly recover, and

they have been instrumental in establishing the dynamic, sub-saturating, and transient nature of GR-chromatin engagement [66, 67]. The principal disadvantage of these approaches is that they require exogenous reporter constructs whose expression level, isoform composition, localization, or interaction with the endogenous machinery may differ from the untagged proteins or RNAs they are intended to report on. Plasmid-driven expression can yield reporter abundances above endogenous levels, and tagged GR constructs typically lack the splice variants (such as GRβ) present in the endogenous receptor pool. Translocation reporters of kinase activity provide a related set of tools for visualizing signaling dynamics in single living cells, with similar tradeoffs in perturbation and calibration; the p38 reporter of Tomida et al., for example, required addition of a nuclear export sequence to suppress spurious nuclear accumulation of the construct [121, 122]. The work in this dissertation uses fixed-cell endogenous measurements of GR protein and DUSP1 mRNA because they provide accurate quantification of molecular species and their subcellular distribution, which outweighs the loss of temporal trajectory information for the modeling framework adopted here.

1.5 Stochastic modeling of gene expression dynamics

The single-cell variability described in the preceding section motivates a quantitative framework in which gene expression is modeled not as a continuous, deterministic process but as a discrete, stochastic one whose realizations across cells produce the observed distributions of receptor, transcript, and protein abundance. This section reviews the chemical master equation as the governing description of these processes, the finite state projection algorithm that makes the master equation tractable for inference, the two-state promoter models that capture transcriptional bursting, and the inference procedures that connect model parameters to single-cell data. The general framework is presented at a level accessible to readers without a stochastic modeling background, and each subsection closes by indicating how the framework is instantiated for GR transport and DUSP1 transcription in Chapter 2.

1.5.1 The chemical master equation framework

This subsection introduces the CME as the governing description of discrete stochastic biochemical dynamics and identifies the regimes in which the deterministic ODE limit fails to capture the distribution-level features that single-cell data report. These regimes correspond directly to the GR transport and DUSP1 transcription systems modeled in Chapter 2.

Discrete stochastic dynamics and propensity functions

A biochemical reaction network can be described as a continuous-time Markov process on a discrete state space, in which the state of the system is specified by the integer copy number of each chemical species and the dynamics are determined by a set of reactions, each with an associated propensity function [123]. The propensity of a reaction at a given state is the instantaneous probability per unit time that the reaction will fire, and it plays the role in the stochastic description that the reaction rate plays in deterministic chemical kinetics. The chemical master equation (CME) is the linear differential equation that governs the time evolution of the probability distribution over states, and its solution gives the full joint distribution of all species at all times rather than only the mean trajectory. The GR transport and DUSP1 transcription networks examined in Chapter 2 are formulated as CMEs whose state vectors specify the number of nuclear GR molecules, cytoplasmic GR molecules, transcription sites in active and inactive states, and nuclear and cytoplasmic DUSP1 mRNAs in each cell.

The deterministic limit and when it fails

In the limit of large molecule numbers and well-mixed systems, the CME reduces to a system of ordinary differential equations (ODEs) for the mean concentrations, and the stochastic and deterministic descriptions converge [123, 124]. This limit is appropriate for many metabolic and signaling networks where copy numbers are in the thousands or higher. It fails, however, in three regimes that are directly relevant to the systems studied here: when copy numbers are low (as for promoter states, transcription sites, and mRNAs of inducible genes such as DUSP1), when the system undergoes stochastic switching between states (as for promoter on/off dynamics), and when

nonlinearities, such as saturable and time dependent degradation kinetics, shape the observed distributions 2. In each of these regimes, the deterministic description loses information about the shape of the single-cell distribution, including its bimodality, skewness, and variance, that is precisely the information needed to discriminate among kinetic models.

1.5.2 Numerical solution via finite state projection

This subsection describes the FSP algorithm as the numerical method used to solve the CME for inference, including the error bounds that make it suitable for likelihood evaluation and the practical considerations for using FSP within parameter inference loops. The SSIT implementation used in this dissertation is introduced as the computational backbone of the modeling work.

State-space truncation and error bounds

The CME is an infinite-dimensional system whenever any species has an unbounded copy number, and exact analytical solutions are available only for a small set of simple networks. The finite state projection (FSP) algorithm provides a general numerical solution by truncating the infinite state space to a finite, computationally tractable subset and solving the resulting matrix differential equation directly [123]. FSP differs from sampling-based approaches such as the stochastic simulation algorithm in that it computes the probability distribution directly rather than estimating it from finite samples, and it provides rigorous one-sided error bounds on the truncation error that decrease as the included state space is expanded. These error bounds make FSP particularly well suited to parameter inference applications, where the likelihood of an observed dataset must be evaluated accurately rather than approximated stochastically.

Practical considerations for inference-grade FSP

Using FSP within an inference loop, in which the likelihood is evaluated repeatedly at thousands of parameter combinations, imposes additional practical requirements beyond a single forward solve. The truncation size must be large enough to bound the likelihood error below the resolution required for parameter discrimination, the sparse matrix representations of the CME

generator must be constructed efficiently, and the solver must be parallelized across the experimental conditions and time points being fit simultaneously [32, 125]. The Stochastic System Identification Toolkit (SSIT) developed in the Munsky group provides an integrated implementation of these requirements, with FSP solvers coupled to likelihood evaluation, parameter sampling, and Fisher information-based experimental design [126]. The inference work in Chapter 2 uses SSIT to fit and compare alternative CME-based models of GR transport and DUSP1 transcription against single-cell distributions across multiple Dex concentrations and time points.

1.5.3 Two-state promoter models and transcriptional bursting

This subsection introduces the telegraph model as the simplest stochastic description of inducible transcription, distinguishes the burst frequency and burst size mechanisms that produce identical means but different distributions, and maps the resulting distribution shapes onto observable single-cell signatures. These mappings frame the model discrimination performed for GR-induced DUSP1 transcription in Chapter 2.

The telegraph model: k_{on}, k_{off}, k_r

The simplest stochastic model of inducible transcription is the two-state, or telegraph, model, in which the promoter switches between an inactive (OFF) and active (ON) state at rates k_{on} and k_{off}, and transcription occurs at rate k_r during the ON state [92, 102]. mRNA decay occurs at rate γ independent of promoter state. Despite its simplicity, this model captures the essential observation that transcription occurs in discrete bursts separated by periods of silence, and it produces a steady-state mRNA distribution that ranges from Poisson (when promoter switching is fast relative to transcription and decay) to bimodal (when promoter switching is slow relative to decay). The mean and Fano factor of the resulting distribution depend on the relative magnitudes of k_{on}, k_{off}, k_r, and γ in ways that have intuitive mechanistic interpretations, providing a starting point for connecting observed distributions to underlying promoter behavior.

Burst frequency versus burst size as distinguishable mechanisms

A central feature of the telegraph model is that the same mean transcript abundance can arise from very different promoter behaviors. Increasing k_{on} increases the frequency of bursts while leaving their size unchanged, whereas increasing k_r or decreasing k_{off} increases the size of each burst while leaving their frequency unchanged [55, 102]. Mean transcript level alone cannot distinguish these mechanisms, but they produce qualitatively different distribution shapes, different fractions of cells with active transcription sites at any given time, and different intensity distributions at the active transcription sites themselves. Discriminating among these mechanisms is therefore a question about distribution shape, and it requires the kind of single-cell, distribution-level measurements that smFISH and smiFISH provide. For GR-induced DUSP1 transcription specifically, Chapter 2 uses smiFISH measurements of both mature transcript counts and transcription site activity to discriminate among GR-dependent regulatory schemes in which Dex modulates k_{on}, k_{off}, or combinations of both.

Mapping promoter mechanisms to observable distributions

The qualitative distribution shapes produced by the telegraph model under different parameter regimes provide an intuitive bridge between mechanism and observation [102, 103]. When promoter switching is fast relative to both transcription and decay, the resulting transcript distribution is approximately Poisson, with variance equal to the mean and a unimodal, narrow shape. When the ON state is rare but produces a large burst, the distribution becomes negative-binomial, with super-Poissonian variance and a long right tail. When the ON state is sufficiently long-lived and rare, the distribution becomes bimodal, with one peak at low transcript counts representing cells whose promoters are currently OFF and a second peak at higher counts representing cells in the middle or aftermath of a burst. Fitting the telegraph model to observed distributions therefore amounts to recovering the parameter combination that places the model in the regime consistent with the data, and this fitting procedure forms the basis of the inference work described next.

1.5.4 Parameter inference from single-cell distributions

This subsection describes likelihood-based inference of CME parameters from single-cell distributions, the Bayesian framework used to quantify parameter uncertainty, and the formal concepts of identifiability and model discrimination that determine what can be concluded from any inference exercise. These concepts directly underlie the model selection results reported in Chapter 2.

Likelihood functions over discrete distributions

Given a CME-based model with a vector of parameters $\boldsymbol{\theta}$, an FSP solution provides the predicted probability of each discrete state at each observation time, and these probabilities can be evaluated directly at the states observed in single-cell measurements to yield the likelihood of the data under the model [32, 103]. Because the FSP solution is a probability distribution rather than a moment summary, the resulting likelihood is exact within the FSP truncation error and does not require Gaussian approximations or moment-closure schemes that would discard distribution shape information. Single-cell measurements at multiple time points and Dex concentrations are combined into a joint likelihood by assuming independence across cells within each condition, and this joint likelihood is the objective function for parameter estimation and model comparison in Chapter 2.

Bayesian inference and uncertainty quantification

Parameter estimation under the FSP likelihood is performed in a Bayesian framework, in which prior distributions over the model parameters are combined with the data likelihood to yield posterior distributions that characterize both the most probable parameter values and their associated uncertainty [32,115]. Markov chain Monte Carlo sampling, typically using Metropolis-Hastings or related schemes, provides samples from the posterior that can be summarized in terms of credible intervals, marginal distributions, and joint dependencies between parameters. Uncertainty quantification matters in two ways for the modeling work in Chapter 2: it permits honest reporting of the precision with which each kinetic parameter is constrained by the data, and it propagates parameter

uncertainty into model predictions on held-out conditions, allowing predictions to be reported with credible intervals rather than as point estimates.

Identifiability and model discrimination

Two formal concepts shape what can be concluded from any single-cell inference exercise. Structural identifiability asks whether the parameters of a model are uniquely determined in principle by the available observables, while practical identifiability asks whether the available data are sufficient to constrain them with useful precision [32]. Parameters that are structurally identifiable but practically unidentified appear in the posterior as broad marginal distributions or strong joint correlations, and these patterns are themselves mechanistic information rather than failures of the inference procedure. Model discrimination, distinct from parameter inference, asks which of several candidate models is best supported by the data, and is typically performed using information criteria such as the Bayesian information criterion (BIC) and the Akaike information criterion (AIC), or through formal Bayesian model comparison. The central methodological output of Chapter 2 is a model discrimination outcome: among the alternative mechanistic schemes considered for GR transport, for DUSP1 promoter regulation, and for cytoplasmic mRNA fate, the data identify a specific subset as best supported and reject others as inconsistent with the observed single-cell distributions.

1.6 Existing computational models of GR-dependent transcription

The biological and mathematical foundations developed in the preceding sections have motivated a substantial body of computational modeling of GR signaling and GC-induced transcription. These prior efforts have addressed complementary questions and have used a range of mathematical frameworks, from equilibrium statistical thermodynamics to deterministic kinetic models to statistical and Boolean network analyses. The purpose of this section is not to provide an exhaustive review, but to identify what each class of approach has contributed, what it has been unable

to address, and where the integrated single-cell, discrete stochastic framework developed in this dissertation fills a specific gap in the existing landscape.

1.6.1 Thermodynamic and equilibrium models

Statistical thermodynamic models treat the assembly of GR, coregulators, and DNA at a target gene as an equilibrium process governed by binding affinities, cooperativity terms, and coregulator concentrations, and predict the resulting transactivation as a function of ligand and coregulator availability [59]. This framing has been productive for interpreting allosteric coupling between ligand binding, dimerization, and coregulator recruitment, and for explaining how the same receptor can produce ligand-specific and gene-specific transcriptional outputs from a small set of biophysical parameters. The principal limitation of equilibrium models for the questions addressed in this dissertation is that they describe the steady state of the assembled complex rather than its temporal dynamics, and they assume a deterministic population average rather than predicting the cell-to-cell distribution of transcriptional outputs. They are therefore not suited to the inference of kinetic parameters from time-resolved, single-cell measurements of nuclear GR and DUSP1 transcript distributions.

1.6.2 ODE and pathway-level kinetic models

Deterministic kinetic models, formulated as systems of ordinary differential equations (ODEs), have been developed to describe GR autoregulation, target gene induction, and GR-mediated crosstalk with other pathways in both GC-sensitive and GC-resistant cell systems [127, 128]. Related ODE frameworks have been used to model GR dimerization cycles and the multi-tissue pharmacodynamics of GC-induced target genes such as GILZ [129, 130]. These models successfully capture the population-average kinetics of GR signaling and have been useful for interpreting how perturbations to individual rate constants would affect the mean response. As discussed in Section 1.4.2, however, deterministic descriptions cannot reproduce the distribution shapes of single-cell measurements and cannot discriminate between alternative kinetic mechanisms that produce

identical means. The limitation is intrinsic to the framework rather than a matter of model complexity, and it cannot be addressed by adding more reactions to an ODE description.

1.6.3 Statistical and Boolean approaches

A complementary set of approaches uses statistical and logical models to describe GR signaling without committing to detailed kinetic rate laws. Multivariate statistical analyses of GR phosphorylation patterns and protein-protein interactions have been used to identify biomarkers of GC response and to relate receptor modification state to target gene output [60]. Boolean and network-based analyses of the GR interactome have provided qualitative predictions about pathway connectivity and have suggested candidate nodes whose perturbation could modulate the GC response [51]. These methods are valuable for hypothesis generation and for identifying interactions that warrant detailed mechanistic investigation. They are not, however, designed to produce quantitative, distribution-level predictions about endogenous transcript or protein abundance in single cells, and they cannot be used directly for the parameter inference and model discrimination tasks pursued in this dissertation.

1.6.4 Gaps: spatial resolution, single-cell heterogeneity, and endogenous measurement

Across the approaches reviewed above, four limitations recur and together define the specific gap that this dissertation aims to fill. First, most existing models operate at steady state or on population averages, and therefore cannot resolve the time-dependent, distribution-level features of the single-cell response. Second, most models do not incorporate the explicit subcellular spatial information (nuclear versus cytoplasmic localization of GR, transcription site activity at the locus, nuclear versus cytoplasmic mRNA) that single-cell imaging provides and that constrains alternative transport and processing mechanisms. Third, very few existing models combine endogenous single-cell measurement with discrete stochastic modeling, instead relying on bulk biochemistry, exogenous reporter constructs, or both. Fourth, existing models of GR-driven transcription typi-

cally focus on either the upstream receptor dynamics or the downstream transcript-level response, but rarely integrate GR transport, promoter activation, mRNA export, and ARE-mediated decay within a single, jointly fit framework whose predictions are validated against held-out conditions. Closing this gap, by developing and quantitatively validating an integrated, single-cell, discrete stochastic model of GR transport and DUSP1 mRNA dynamics, is the central methodological contribution of the work described in Chapter 2.

1.7 Dissertation objectives and overview

This section states the central research question and hypothesis of the dissertation, presents the four specific aims that operationalize them, and outlines the organization of the remaining chapters.

1.7.1 Research question and central hypothesis

The preceding sections have established that GC signaling through GR is one of the most clinically consequential anti-inflammatory pathways in human biology, that the dynamics of GR transport and the regulation of GR target genes such as DUSP1 are intrinsically heterogeneous across single cells, and that existing computational models of this system have not integrated endogenous single-cell measurement with discrete stochastic modeling. These observations motivate the central research question of this dissertation: how do GR nucleocytoplasmic transport dynamics, transcriptional bursting at the DUSP1 promoter, and ARE-mediated cytoplasmic mRNA decay jointly produce the observed single-cell distributions of DUSP1 expression following GC stimulation, and which features of these processes are uniquely identifiable from endogenous single-cell measurements?

The central hypothesis of this work is that endogenous, single-cell measurements of GR localization and DUSP1 transcript abundance, when combined with discrete stochastic models formulated in the chemical master equation framework, are sufficient to identify the dominant mechanisms governing each stage of the response and to quantitatively constrain the kinetic parameters

that describe them. The hypothesis is operationalized through three specific aims that together produce an integrated, experimentally validated model of GR-driven DUSP1 dynamics.

1.7.2 Specific aims

The four specific aims progress from upstream GR transport dynamics to promoter-level transcriptional regulation, to model-based discrimination of post-transcriptional decay mechanisms, and finally to mechanistic validation through TTP dynamics and prediction on held-out conditions.

Aim 1: Quantify GR nucleocytoplasmic transport dynamics and identify dominant clearance mechanisms

The first aim uses quantitative ICC of endogenous GR across multiple Dex concentrations and time points to measure single-cell distributions of nuclear and cytoplasmic GR in HeLa cells. Discrete stochastic models of GR transport and degradation, formulated in the CME framework and solved by FSP, are fit to these distributions and compared to discriminate among alternative clearance mechanisms, including cytoplasmic recycling, nuclear degradation, and combinations of both. The aim establishes the kinetic structure of the upstream GR response and identifies the mechanisms most consistent with the joint nuclear and cytoplasmic distributions observed in single cells.

Aim 2: Quantify endogenous DUSP1 transcription and discriminate among GR-driven promoter mechanisms

The second aim uses smiFISH to measure both transcription site activity and mature DUSP1 mRNA abundance in single cells across the same Dex doses and time points used in Aim 1. Two-state promoter models with alternative GR-dependent regulatory schemes, including Dex-driven increases in promoter activation rate k_{on}, Dex-driven decreases in promoter deactivation rate k_{off}, Dex-driven increases in transcription rate k_r during the active state, and combinations of these, are fit to the joint distributions of transcription site activity and mature transcript counts. Model comparison identifies which of these regulatory schemes is best supported by the data, provid-

ing a mechanistic interpretation of the GR-driven transcriptional response in terms of changes to promoter switching dynamics, transcriptional output during the active state, or both.

Aim 3: Discriminate post-transcriptional mechanisms of DUSP1 mRNA regulation through model selection

The third aim extends the promoter-level model from Aim 2 to include nuclear export and cytoplasmic decay of DUSP1 mRNA, and tests alternative formulations of the decay process to identify the minimal post-transcriptional features needed to reproduce the measured response. Four candidate models are compared: a first-order decay model, a time-varying (TV) decay model, a saturable (Sat) decay model, and a combined time-varying and saturable (TV+Sat) model. Each candidate is fit to single-cell distributions of nuclear and cytoplasmic DUSP1 mRNA across the 100nM Dex time-sweep experiments, and models are discriminated based on their ability to capture both the mean and the variance of the response. This analysis establishes the semi-mechanistic TV+Sat formulation as the minimal description required to reproduce both the mean and the cell-to-cell variability of DUSP1 mRNA dynamics following GC stimulation.

Aim 4: Validate the semi-mechanistic model and resolve its mechanistic basis through TTP dynamics

The fourth aim confirms the semi-mechanistic TV+Sat model identified in Aim 3 by predicting single-cell distributions under held-out conditions, including alternative Dex concentrations and transcriptional inhibition by triptolide (TPL). To provide a mechanistic basis for the time-varying and saturable decay, the semi-mechanistic terms are replaced with explicit dynamics for the ARE-binding protein TTP, whose own expression is induced by Dex. The fully mechanistic model is fit jointly to single-cell distributions of nuclear GR, transcription site activity, and nuclear and cytoplasmic mRNA across Dex concentrations, and its predictions are tested against the same held-out conditions used to validate the semi-mechanistic formulation. The aim establishes the relative contributions of transcriptional induction and TTP-mediated post-transcriptional destabilization to

the observed DUSP1 response, and provides a quantitative framework for predicting GC-induced DUSP1 dynamics under conditions beyond those used for parameter inference.

1.7.3 Dissertation organization

The remainder of this dissertation is organized as follows. Chapter 2 presents the experimental and modeling work that addresses Aims 1 through 4, including the ICC and smiFISH measurements, the CME-based models of GR transport and DUSP1 dynamics, the parameter inference and model discrimination results, and the predictive validation against held-out conditions. The content of Chapter 2 originates from a manuscript in preparation for submission, adapted and expanded for dissertation context. Chapter 3 discusses future directions, including the quantification of cytoplasmic degradation dynamics for additional protein and mRNA species, the extension of the modeling framework to longer time scales and to live-cell measurements, and the integration of the GR-DUSP1 model with broader pro- and anti-inflammatory signaling networks. Detailed experimental and computational methods, including ICC protocol development, smiFISH probe validation, image analysis pipelines, and software implementation notes, are provided in the appendices.

Chapter 2

Integrating Single-Cell Experiments and Stochastic Models to Understand and Predict Glucocorticoid Receptor Transport and *DUSP1* mRNA Expression Dynamics

This chapter is adapted from a manuscript currently in review and available as a preprint on bioRxiv (`https://www.biorxiv.org/XXXXX`). The manuscript is co-authored with Alex Popinga, Jack Forman, Luis U. Aguilera, Linda S. Forero Quintero, and Brian Munsky. Content has been adapted and expanded for the dissertation context, and the supplementary materials from the manuscript have been integrated directly into the methods and modeling sections rather than maintained separately. I designed and performed the ICC and smiFISH experiments, conducted the single-cell image analysis, and contributed the biochemical rationale used to formulate and discriminate among the alternative regulatory models presented in this work. I led the writing of the manuscript. Brian Munsky led the development and fitting of the stochastic models and the writing of the modeling methods, with contributions from Alex Popinga, and he contributed to manuscript editing in addition to supervising the project and securing funding. Alex Popinga is the first author of the underlying Stochastic System Identification Toolkit [126], which provides the finite state projection solver and likelihood-based inference machinery used throughout this work. Linda S. Forero Quintero designed the DUSP1 and GAPDH smiFISH probe sets and provided protocol guidance during the initial smiFISH experiments. Luis U. Aguilera initiated the image analysis pipeline used for DUSP1 spot quantification, which Jack Forman and myself subsequently extended and refined into the framework applied here. HeLa Kyoto cells were a gift from the DeLuca Lab. I am grateful to all co-authors and to past and current members of the Munsky and Stasevich Labs for ongoing discussions and feedback.

Chapter Abstract

The over-activation of mitogen-activated protein kinase (MAPK) signaling underlies numerous inflammatory pathologies that are treated using synthetic glucocorticoids, such as dexamethasone (Dex), to activate glucocorticoid receptors (GR) and induce expression of dual-specificity phosphatase 1 (*DUSP1*), which encodes for MAPK phosphatase 1 (MKP1). Despite its importance, the single-cell heterogeneity of this spatial and temporal pathway has not been fully quantified, several regulatory mechanisms are unclear, and accurate quantitative predictions are not possible based on existing models. To address this challenge, we combined immunocytochemistry (ICC) and single-molecule FISH (smiFISH) to quantify endogenous GR transport and *DUSP1* transcription dynamics across thousands of single cells following Dex stimulation. Using Chemical Master Equations (CME) and likelihood-based inference, we identified clear mechanisms and reaction rates for Dex-driven GR nuclear import; compartment-specific GR degradation; GR-dependent modulation of *DUSP1* promoter activation and transcription burst frequencies; DUSP1 transcription, elongation, and transport; and time-dependent and saturation-limited cytoplasmic degradation. Rigorous model comparisons against endogenous, fixed-cell data pinpoints nuclear GR degradation as the dominant mechanism of receptor clearance, indicates that GR primarily regulates promoter activation, and highlights time-dependent AU-rich element (ARE)–mediated mRNA degradation as the dominant mechanism for *DUSP1* clearance. With these mechanisms, the fully-parameterized model quantitatively predicts joint distributions of GR translation and decay dynamics, *DUSP1* transcription site activity, and nuclear and cytoplasmic mRNA heterogeneity among clonal cells as functions of time and across seven orders of magnitude for Dex induction concentrations. Together, these results show that total *DUSP1* mRNA levels emerge from the balance between GR-driven activation and cytoplasmic mRNA decay, with the inferred model quantitatively predicting single-cell distributions across held-out conditions.

2.1 Introduction

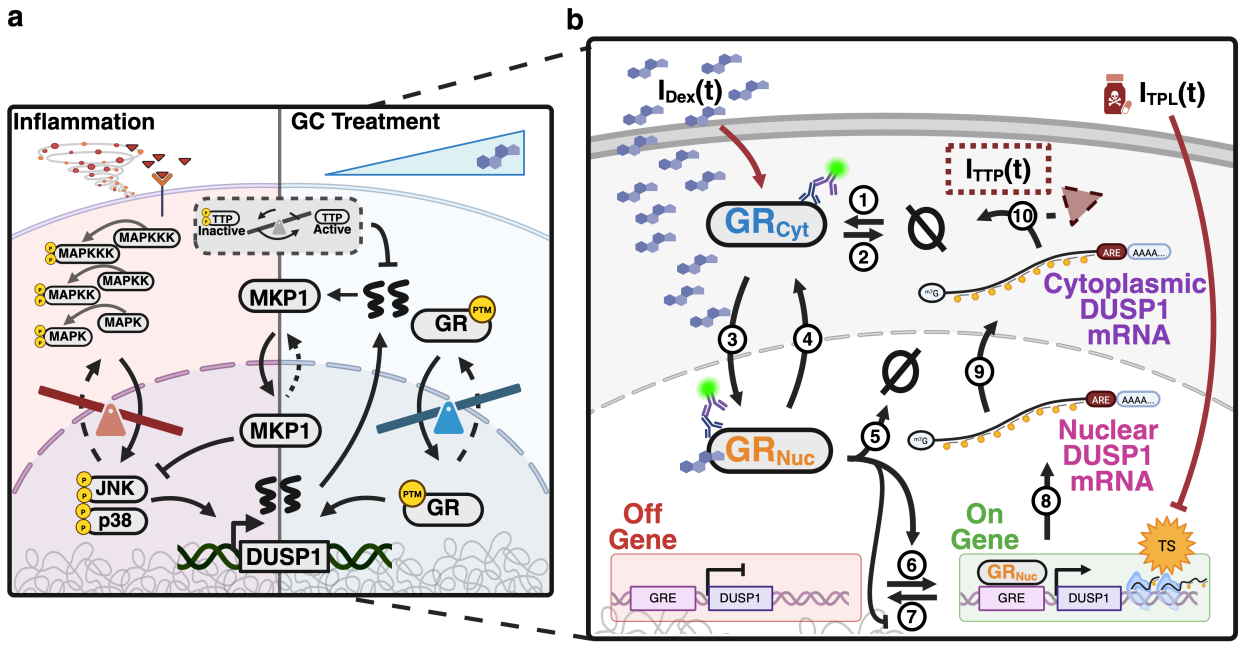


Figure 2.1: Graphical overview and model schematic of GR–DUSP1 signaling.
a Inflammatory signaling activates JNK and p38, inducing *DUSP1* transcription and p38 dependent TTP phosphorylation that stabilizes ARE containing mRNAs. MKP1 dephosphorylates JNK and p38, forming a negative feedback loop. GCs up regulate *DUSP1* via GR to suppress MAPK signaling. **b** Model schematic. HeLa cells are stimulated with multiple concentrations of Dex over three hours to generate a time-dependent Dex signal $I_{\mathrm{Dex}}(t)$. The model accounts for: **(1)** GR synthesis and **(2)** cytoplasmic GR degradation; **(3)** Dex-induced GR translocation to the nucleus; **(4)** nuclear–cytoplasmic shuttling of GR; and **(5)** nuclear GR degradation. Within the nucleus, GR binds to GREs to activate the *DUSP1* promoter, **(6,7)** modeled as stochastic switching between OFF and ON states. **(8)** Transcription produces nascent nuclear DUSP1 mRNA at transcription sites (TS), which are detected by smiFISH, followed by **(9)** export of *DUSP1* mRNA to the cytoplasm and **(10)** ARE-mediated degradation through $I_{\mathrm{TTP}}(t)$. In transcription inhibition experiments, a secondary signal $I_{\mathrm{TPL}}(t)$ represents TPL-mediated suppression of mRNA synthesis during dual Dex–TPL stimulation. Red arrows indicate drug stimulation.

Glucocorticoids (GCs) are cornerstone therapeutics for the treatment of inflammatory and autoimmune diseases, acting through the glucocorticoid receptor (GR) to regulate hundreds of target genes across nearly all tissues [5, 7, 40, 46]. Dexamethasone (Dex) is a high-affinity, long-acting synthetic GC that potently activates GR and serves as a benchmark ligand for mechanistic studies [38]. We focus on HeLa cells, which despite a problematic history [131], are a well-characterized epithelial model with consistent nuclear–cytoplasmic morphology to resolve the sub-

cellular and transcriptional processes underlying Dex-dependent anti-inflammatory responses [38, 69, 131]. Among GR-induced genes, *Dual Specificity Phosphatase 1 (DUSP1)* encodes MAPK phosphatase 1 (MKP1), which dephosphorylates and inactivates the stress kinases p38 and JNK, forming a key negative-feedback loop on inflammatory MAPK signaling (Fig. 2.1a) [12, 23].

The GR is a modular transcription factor whose structure dictates both localization and activity. The ligand-binding domain anchors unliganded GR in cytoplasmic chaperone complexes with HSP90 and FKBP51; the DNA-binding domain recognizes Glucocorticoid Response Elements (GREs); and the intrinsically disordered N-terminal domain harbors activation function-1 and post-translational modification sites that modulate transcriptional potency, nuclear residency, and receptor stability [47, 49, 55, 56, 66, 76]. Upon ligand binding, GR undergoes conformational changes that expose nuclear localization sequences (NLS1 and NLS2), enhancing importin-α/β mediated nuclear import and suppressing CRM1-dependent export [64, 83]. Once in the nucleus, GR binds GREs to activate target genes, but is also subject to ongoing nucleocytoplasmic shuttling and ligand-dependent proteasomal degradation [48, 69, 70, 87]. The balance among import, recycling, degradation, and chromatin engagement thus determines the magnitude and duration of the transcriptional response.

The human *DUSP1* gene resides at 5q35.1, spans approximately 3.1 kb on the reverse strand of chromosome 5 (GRCh38), and comprises four exons and three introns [98] (Fig. 2.9). At GR-regulated promoters, single-molecule and biochemical studies of the MMTV model system have shown that GR can activate transcription through several non-exclusive mechanisms, including increased burst frequency [132], stabilization of the active promoter state [55,68], and enhanced transcription rates within bursts [55,90]. Consistent with these mechanisms, multiple candidate GREs have been mapped upstream of the *DUSP1* transcription start site in A549 cells [133], and at least one site is enriched for both GR and the coactivator p300 alongside increased chromatin accessibility and histone acetylation [134], though GR binding and chromatin context can vary across cell types [91]. Nascent *DUSP1* transcripts accumulate at transcription sites (TS) and appear as bright nuclear foci under smFISH imaging (Fig. 2.11), with intensities brighter than multiples of the av-

erage single diffraction-limited mRNA [118] (Fig. 2.9). Following processing and export through nuclear pore complexes, mature *DUSP1* mRNAs enter the cytoplasm, where they are translated into MKP1 or targeted for degradation. The *DUSP1* mRNA contains AU-rich elements (AREs) in its 3' UTR (Fig. 2.9), making it a substrate for ARE-binding proteins, such as tristetraproline (TTP), which can accelerate mRNA turnover [12, 35, 37, 104, 105]. Consequently, ligand-induced *DUSP1* expression arises from a balance between GR-driven transcriptional activation, receptor down-regulation, and cytoplasmic mRNA decay.

Previous modeling efforts have captured important aspects of GR-mediated transcriptional regulation using a range of approaches. Equilibrium thermodynamic models of ligand–GR–coregulator–DNA interactions have described how allosteric coupling gives rise to ligand- and gene-specific transactivation at steady state [59]. ODE models have simulated the kinetics of GR autoregulation and induction of target genes such as *BIM* and *GILZ* in GC-sensitive and -resistant leukemia cell lines [127]. Multivariate statistical approaches have demonstrated that GR Ser211 phosphorylation is a stronger predictor of endogenous target gene responses than conventional reporter assays [60], and Boolean models of the GR interactome have provided qualitative predictions of signaling states associated with GC sensitivity and resistance [51]. However, these approaches either operate at steady state or on population-averaged quantities, and none integrates subcellular spatial resolution with stochastic single-cell dynamics to mechanistically link GR activation to the heterogeneous transcriptional responses observed at the single-cell level.

To complement and expand upon previous investigations of GR and DUSP1, our approach integrates single-cell imaging of endogenous targets with stochastic modeling to capture the spatial and temporal dynamics of GR signaling coupled with downstream regulation of DUSP1 transcription. Using fixed-cell ICC and smiFISH measurements of GR localization and *DUSP1* mRNA abundance (see Methods), we quantitatively link nuclear–cytoplasmic transport to promoter activation and mRNA decay. By explicitly modeling the probabilistic nature of transcription and degradation, our framework predicts not only mean transcriptional responses but also the full distributions of inter- and intracellular heterogeneity that are inaccessible to bulk assays, live-cell

reporters, or exogenous constructs. Measurements of cell-to-cell variability provide a sensitive *fluctuation fingerprint* to interrogate gene regulatory mechanisms [31], often offering more information than averaged population data [115]. When single-molecule measurements are integrated with discrete stochastic models, they enable rigorous identification of kinetic parameters governing gene regulation dynamics [32,103]. By comparing single-cell data against multiple different model hypotheses within the framework of the Chemical Master Equation (CME), we infer the most probable mechanisms and parameters to achieve a highly predictive quantitative model for GR nuclear import and degradation, GR-modulated promoter activation, DUSP1 transcriptional elongation, and ARE-mediated mRNA decay (Fig. 2.1b). This integrative modeling approach clarifies how GR-dependent transcriptional and post-transcriptional processes jointly shape the heterogeneous single-cell responses observed across Dex stimulation and triptolide (TPL)-mediated transcription inhibition conditions.

2.2 Results

To realize this integrative approach, we constructed a semi-mechanistic stochastic model of the coupled GR–DUSP1 system, the structure of which is summarized in Fig. 2.1b. The model is comprised of three modules: (*i*) GR transport regulation defined by **reactions 1-5**, (*ii*) DUSP1 transcription and transport regulation defined by **reactions 6-9**, and (*iii*) DUSP1 degradation regulation defined by **reaction 10**. The mechanisms and parameters of these modules are sequentially inferred from single-cell ICC (Module *i*) and smFISH data (Modules *ii* and *iii*) as described in the following sub-sections.

2.2.1 Subcellular ICC measurements reveal heterogeneous GR translocation dynamics

To quantify endogenous GR dynamics in response to GC stimulation, HeLa cells were treated with 1, 10, or 100 nM Dex for six different time periods (10, 30, 50, 75, 120, 180) min in addition

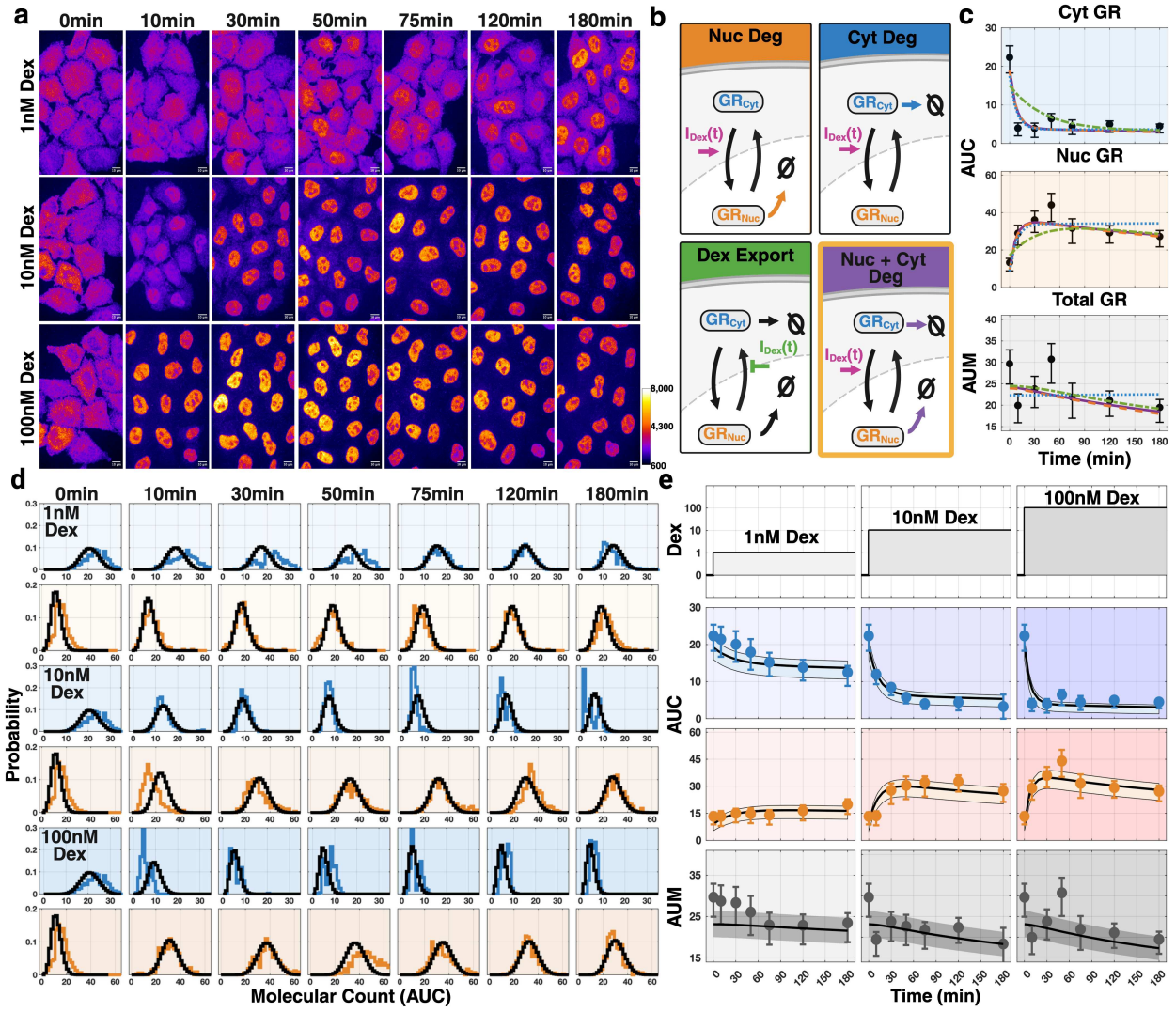


Figure 2.2: Subcellular GR translocation.
(a) Representative HeLa cells stained for GR by ICC at selected times following continuous Dex stimulation (1 nM, 10 nM, 100 nM). Intensities scaled by background. **(b)** Candidate GR models, each comprising cytoplasmic and nuclear GR species with Dex stimulation $I_{\mathrm{Dex}}(t)$ driving nuclear import. The variants differ in GR removal: nuclear degradation only (Nuc Deg, orange), cytoplasmic degradation only (Cyt Deg, blue), Dex-modulated nuclear export (Dex Export, green), and combined nuclear and cytoplasmic degradation (Nuc + Cyt Deg, purple). The Nuc + Cyt Deg model (gold outline) provided the best fit. **(c)** Cytoplasmic (Cyt GR), nuclear (Nuc GR), and total (Total GR) GR versus time. Measured medians and upper/lower quartile ranges (black, circles and bars) are compared with FSP fits for each candidate model, colored as in (b): Nuc + Cyt Deg (purple), Nuc Deg only (orange), Cyt Deg only (blue), and Dex Export (green). **(d)** Measured distributions of cytoplasmic (blue) and nuclear (orange) GR concentration at each time point and Dex dose (1 nM, 10 nM, 100 nM), compared with FSP model fits (black). **(e)** Dex input profiles (top) and temporal trajectories of 25/50/75 percentiles for cytoplasmic GR (AUC, blue), nuclear GR (AUC, orange), and total GR mass (AUM, gray) at each dose. Measured medians and upper/lower quartile ranges are shown by circles and bars, and the corresponding model fits are shown by solid lines and shading.

to an unstimulated control. Representative ICC images (Fig. 2.2a), which were verified against isotype and secondary control experiments (Supplementary Fig. S3), illustrate three key features of GR localization. First, unstimulated HeLa cells exhibit a heterogeneous distribution of GR, with a mean nuclear-to-cytoplasmic (N/C) intensity ratio of 1.05 (CV=11%, $n = 430$ cells), reflecting low to moderate nuclear GR in most cells (Fig. 2.2a,d,e, Supplementary Table 1). This ligand-independent nuclear localization is consistent with prior reports [64, 72, 111]. At 1 nM, the population N/C ratio rises slowly and reaches only 1.72 by 180 min, whereas 10 and 100 nM produce faster and larger shifts, with peak N/C ratios of 3.26 at 75 min and 3.53 at 30 min, respectively. Variability in the cytoplasmic intensity distribution decreases as cells deplete cytoplasmic GR, with the CV dropping from 17% in unstimulated cells to 8% at 10 nM/75 min (Table 2.1). Third, the total amount of GR decreases across all conditions, with faster rates of depletion for higher concentrations of Dex (Fig. 2.2d).

2.2.2 A stochastic model of Dex-driven nuclear import and compartment-specific degradation captures GR dynamics

To interpret the measured GR spatial and temporal transport dynamics (i.e., ***CytGR*** and ***NucGR*** as functions of time and Dex concentration), we constructed a flexible GR model (Module *i*) and used it to compare competing hypotheses for how Dex controls GR transport and where GR is degraded (Fig. 2.2b).

The model couples cytoplasmic and nuclear GR through nucleocytoplasmic transport, with Dex supplied as a time-varying signal $I_{\mathrm{Dex}}(t) = I_0 \mathrm{e}^{-\gamma_{\mathrm{Dex}} t}$, where I_0 is the supplied Dex concentration and γ_{Dex} is its first order decay rate, and with Dex-stimulated transport following Michaelis-Menten kinetics to allow for saturation at higher concentrations. We evaluated four candidate models (Fig. 2.2b, Fig. S4): three in which Dex drives nuclear import while GR degradation is restricted to the nucleus, restricted to the cytoplasm, or active in both compartments, and one in which Dex instead suppresses nuclear export.

To distinguish among these candidates, we fit each model independently to the single-cell ICC data. By solving the CME using Finite State Projection (FSP) [126] and searching over parameter space, we found the maximum likelihood estimate (MLE) for each model, and we accounted for differences in model complexity using the Bayesian Information Criteria (BIC). Table 2.2 provides a complete comparison of log-likelihoods and BIC values. The Dex export model gave the poorest agreement with the cytoplasmic and nuclear GR data (Supplementary Fig. S4), even though it still captured total GR, and the cytoplasm-only degradation model overestimated nuclear GR at later times and predicted essentially no change in total GR (Fig. 2.2c, Supplementary Fig. S4). The nucleus-only and compartment-specific degradation models produced very similar fits to the cytoplasmic, nuclear, and total GR dynamics (Fig. 2.2c, Supplementary Fig. S4), but the compartment-specific model achieved the highest log-likelihood and the lowest BIC of the four candidates, remaining favored even after penalizing for its additional degradation parameter(Table 2.2). An approximate Bayes factor (BF) reached the same conclusion, favoring the compartment-specific model over every alternative, including by roughly 90-fold over the next-best nucleus-only model (Table 2.2).

Figure 2.2d shows the resulting fits to the nuclear and cytoplasmic GR distributions as functions of time and Dex concentration, and Figure 2.2e summarizes these distributions to show the measured and model-fitted median, 25^{th} and 75^{th} percentile levels for GR concentrations in the nucleus and cytoplasm and the total GR mass. For all Dex concentrations and times, the compartment-specific degradation model simultaneously reproduces the measured nuclear, cytoplasmic, and total GR distributions (Fig. 2.2d,e), (Table 2.5) shows the inferred parameters for the compartment-specific degradation GR model, with uncertainties inferred using Metropolis Hastings assuming broad lognormal prior distributions with standard deviations of two orders of magnitude for each parameter (see methods).

By comparing the rates of nuclear (γ_{GRnuc}) and cytoplasmic (γ_{GRcyt}) GR degradation inferred from the ICC data (Supplementary Table S3), we found that nuclear degradation was faster by approximately 3-fold, supporting ligand-induced nuclear proteasomal degradation as a key mech-

anism of GR deactivation [69, 78, 86, 87]. Consistent with this interpretation, cytoplasmic GR antibody intensity did not reappear at later times, and total GR levels declined more rapidly at higher Dex concentrations, when a greater fraction of GR was nuclear (Fig. 2.2d,e). Inferred transport rates also recapitulated the expected pattern of ligand-dependent shuttling [64, 83]: under unstimulated conditions, the nuclear export rate ($k_{\mathrm{nc}} \approx 0.02$ min^{-1}) exceeded the basal import rate ($k_{\mathrm{cn0}} \approx 0.006$ min^{-1}), favoring cytoplasmic localization, while 100 nM Dex-stimulated import ($k_{\mathrm{cn0}} + k_{\mathrm{cn1}} I_{\mathrm{Dex}}(t) \approx 11.5$ min^{-1}) was much higher, driving rapid and nearly complete nuclear accumulation (Table 2.2). Together these findings reproduced the observations that 1 nM stimulation maintained the highest total GR (Nuc + Cyto) across all stimulatory conditions, while 100 nM produced the fastest and most uniform transport induction followed by the most rapid decline in both ***NucGR***, ***CytGR***, and ***Total GR*** (Fig. 2.2e, Fig. 2.5a).

2.2.3 Single-molecule measurements reveal stochastic *DUSP1* transcription dynamics

To quantify early transcription of endogenous *DUSP1* mRNA, we designed a smiFISH probe set targeting exonic regions of the human *DUSP1* transcript (Fig. 2.9) [117]. *GAPDH* smiFISH probes served as a cytoplasmic marker to enable automated single-cell segmentation (Fig. 2.3a, Fig. 2.11). Images were analyzed using a custom implementation of BigFISH [118]. A combined compartment-based and local signal-to-noise ratio (SNR) thresholding strategy yielded the most reliable spot detection, as verified visually (2.1) (Fig. 2.11). This approach substantially reduced false positives and enabled consistent identification of transcription sites (magenta), nuclear mRNAs (blue), and cytoplasmic mRNAs (purple) (Fig. 2.3a), with minor expected imperfections (Fig. 2.11). Once identified, candidate spots were post-processed and separated into TS's and mature mRNA (Fig. 2.3a, Fig. 2.11).

At 100nM stimulation, and across all time points, *DUSP1* expression remained heterogeneous at the single-cell level (Fig. 2.3c,d, Fig. 2.4). The fraction of cells that had one or more active TS increased rapidly after stimulation and peaked at roughly 30–40 minutes, while the intensity

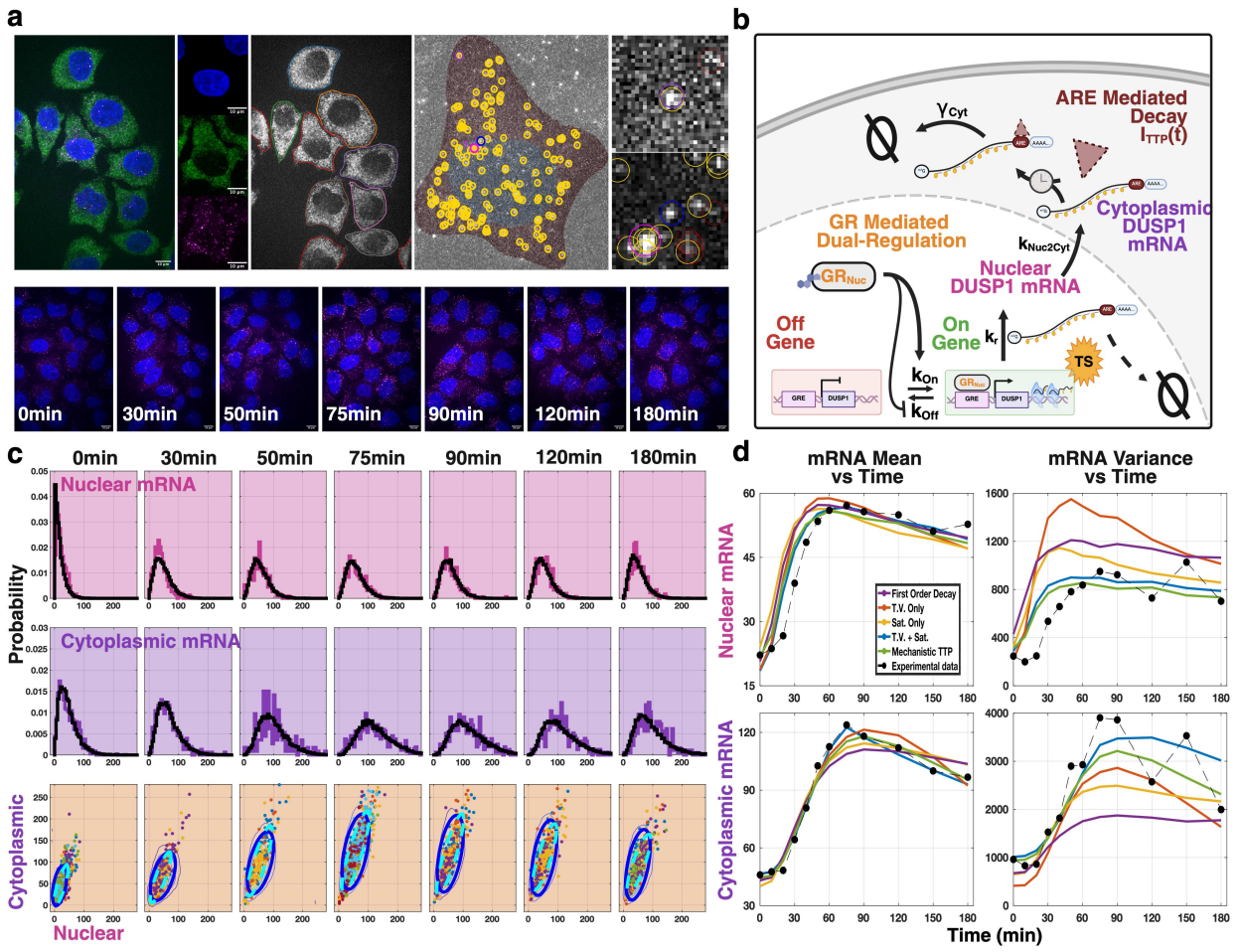


Figure 2.3: Subcellular *DUSP1* transcriptional regulation.
(a) Top: single-cell segmentation and smiFISH spot detection workflow. From left to right: merged three-color image of a representative field of view; zoomed view of a selected cell with individual DAPI, *GAPDH* smiFISH, and *DUSP1* smiFISH channels; cytoplasmic segmentation with partial peripheral cells excluded; nuclear and cytoplasmic segmentation overlaid with detected *DUSP1* mRNA; example spot crops with cytoplasmic (top) and nuclear (bottom) detections. Gold circles indicate accepted mRNA detections, magenta circles denote transcription sites, and red circles mark low-SNR candidates removed during filtering. Bottom: representative merged *DUSP1* smiFISH and DAPI images following 100 nM Dex stimulation at the indicated time points. Scale bars, 10 µm. **(b)** Schematic of the stochastic model linking GR-dependent transcriptional activation to *DUSP1* mRNA production, nuclear export, and ARE-mediated cytoplasmic degradation. **(c)** Distributions of nuclear (top) and cytoplasmic (middle) *DUSP1* mRNA at the indicated time points, shown with corresponding model fits. Histogram colors denote experimental replicates. Bottom row shows joint nuclear, cytoplasmic mRNA distributions with data as points and 95% confidence ellipses. **(d)** Mean (left column) and variance (right column) of nuclear (top row) and cytoplasmic (bottom row) *DUSP1* mRNA over time, comparing experimental measurements to candidate model fits (First Order Decay, T.V. Only, Sat. Only, T.V. + Sat., Mechanistic TTP).

of active TS remained relatively constant (Fig. 2.5a). TS activation was followed by the rise in nuclear mRNA, which reached a maximum near 75 minutes (Fig. 2.5a). Nuclear and cytoplasmic

mRNA levels then peaked between 75–90 minutes (Fig. 2.3d, Fig. 2.5a) before declining, with a more pronounced decrease observed in the cytoplasm (Fig. 2.3c,d). DUSP1 mRNA distributions were highly variable with Fano factors (i.e., variance/mean) of 11.1 $\pm$ 2.9 (at 0 min) to 16.6 $\pm$ 2.5 (at 90 min) for nuclear mRNA and with much higher cytoplasmic Fano factors of 20.9 $\pm$ 3.5 (at 0 min) to 32.7 $\pm$ 6.4 (at 90 min).

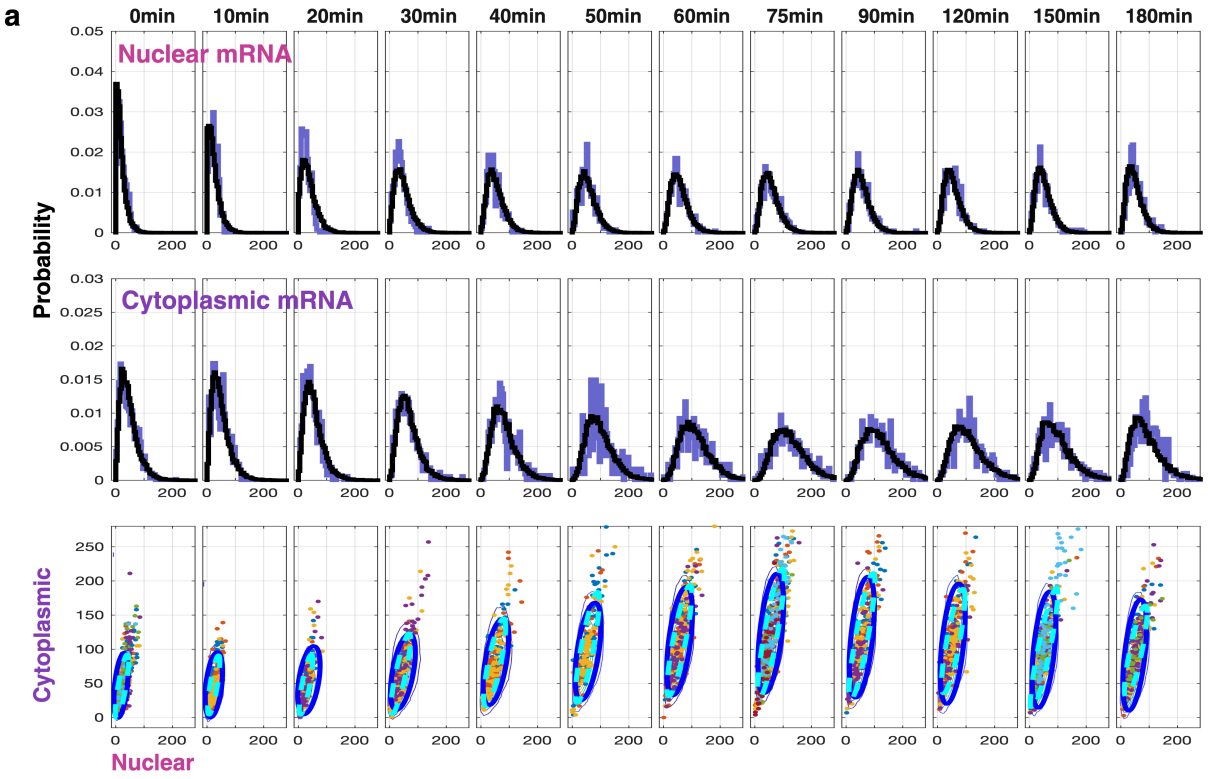


Figure 2.4: Model fits and predictions for *DUSP1* mRNA dynamics at 100 nM Dex.
(a) Distributions of nuclear and cytoplasmic *DUSP1* mRNA at all sampled time points following 100 nM Dex stimulation. Colored histograms show experimental measurements, with black curves indicating the corresponding model fits. Bottom row shows joint nuclear–cytoplasmic mRNA distributions, with data shown as points and model-fitted 95% confidence ellipses.

2.2.4 Stochastic modeling shows that nuclear GR increases *DUSP1* transcription burst frequencies

To build a quantitative understanding for the control of *DUSP1* regulation, we extended the GR model from above (Module *i*) with a transcription and nuclear-transport module (Module *ii*) comprising three additional biochemical species (Fig. 2.1b): inactive gene copies (***offGene***), active gene copies (***onGene***), and nuclear mRNA transcripts (***rNuc***). To capture the stochastic dynamics of these species, we adopt the standard two-state bursting gene expression model [31]. In this model, ***offGene***, ***onGene***, and ***rNuc*** populations are controlled through four additional reactions: allele activation (**reaction 6**: ***offGene*** $\rightarrow$ ***onGene***), allele deactivation (**reaction 7**: ***onGene*** $\rightarrow$ ***offGene***), transcription (**reaction 8**: ***onGene*** $\rightarrow$ ***onGene*** + ***rNuc***), and nuclear degradation or transport of mRNA from the nucleus to the cytoplasm (**reaction 9**: ***rNuc*** $\rightarrow \emptyset$, or ***rNuc*** $\rightarrow$ ***rCyt***). For (**reaction 8**), the model allows for different transcription rates for when alleles are in the ***offGene*** or ***onGene*** states. The model was assumed to have a total of two *DUSP1* alleles per cell, consistent with observations that the vast majority (98.9%) of cells were detected to contain zero, one, or two observable TS per cell.

We reasoned that the finding that application of 100 nM Dex leads to increased *DUSP1* activity could be explained by multiple distinct mechanisms in the context of the bursting gene expression model. GR could increase the promoter activation rate (k_{on} in **reaction 6**), decrease the promoter deactivation rate (k_{off} in **reaction 7**), or increase the transcription rate during the ON state (k_{r} in **reaction 8**), or act through some combination of these effects (Supplementary Fig. S6). Depending upon model parameters, these mechanism can predict distinct and quantitatively revealing relationships between the fraction of cells with active TS or the distributions of nascent mRNA per active TS or mRNA counts per cell [31, 103].

To select among the proposed models, we searched over parameter space to maximize the likelihood of the smFISH data for the number of mRNA per cell and the distribution for the total intensity of the transcription sites (or in the rare case where more than two TS are detected, the total of the two brightest TS). The resulting likelihood-based comparisons strongly favored GR

regulation of the promoter activation rate k_{on} as the dominant mechanism: the likelihood ratio LR in favor of k_{on} over k_{r} alone was $LR = e^{83}$, and over k_{off} alone was $LR = e^{38}$ (Fig. 2.12). Consistent with this, a model in which GR acts exclusively through k_{on} achieved the best likelihood for TS abundance among all single-action models, while the combined $k_{\mathrm{on}}\&k_{\mathrm{off}}$ model yielded the best overall MLE fit and BIC values (Fig. 2.12). In the smiFISH data, we found that Dex stimulation produces a substantial increase in the fraction of *DUSP1* alleles exhibiting detectable TS, while the mean and the distributions of TS intensity show relatively small changes over time (Fig. 2.5a), a pattern that is most consistent with increased burst frequency through increases in k_{on} rather than increased burst size through decreases in k_{off} or increases in k_{r} [103].

Although the single strongest regulatory interaction was found to be an increase in k_{on}, models that also included GR-dependent decreases in k_{off} yielded modest improvements in likelihood of the observed numbers for mature mRNA per cell (Fig. 2.12). Models incorporating GR-dependent changes in k_{r} provided no meaningful improvement in fit, with the full three-parameter model ($k_{\mathrm{on}}/k_{\mathrm{off}}/k_{\mathrm{r}}$) performing comparably to the two-parameter model and carrying a higher BIC penalty. Our final model therefore retains GR regulation of k_{on} as the dominant mechanism (thick line), with weaker modulation of k_{off} (thin line) (Fig. 2.1b, Fig. 2.13). The final inferred set of semi-mechanistic model parameters and uncertainties can be found is Table 2.7.

2.2.5 Subcellular measurements reveal complex dynamics of *DUSP1* mRNA transport and degradation

To extend our GR and *DUSP1* promoter-level analyses to include the full *DUSP1* mRNA life cycle, we next examined the relationships between nuclear and cytoplasmic mRNA distributions (Fig. 2.3c,d, Fig. 2.14). At early times, following a short delay after addition of Dex, the average level of cytoplasmic mRNA increases rapidly to reach a maximum level shortly after that of the nuclear mRNA. These observations were expected since cytoplasmic mRNA accumulation follows behind that of the nucleus with a delay set by the nucleus to cytoplasm transport rate. However, upon comparing the distributions of nuclear and cytoplasmic mRNA at later times (Fig 2.3d,e), we

made two surprising key observations: First, after reaching its maximum value, the average level of cytoplasmic mRNA rapidly decreases, which is surprising given that the average level of nuclear mRNA decreases only slightly below its maximal value. Second, at later times, the relative level of heterogeneity in the number of cytoplasmic mRNA (e.g., $FF_{\mathrm{cyt}} = 32.7 \pm 6.4$ at t = 90 min) is much wider than that of the nuclear mRNA ($FF_{\mathrm{nuc}} = 16.6 \pm 2.51$), which was surprising given that the cytoplasmic mean number ($\mu_{\mathrm{cyt}} = 118.0$) is more than twice as large as that of nuclear mRNA ($\mu_{\mathrm{nuc}} = 55.7$) at the same time.

2.2.6 Spatial stochastic modeling identifies ARE-mediated decay as the dominant cytoplasmic clearance mechanism

To extend our model to capture these observations, we added a cytoplasmic degradation module (Module *iii*) with an additional species for cytoplasmic mRNA (***rCyt***), which increases via the previous transport reaction (**reaction 9**) and decays according to **reaction 10** ($rCyt \rightarrow \emptyset$). During preliminary parameter inference, we found that the nuclear mRNA degradation pathway (Fig. 2.3b, dashed line) was consistently driven to negligible values, and thus we only consider cytoplasmic decay from this point onward.

We proposed and evaluated four candidate cytoplasmic decay models of varying levels of complexity (Fig. 2.14): (i) a standard model of constant first-order decay, (ii) a model where the degradation rate saturates at high levels of mRNA, (iii) a model where the degradation rate increases over time, and (iv) a model with both saturation and time-dependence in the degradation rate. Mechanism (ii) was inspired by the work of Hansen et al [135], who demonstrated that higher variability in the cytoplasm could be explained by a biphasic degradation mechanism, where distinct subsets of mRNA exhibit different degradation rates. For example, ARE–dependent cytoplasmic degradation could lead to increased degradation of mRNA but only if sufficient quantities of ARE-binding proteins are available. Similarly, mechanism (iii) was inspired by the knowledge that the ARE-binding protein TTP is known to be induced by Dex [37, 136, 137].

Upon fitting the extended models to simultaneously capture TS intensities, nuclear mRNA, and cytoplasmic mRNA, we found that all degradation models could reproduce the average levels of both nuclear and cytoplasmic mRNA as functions of time (Fig. 2.3d, top left and bottom left). The models diverged sharply, however, in their ability to reproduce the heterogeneity of the mRNA distributions. Without a saturation term to constrain the degradation rate, the simpler models could not capture the joint variability in both compartments: their best fits substantially over-estimated nuclear variability (Fig. 2.3d, top right) or under-estimated cytoplasmic variability (Fig. 2.3d, bottom right). Only the semi-mechanistic model incorporating both time-varying and saturating degradation (T.V. + Sat.) and the full mechanistic TTP model captured the nuclear and cytoplasmic variances while simultaneously fitting both means (Fig. 2.3d, Fig. 2.14).

These qualitative observations were supported by quantitative comparisons of the models' fits to the data (Table 2.7), showing that the best fits consistently and overwhelmingly favored ARE-mediated degradation mechanisms that include both time dependence and saturation with respect to cytoplasmic mRNA abundance. This result matches closely to our key qualitative observations above: First, the time dependent increase in the cytoplasmic decay rate is needed to achieve the rapid average reduction in cytoplasmic mRNA that is observed at later times. Second, the saturation effect on the degradation rate is needed to allow mRNA to survive longer when they are already more abundant, which leads to a longer tail in the cytoplasmic mRNA distribution.

Together, these results suggest that ARE-mediated, time-varying, and saturable cytoplasmic degradation is the dominant mechanism governing *DUSP1* mRNA clearance following GC stimulation. This Dex-dependent, but variable, acceleration of cytoplasmic mRNA turnover is consistent with recent studies demonstrating enhanced *DUSP1* degradation through ARE-binding proteins such as TTP [37].

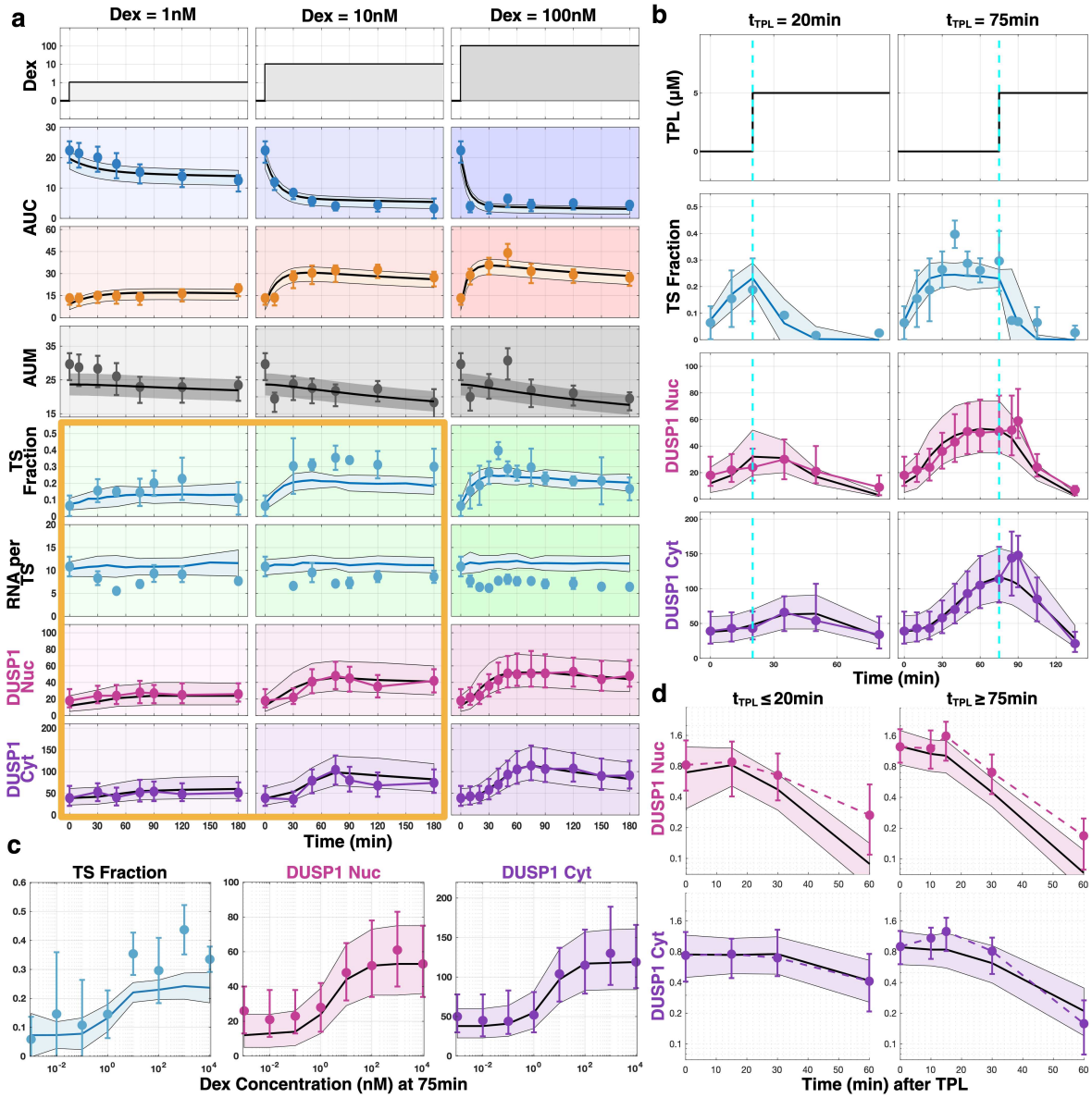


Figure 2.5: Model fits and predictions across Dex concentrations and transcription inhibition conditions. **(a)** Joint GR and *DUSP1* time courses at 1, 10, and 100 nM Dex. The top three rows show fits to cytoplasmic GR concentration (arbitrary units of concentration, AUC, blue), nuclear GR concentration (AUC, orange), and total GR mass (arbitrary units of mass, AUM, gray). The bottom four rows show *DUSP1* TS fraction, RNA per TS, nuclear mRNA (*DUSP1* Nuc), and cytoplasmic mRNA (*DUSP1* Cyt). The semi-mechanistic model was fit to the GR data and the 100 nM *DUSP1* column; the gold outline marks the 1 and 10 nM columns, which are predictions generated without refitting. **(b)** Dex–TPL dual-stimulation predictions for early ($t_{\mathrm{TPL}} = 20\,\mathrm{min}$) and late ($t_{\mathrm{TPL}} = 75\,\mathrm{min}$) transcriptional inhibition. Cells were first stimulated with 100 nM Dex, followed by 5 μM TPL added at t_{TPL}; cyan dashed lines mark TPL addition. **(c)** Dex-titration predictions at $t = 75\,\mathrm{min}$ spanning 1 pM to 10 μM. **(d)** Compartment-specific *DUSP1* mRNA decay after TPL, grouped into early ($t_{\mathrm{TPL}} \leq 20\,\mathrm{min}$) and late ($t_{\mathrm{TPL}} \geq 75\,\mathrm{min}$) inhibition. The y-axis is compartment-specific mRNA normalized for TPL onset, *DUSP1* elongation, and nuclear-to-cytoplasmic export. Cytoplasmic decay rates increase substantially at later times while nuclear rates remain similar, consistent with time-dependent ARE-mediated turnover. Panels (b)–(d) are predictions from the semi-mechanistic model without refitting. In (a) and (c), TS fraction and RNA per TS are mean ± standard deviation; all other data are median ± interquartile range (25th/75th percentiles).

2.2.7 Model predictions across Dex concentrations and transcriptional inhibition conditions

After fitting to the single-cell GR ICC measurements measurements at 1, 10, and 100 nM Dex and the smiFISH measurements at 100 nM Dex, we next asked if our fully parameterized model could quantitatively predict *DUSP1* transcriptional outputs across other Dex concentrations. To extend the model to the new levels of Dex without introducing new parameters or mechanisms, we assumed that the impact of Dex on the time variation of cytoplasmic degradation should scale linearly with the increase of GR in the nucleus. Model predictions for TS fraction, RNA per TS, and nuclear and cytoplasmic *DUSP1* mRNA were validated experimental measurements at both 1 nM and 10 nM Dex across all sampled time points (Fig. 2.5a). Importantly, these predictions capture both mean behaviors and observed variances, indicating that the stochastic structure of the model accurately extrapolates to predict cell-to-cell heterogeneity (Fig. 2.6 2.7).

To further challenge the model's ability to predict promoter activity, we performed a Dex concentration sweep spanning over four orders of magnitude and measured *DUSP1* mRNA abundance at a fixed stimulation time of 75 min. Without refitting, the model accurately predicted both nuclear and cytoplasmic *DUSP1* mRNA counts across concentrations ranging from 1 pM to 10 μM (Fig. 2.5c). The resulting dose–response relationship exhibits a characteristic sigmoidal shape, reflecting saturation of GR transport, GR-dependent promoter activation, and downstream transcriptional output. We confirmed that our final model consistently made more accurate predictions than any of the other discarded models (Fig. 2.3d, Fig. 2.14, and Table 2.7).

To validate the inferred cytoplasmic decay mechanisms, we next examined the model's ability to predict *DUSP1* dynamics under transcriptional inhibition. Dual-stimulation experiments were performed in which cells were first treated with 100 nM Dex and subsequently exposed to 5 μM TPL at defined times following Dex addition. TPL is known to block transcriptional initiation, providing a stringent perturbation of promoter activity [138]. Consistent with model predictions, TS frequency decreased rapidly to near zero following TPL addition at all tested time points, indicating transcriptional shutoff in 10 minutes of less. Model predictions accurately captured the sub-

sequent temporal evolution of nuclear and cytoplasmic *DUSP1* mRNA following transcriptional arrest (Fig. 2.5d), with nuclear and cytoplasmic mRNA distributions and joint nuclear–cytoplasmic distributions for each TPL timing shown in Figure 2.8.

To focus directly on the model's prediction of a temporal change in the cytoplasmic degradation rate, Figure 2.5d shows the predicted and measured post-TPL decay rates for pooled and normalized data before and after 75 min following Dex. At early inhibition times, the observed decay rate was 0.0140 ± 0.0036 min^{-1}, and at later times the decay measured to be significantly higher at 0.0376 ± 0.0073 (one sided T-test, p = 0.0066). These relative decay rates were well predicted by the model, which estimated an effective decay rate of 0.0131 ± 0.0045 min^{-1} at early times and 0.0316 ± 0.0019 min^{-1} at later times.

Together, these results demonstrate that the inferred models for GR transport and degradation, GR-mediated transcriptional activation, and ARE-mediated cytoplasmic decay mechanisms are sufficient to predict temporal and spatial aspects of *DUSP1* mRNA dynamics across Dex concentrations and under acute transcriptional inhibition.

2.3 Discussion

Here we combined single-cell ICC, smiFISH, and stochastic modeling to quantitatively link GR transport with transcriptional and post-transcriptional regulation of the endogenous anti-inflammatory gene *DUSP1*. By fitting discrete stochastic models directly to joint distributions of nuclear and cytoplasmic GR, transcription site activity, and mRNA abundance, we moved beyond mean responses to resolve how variability and timing emerge from the underlying regulatory processes. This integrative framework captures not only the magnitude but also the heterogeneity and temporal ordering of GR-dependent transcriptional responses, providing a quantitative description of how GC signaling propagates from receptor activation to mRNA clearance at the single-cell level.

Our analysis supports a model in which Dex primarily drives GR nuclear accumulation through enhanced import, followed by concentration-dependent nuclear degradation that modulates *DUSP1*

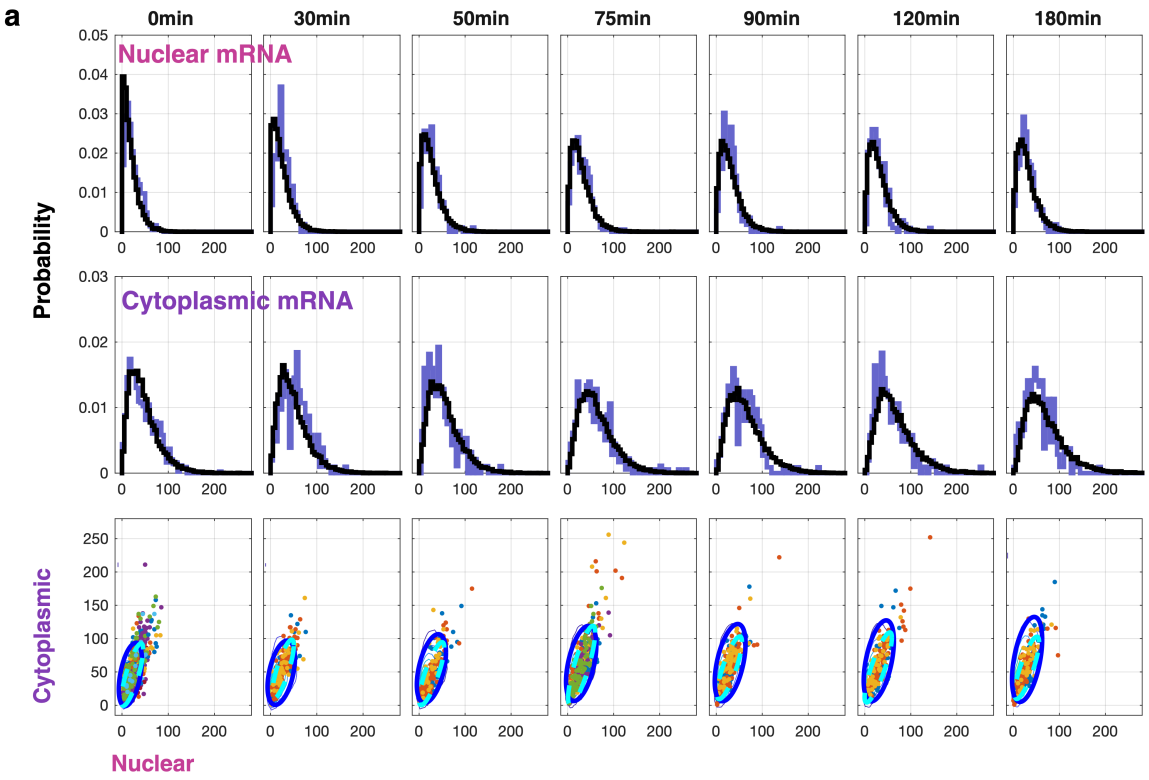


Figure 2.6: Model fits and predictions for *DUSP1* mRNA dynamics at 1 nM Dex.
(a) Distributions of nuclear and cytoplasmic *DUSP1* mRNA at the indicated time points following 1 nM Dex stimulation. Colored histograms show experimental measurements, with black curves indicating the corresponding model fits. Bottom row shows joint nuclear–cytoplasmic mRNA distributions, with data shown as points and model-predicted 95% confidence ellipses.

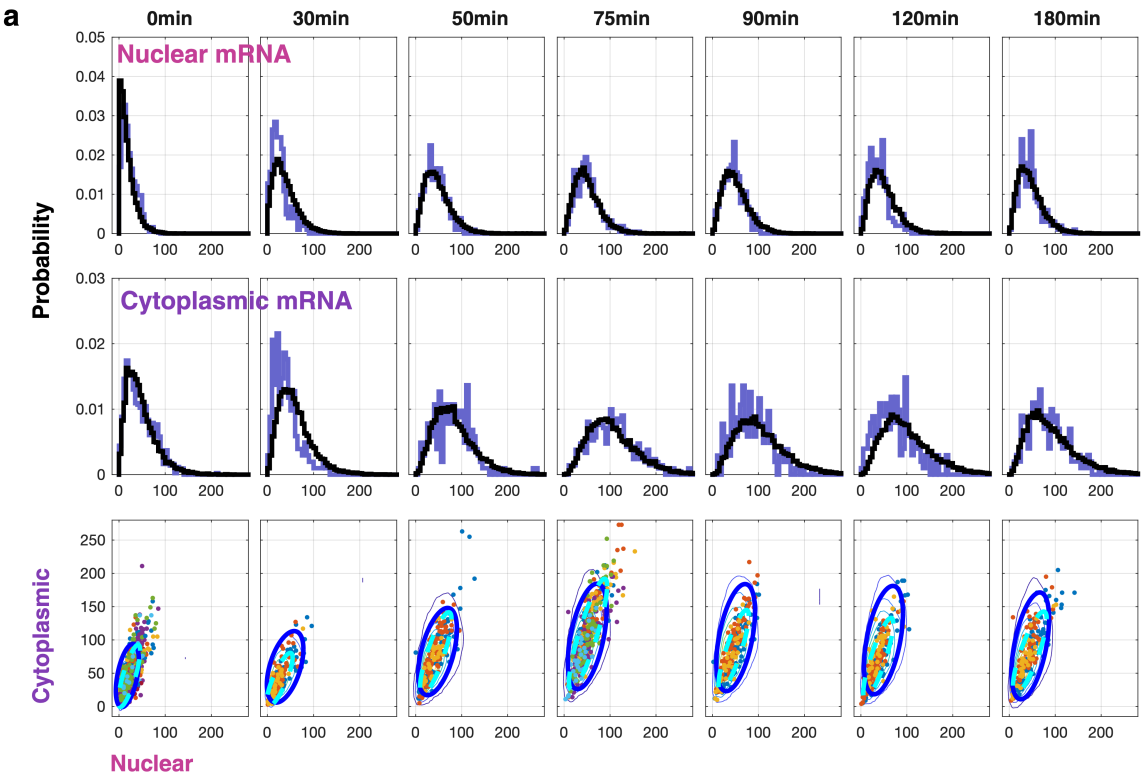


Figure 2.7: Model fits and predictions for *DUSP1* mRNA dynamics at 10 nM Dex.
(a) Distributions of nuclear and cytoplasmic *DUSP1* mRNA at the indicated time points following 10 nM Dex stimulation. Colored histograms show experimental measurements, with black curves indicating the corresponding model fits. Bottom row shows joint nuclear–cytoplasmic mRNA distributions, with data shown as points and model-predicted 95% confidence ellipses.

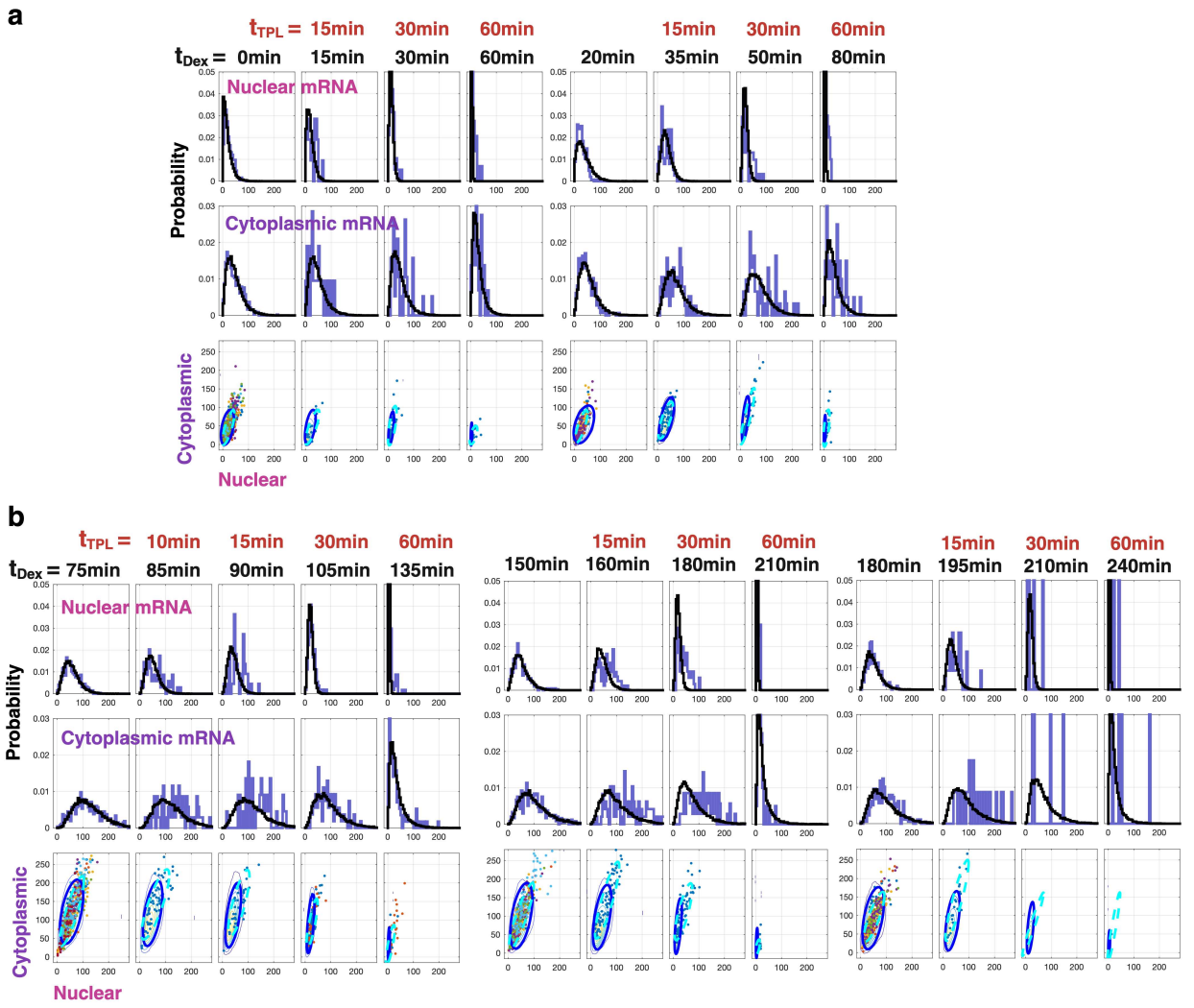


Figure 2.8: *DUSP1* mRNA distributions under transcriptional inhibition by TPL.
(a) Distributions of nuclear and cytoplasmic *DUSP1* mRNA and joint nuclear–cytoplasmic mRNA distributions across all sampled time points following transcriptional inhibition. Green-shaded panels correspond to control time points under 100 nM Dex stimulation without TPL (0, 20, 75, 150, and 180 min), while yellow-shaded panels correspond to time points following addition of 5 µM TPL. Colored histograms show experimental measurements, with black curves indicating the corresponding model predictions. Bottom rows show joint nuclear–cytoplasmic mRNA distributions, with data shown as points and model-predicted 95% confidence ellipses.

transcriptional output. This compartment-specific turnover provides a natural explanation for the observed dose-dependent rise and decline of nuclear GR, particularly at higher Dex concentrations where nuclear GR peaks early and decays rapidly. Such dynamics are consistent with proteasome-mediated clearance [69, 78, 86, 93] acting as a built-in deactivation mechanism that constrains high nuclear flux, rather than simple nuclear export or cytoplasmic recycling [71]. Importantly, this interpretation does not require assuming multiple transcriptionally distinct GR species, but instead emerges from fitting population-wide distributions under a minimal transport and degradation scheme. Future studies examining single-cell distributions of GR phosphorylation states (e.g., S211) over time could further resolve the relationship between ligand-induced activation, transcriptional competence, and proteasomal targeting [81, 139].

At the level of transcriptional regulation, our single-cell measurements indicate that GR activation increases the fraction of *DUSP1* alleles engaged in transcription without producing a strong or sustained increase in TS intensity. We systematically tested models in which GR modulates the promoter activation rate k_{on}, the promoter de-activation rate k_{off}, the transcription rate k_{r}, or combinations thereof. Models acting through k_{on} alone or through dual regulation of k_{on} and k_{off} provided comparably strong fits; however, the dual regulation models predicted increases in TS intensity that were not observed in the data, favoring the simpler k_{on}-only mechanism. General activation models including modulation of k_{r} did not improve fits or predictions. Within a two-state bursting framework, this pattern is most consistent with an effective increase in promoter activation frequency, rather than a large change in transcriptional output per active allele [92, 102]. Together with prior work using MMTV reporter constructs [55, 67, 86, 132], which found that GR primarily increases burst frequency, this pattern strongly supports a dominant effect of GR on the effective activation rate k_{on}. Chromatin studies at the endogenous *DUSP1* locus further show GR-dependent recruitment of p300, increases in histone H3/H4 acetylation, and localized chromatin remodeling at the *DUSP1* GRE, features that are naturally associated with both facilitating promoter activation and stabilizing the active chromatin state [134]. While additional mechanisms such as stabilization of the active promoter state cannot be excluded, particularly given chromatin

remodeling at the *DUSP1* locus, these effects are not uniquely identifiable from our current fixed-cell transcription site intensity measurements alone. Accordingly, our model represents GR action through dual regulation of the promoter, in which a GR-dependent increase in the effective activation rate k_{on} dominates over a smaller effect on the de-activation rate k_{off}, capturing the dominant but not exclusive contribution of GR to transcriptional control.

Beyond transcription initiation, the results of our semi-mechanistic models highlight cytoplasmic mRNA decay as a key mechanism in the Dex-GR-*DUSP1* expression dynamics. Our models required a saturable, time-dependent ARE-mediated degradation process to capture *DUSP1* cytoplasmic mRNA dynamics, particularly the rapid decline following peak expression that could not be reconciled with a fixed degradation rate given the sustained transcriptional activity. This is consistent with Muazzen et al., who showed that Dex treatment reduces *DUSP1* mRNA half-life even as steady-state levels rise, and more broadly that GCs universally destabilize ARE-containing mRNAs [37]. The heterogeneity of this response has consequential implications: comparative transcriptomic analyses between Dex treatment and SARS-CoV-2 infection revealed that ARE-mRNAs tend to regulate in opposite directions [37, 110], suggesting that ARE-dependent post-transcriptional control is a clinically relevant factor in GC efficacy during COVID-19 [43].

To further our understanding of the observed cytoplasmic mRNA decline, we extended from a semi-mechanistic to a fully mechanistic model that explicitly incorporates Dex-induced *TTP* gene activation via nuclear GR, *TTP* mRNA production and nuclear export, TTP protein translation, and reversible binding of TTP to ARE-containing mRNAs including *DUSP1* and *TTP* itself (Supplementary Fig. S11). This model achieved comparably strong fits and improved predictions of our experimental data (Supplementary Fig. S12, Table S6), offering an interpretable explanation for the faster clearance of cytoplasmic relative to nuclear *DUSP1* mRNA. In this framework, we have assumed that Dex-induced TTP is unphosphorylated and therefore active, since Dex does not activate p38 but instead induces *DUSP1*/MKP-1, which suppresses p38 activity and maintains TTP in its decay-promoting state [37, 106, 136]. Thus, ligand-induced *DUSP1* expression is shaped not

only by transcriptional activation but also by an actively regulated mRNA clearance circuit that is itself a product of GR signaling.

Several limitations frame the scope of our conclusions. All measurements were obtained using ICC and smiFISH measurements that allowed us to obtain endogenous expression measurements without perturbing the cells' genetic or biochemical processes, but the reliance on fixed cells restricts direct observation of temporal correlations within individual cells and limits identifiability of closely related regulatory mechanisms. In addition, GR localization and *DUSP1* transcription were quantified in separate experiments, such that nuclear GR abundance and *DUSP1* mRNA levels were not measured simultaneously within the same cells. As a result, the coupling between GR transport and transcriptional output is inferred statistically across matched populations rather than directly observed at the single-cell level. Importantly, *TTP* mRNA and protein levels have not been measured directly in this study; TTP dynamics were inferred through model fitting and are consistent with established biochemistry [35, 37, 105] but remain to be validated experimentally in this system. Future work should directly quantify *TTP* expression, TTP phosphorylation status, p38 activity, and MKP-1 protein levels to confirm the proposed regulatory circuit and further constrain model parameters. Our analysis further focuses on a single endogenous target gene in a single epithelial cell line, and regulatory architectures may differ across GR targets or cell types. Nevertheless, the experimental and computational framework developed here is readily extensible to additional genes, perturbations, and signaling contexts. More broadly, this work demonstrates how integrating endogenous single-cell measurements with stochastic modeling can yield predictive, mechanistic insight into hormone-driven gene regulation, providing a foundation for future studies that seek to rationally modulate inflammatory signaling through model-guided perturbations.

2.4 Experimental framework, methods, and quantification

This section is organized in two parts. The first describes sample preparation and imaging, covering cell culture, drug stimulation, the two fixed-cell assays (immunocytochemistry for GR protein and smiFISH for *DUSP1* mRNA), and confocal acquisition. The remaining parts describe

the image-analysis pipelines that convert raw fluorescence into the per-cell measurements of GR localization and *DUSP1* transcript abundance used as inputs to the stochastic models in Section 2.5.

Cell culture

HeLa Kyoto cells (a gift from the DeLuca Lab) were maintained in Dulbecco's modified Eagle medium (DMEM, Thermo Fisher Scientific, 11960-044) supplemented with 10% fetal bovine serum (FBS, Atlas Biologicals, F-0050-A), 10 U/mL penicillin/streptomycin (P/S, Thermo Fisher Scientific, 15140122), 1 mM L-glutamine (L-glut, Thermo Fisher Scientific, 25030081) in a humidified incubator at $37\,^{\circ}\mathrm{C}$ with 5% CO_2.

For smiFISH and ICC experiments, HeLa Kyoto cells were seeded on 18 mm cover glasses in a 12-well plate at approximately 1.5×10^5 cells per well, in DMEM supplemented with 10% charcoal stripped fetal bovine serum (csFBS, Sigma, F6765-500ML), 10 U/mL penicillin/streptomycin, and 1 mM L-glutamine 24 hours prior to the experiment.

Drug stimulation

Dexamethasone (Dex, Sigma, D2915) was reconstituted in nuclease free water to a stock concentration of 67.3×10^3 nM. For experimentation, dilutions were performed such that a volume of $1.6\,\mu\mathrm{L}$ in $1000\,\mu\mathrm{L}$ had the desired concentration. All samples were incubated at $37\,^{\circ}\mathrm{C}$ with 5% CO_2 during the experiment and were only temporarily removed for the addition and mixing of the stimulant(s) (approx. 1.5 min).

For transcription inhibition, cells were first stimulated with 100 nM Dex as above. Following Dex stimulation, 5 mM of triptolide (TPL, Sigma, 645900) was added to the corresponding wells at appropriate times. All samples were incubated at $37\,^{\circ}\mathrm{C}$ with 5% CO_2 during the experiment and were only temporarily removed for the addition and mixing of the stimulant(s) (approx. 1.5 min).

Immunocytochemistry

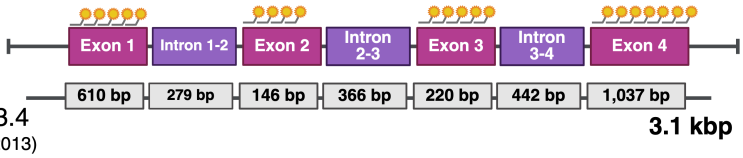
Immunocytochemistry was performed using a modified protocol described here: Abcam ICC protocol.

Briefly, the samples were rinsed twice with RNase-free 1× PBS and then fixed with 4% PFA at room temperature for 10 min. Samples were permeabilized with 0.1% Triton-X100 in PBS for 20 min and washed with 1 mL of PBS three times for ten minutes each wash. Next, samples were blocked for nonspecific binding with 10% Normal Goat Serum (ThermoFisher, 50062Z) for 1 hr at 20 °C. Samples were then incubated overnight in a 1:500 dilution of primary antibody (Abcam, AB183127) containing 1% BSA (ThermoFisher, A14289SA) in PBST (PBS with 0.1% Tween-20, ThermoFisher 85113). The next day the primary antibody solution was aspirated, and the samples were washed with 1 mL of PBS three times for ten minutes each wash. The samples were then incubated with the secondary antibody solution (0.5 µg/mL Goat anti-Rabbit IgG (H+L) Cross-Adsorbed Secondary Antibody, Alexa Fluor 488, Thermo Fisher A11008; 5% Normal Goat Serum; and 50 ng/mL DAPI in PBST) in the dark for 1 hr at 20 °C. Samples were then washed four times: once with 1 mL of PBST for 10 min, and three times with 1 mL of 1× PBS for 10 min each wash. Finally, the samples were mounted on a 15 µL droplet of Vectashield mounting medium (Vector Laboratories, H-1000-10) and sealed with clear nail polish.

Single-molecule inexpensive FISH

Probe design. To design smiFISH probes for *DUSP1* and GAPDH, the gene's sequence was obtained from the Ensembl genome browser by using the transcript ID (DUSP1: ENST00000239223.4, GAPDH: ENST00000229239.10) and exported as a FASTA file. The RepeatMasker Web Server was used to identify any repetitive sequences within the *DUSP1* and GAPDH exonic sequences, and the Oligostan script in R-studio was used to generate potential probes, ensuring at least 21–24 probes for high-quality results. Candidate probes were filtered based on criteria from relevant literature to select those with optimal thermodynamic properties and specificity, avoiding probes that bind non-target regions. Probe specificity was confirmed by blasting sequences against genomic and transcript databases, selecting probes that align perfectly with *DUSP1* and lack significant similarity to other genes. The selected probes were visualized and verified as binding sites using vector mapping software, and the final probe sequences with the FLAP sequences were ordered from IDT (100 µM).

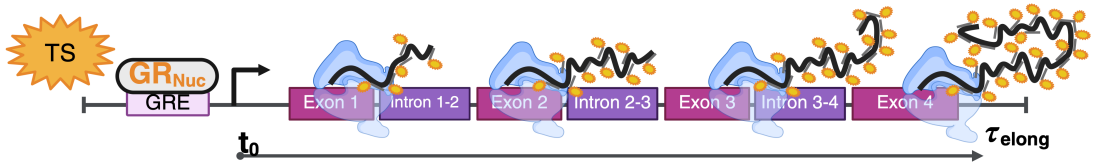
a **Number of probes:** 21
Probe length: 20±5 nt (plus FLAP-Y)
GC content: 45–55%
Melting T (nearest neighbor): 66–70 °C
Reference genome: ENST00000239223.4
Design: Oligostan (Mueller et al., Nat. Methods 2013)



b

Probe Label	Locus	Probe Sequence
DUSP1_P1_Exon1	101 - 127	AGCCGGCGATGTGGCCGGCGTTGAAATTACACTCGGACCTCGTCGACATGCATT
DUSP1_P2_Exon1	132 - 158	CGCACGATGGTGCTGAAGCGCACGTTTTACACTCGGACCTCGTCGACATGCATT
DUSP1_P3_Exon1	189 - 215	CGGAGCTCGGCGTTGGGCACGATGTGTTACACTCGGACCTCGTCGACATGCATT
DUSP1_P4_Exon1	237 - 263	TCGTCCAGCAACACCACGGCGTGGTATTACACTCGGACCTCGTCGACATGCATT
DUSP1_P5_Exon1	347 - 378	TTCGTATCCTCCTTTGAGGAAGAAGACTTGCTTACACTCGGACCTCGTCGACATGCATT
DUSP1_P6_Exon2	380 - 407	CACAGCTCCGGGCAGGAAGCCGAAAACTTACACTCGGACCTCGTCGACATGCATT
DUSP1_P7_Exon2	411 - 437	CTGAGCCCCATGGGGGTCGACTGTTTTTACACTCGGACCTCGTCGACATGCATT
DUSP1_P8_Exon2	452 - 478	CAGATTCCGCGCTGTCAGGGACGCTATTACACTCGGACCTCGTCGACATGCATT
DUSP1_P9_Exon2	490 - 517	CTGATCGTAGAGTGGGGTACTGCTTACACTCGGACCTCGTCGACATGCATT
DUSP1_P10_Exon3	550 - 576	CTTGCGGGAAGCGTGATACGCACTGCTTACACTCGGACCTCGTCGACATGCATT
DUSP1_P11_Exon3	609 - 641	AAATGGTTGGGACAATTGGCTGAGACGTTGATTTACACTCGGACCTCGTCGACATGCATT
DUSP1_P12_Exon3	645 - 674	ACAGGGATGCTCTTGTACTGGTAGTGACCTTACACTCGGACCTCGTCGACATGCATT
DUSP1_P13_Exon3	676 - 702	GCTGATGTCTGCCTTGTGGTTGTCCTTTACACTCGGACCTCGTCGACATGCATT
DUSP1_P14_Exon3	704 - 734	TCTATGAAGTCAATGGCCTCGTTGAACCAGTTACACTCGGACCTCGTCGACATGCATT
DUSP1_P15_Exon4	736 - 762	CACCCTTCCTCCAGCATTCTTGATGGTTACACTCGGACCTCGTCGACATGCATT
DUSP1_P16_Exon4	764 - 790	GGGAAATGCCTGCCTGGCAGTGGACATTACACTCGGACCTCGTCGACATGCATT
DUSP1_P17_Exon4	799 - 831	ATTAGTCCTCATAAGGTAAGCAAGGCAGATGGTTACACTCGGACCTCGTCGACATGCATT
DUSP1_P18_Exon4	833 - 860	AACTCAAAGGCCTCGTCCAGCTTGACTTTACACTCGGACCTCGTCGACATGCATT
DUSP1_P19_Exon4	862 - 888	AGAGATGATGCTTCGCCTCTGCTTCATTACACTCGGACCTCGTCGACATGCATT
DUSP1_P20_Exon4	1046 - 1074	CTGAAGGTAGCTCAGCGCACTGTTCGTGTTACACTCGGACCTCGTCGACATGCATT
DUSP1_P21_Exon4	1076 - 1104	TCAGCAGCTGGGAGAGGTCGTAATGGGGTTACACTCGGACCTCGTCGACATGCATT
FLAP Y-Cy5		Cy5/AA TGC ATG TCG ACG AGG TCC GAG TGT AA/Cy5

c



d

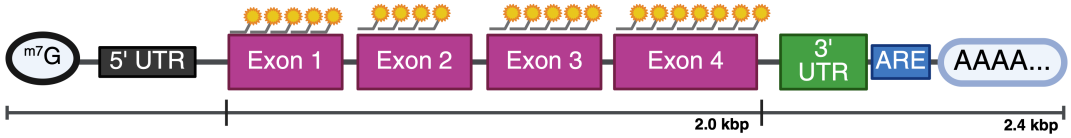


Figure 2.9: Design and targeting scheme for the *DUSP1* smiFISH probe set. (a) Genomic organization of the *DUSP1* locus showing exons and introns with relative length scaling and the distribution of gene-specific smiFISH probes across exonic regions. **(b)** Table listing the smiFISH probe labels, genomic loci, and sequences. Each probe consists of a gene-specific sequence extended with a FLAP-Y overhang for secondary probe binding. **(c)** Cartoon of smiFISH detection at an active transcription site. As RNA polymerase progresses along the gene, nascent *DUSP1* transcripts are labeled by exon-targeting probes, producing a bright nuclear focus. The transcriptional elongation time, τ_{elong}, defines the duration over which polymerases contribute to the TS signal and is used in TS-based model fits and transcriptional inhibition (TPL) predictions. **(d)** Cartoon of probe binding along a mature *DUSP1* mRNA, shown with a relative length scale. Probes tile the coding exons, resulting in a single fluorescent focus. The transcript includes a 5′ cap, coding exons, the 3′ UTR containing an ARE, and a poly(A) tail.

Sample labeling. smiFISH was performed following a protocol previously described [57,117].

Briefly, samples were rinsed twice with RNase-free $1\times$ PBS and fixed with 4% PFA at room temperature for 10 min. This was followed by permeabilization with 70% ethanol at $4\,^{\circ}\mathrm{C}$ for a minimum of 1 hr. Samples were then washed with Wash A buffer (Biosearch Technologies, SMF-WA1-60) for 5 min. Each coverslip was placed cell-side down on a droplet containing $40\,\mu\mathrm{L}$ of hybridization buffer (Biosearch Technologies, SMF-HB1-10) and $1\,\mu\mathrm{L}$ of each duplexed smiFISH probe set (*DUSP1* probes annealed to FLAP-Y-Cy5 and GAPDH exon probes annealed to FLAP-Y-Cy3), and incubated overnight at $37\,^{\circ}\mathrm{C}$ in a sealed humidified chamber.

The following day, samples were transferred to a new 12-well plate and washed twice in Wash A buffer containing 10% formamide at $37\,^{\circ}\mathrm{C}$ for 30 min, first without additives and then with 50 ng/mL DAPI included. Finally, samples were treated with Wash B buffer (Biosearch Technologies, SMF-WB1-20) at room temperature for 5 min, mounted on a $15\,\mu\mathrm{L}$ droplet of Vectashield mounting medium (Vector Laboratories, H-1000-10), and sealed with clear nail polish.

Microscopy imaging

Fluorescent images were acquired on an Olympus IX81 inverted spinning-disk confocal microscope (CSU22 head with quad dichroic and an additional emission filter wheel to minimize spectral crossover) using a $60\times$/1.42 NA oil-immersion objective. Confocal z-stacks were collected with a step size of $0.5\,\mu\mathrm{m}$, with 27 optical sections acquired per channel.

ICC experiments were imaged using two high-power diode lasers with rapid microsecond switching (405 nm for DAPI, 100 ms exposure; 488 nm for Alexa Fluor 488, 100 ms exposure; Thermo Fisher A11008). smiFISH fields of view were imaged using three high-power diode lasers (405 nm for DAPI, 100 ms; 561 nm for smiFISH of GAPDH exons, 100 ms; and 647 nm for smiFISH of *DUSP1* mRNA, 300 ms). Combined smiFISH/ICC fields of view were imaged using four high-power diode lasers (405 nm for DAPI, 100 ms; 488 nm for Alexa Fluor 488, 100 ms; 561 nm for smiFISH of GAPDH exons, 100 ms; and 647 nm for smiFISH of *DUSP1* mRNA, 300 ms).

The system was equipped with differential interference contrast (DIC) optics, built-in spherical aberration correction for all objectives, and a wide-field xenon light source. Images were acquired

using an EMCCD camera (iXon Ultra 888, Andor) controlled with SlideBook software, yielding images with an effective pixel size of 160 nm. The imaging area was 624×928 pixels.

2.4.1 GR quantification from immunocytochemistry

To obtain accurate and consistent subcellular single-cell GR measurements, raw image stacks were processed through the following steps: illumination correction, pseudo-cytoplasmic mask generation, intensity normalization by imaging date, intensity discretization, and conversion to concentrations using per-cell nuclear-to-cytoplasmic volume ratios. Although images were acquired as z-stacks of shape $[P, T, C, Z, Y, X]$, all subsequent intensity quantification and mask generation were performed on 2D maximum-intensity projections along the Z-axis.

Illumination correction. Illumination correction was performed using a data-driven, background-based approach (Figure 2.10a-c). Image z-stacks were first projected along the Z-axis using the 10th percentile intensity to generate a background estimate per field of view, then aggregated across fields of view via a median projection to produce a single profile per channel (Figure 2.10a). Each profile was smoothed with a Gaussian filter (channel-specific σ) to suppress noise and remove cellular morphology artifacts. A 2D Gaussian was then fit to each smoothed profile using nonlinear least squares to produce a parametric correction map (Figure 2.10c). Each fitted profile was normalized to its maximum value and inverted to form a per-pixel correction factor, which was applied multiplicatively to the original image stack (Figure 2.10b).

Pseudo-cytoplasmic mask from DAPI dilation. In datasets without a cytoplasmic stain, pseudo-cytoplasmic regions were derived from the nuclear (DAPI) mask. Nuclear masks were dilated by 20 pixels, and a watershed algorithm was applied to prevent overlaps between neighboring cells. The resulting cell territories were matched to their corresponding nuclei, and the pseudo-cytoplasmic mask for each cell was defined as the difference between the dilated territory and the nuclear mask. Mean intensity within this pseudo-cytoplasmic ring was calculated for each cell, providing non-overlapping cytoplasmic measurements. Cells touching the image border were excluded from analysis.

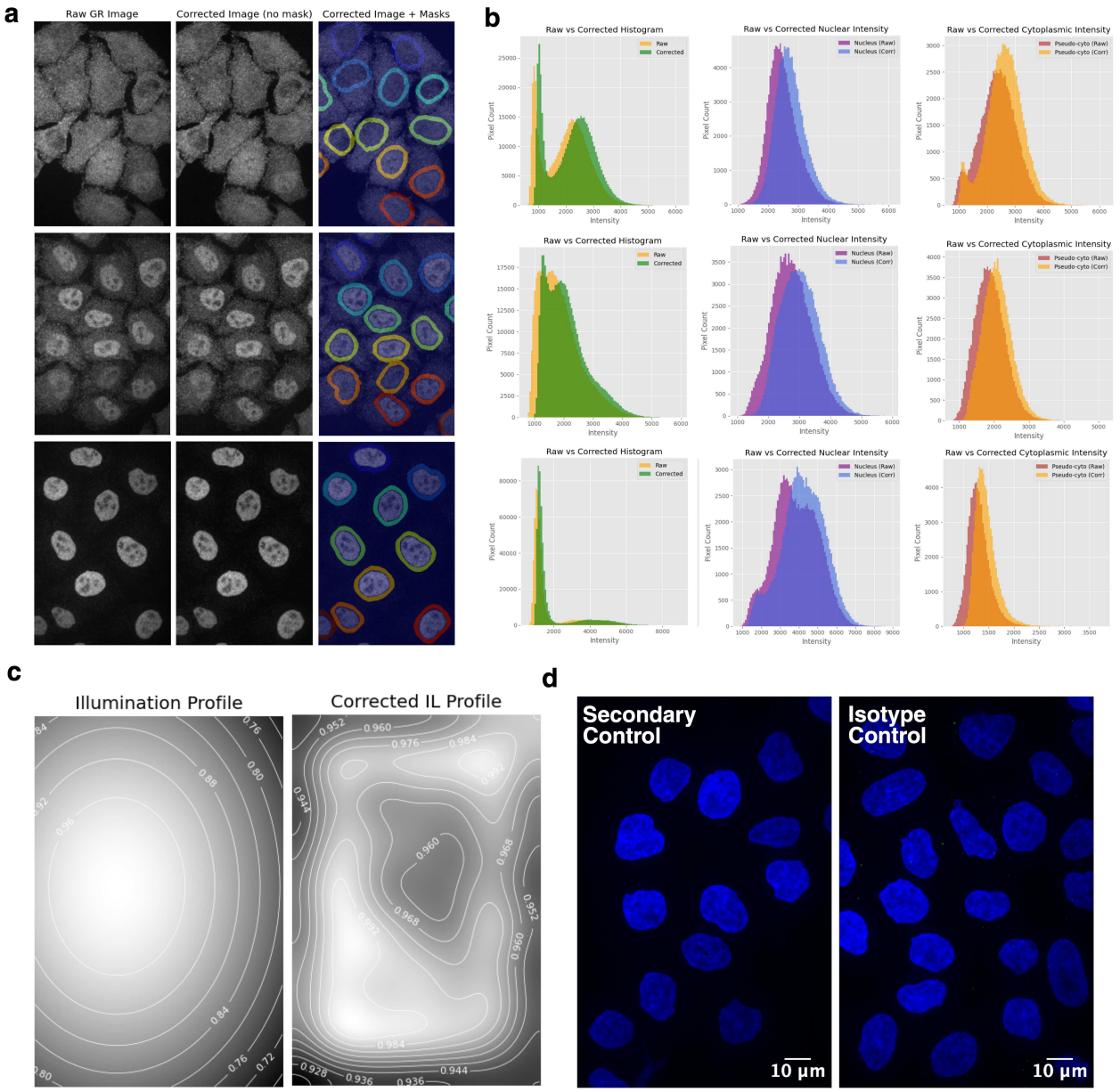


Figure 2.10: Data-driven illumination correction and controls for GR images. **(a)** From left to right, raw GR images, illumination-corrected GR images, and corrected images with pseudo-cytoplasmic masks overlaid for three representative fields of view spanning low to high Dex stimulation from top to bottom. **(b)** Pixel-intensity histograms corresponding to the fields of view in (a). From left to right, distributions of whole-image intensities (raw, yellow; corrected, green), nuclear GR intensities (raw, purple; corrected, blue), and pseudo-cytoplasmic GR intensities (raw, red; corrected, orange), showing improved uniformity after correction. **(c)** Batch-derived illumination profile for the GR channel (left) and the corresponding profile after correction (right), both normalized to the range 0–1 and displayed as contour maps, demonstrating removal of the illumination gradient. **(d)** Representative secondary-only and isotype control images of HeLa cells stained with DAPI, confirming minimal background signal in the GR channel. Scale bars, 10 µm.

Intensity normalization and cell size gating. Raw GR nuclear (`nucGRint`) and cytoplasmic (`cytGRint`) intensities were normalized for between-day imaging variability by a replica-scaling procedure, yielding illumination- and day-corrected intensities (`NucGRCorrected`, `CytGRCorrected`). Additionally, to reduce variability due to cell size, both GR and *DUSP1* datasets were gated to include only cells with nuclear areas between the 25th and 75th percentiles of their respective nuclear area distributions.

Conversion to sub-cellular concentrations. Mean fluorescent intensities within the nuclear and pseudo-cytoplasmic masks, `NucGRCorrected`, `CytGRCorrected`, were assumed to be proportional to the compartmental GR concentrations in arbitrary units of concentration, AUC. To determine GR levels in consistent units of mass, a nuclear-to-cytoplasmic ratio (NCR) was computed as the mean nuclear area divided by the mean cytoplasmic area in the gated *DUSP1* dataset. Arbitrary units of mass (AUM) in the nucleus was estimated as the `NucGRCorrected` intensity rescaled by the NCR, and the `CytGRCorrected` intensity was used directly as a measurement of mass in the cytoplasm. For comparison to the discrete-valued GR transport model, the resulting quantities of mass were discretized into 30 uniformly-spaced bins spanning the 1st to 99th percentile range of the `CytGRCorrected` intensity. Bins were unbounded above to avoid clipping high-expressing cells, and the same bins were used for both nucleus and cytoplasm. The resulting `normGRnuc` and `normGRcyt` represent sub-cellular GR concentrations in arbitrary units of mass (AUM).

2.4.2 *DUSP1* mRNA quantification from smiFISH

Single-cell *DUSP1* transcript counts were extracted from the smiFISH images using a custom pipeline built around BigFISH [118], comprising format conversion, cell segmentation, spot detection and thresholding, SNR-based filtering, and per-cell aggregation. All image processing codes for smiFISH mRNA quantification can be found at https://github.com/MunskyGroup/AngelFISH.

Data conversion. Raw microscopy image stacks and segmentation masks were converted into a standardized HDF5 format for downstream processing. For each experimental folder, multi-

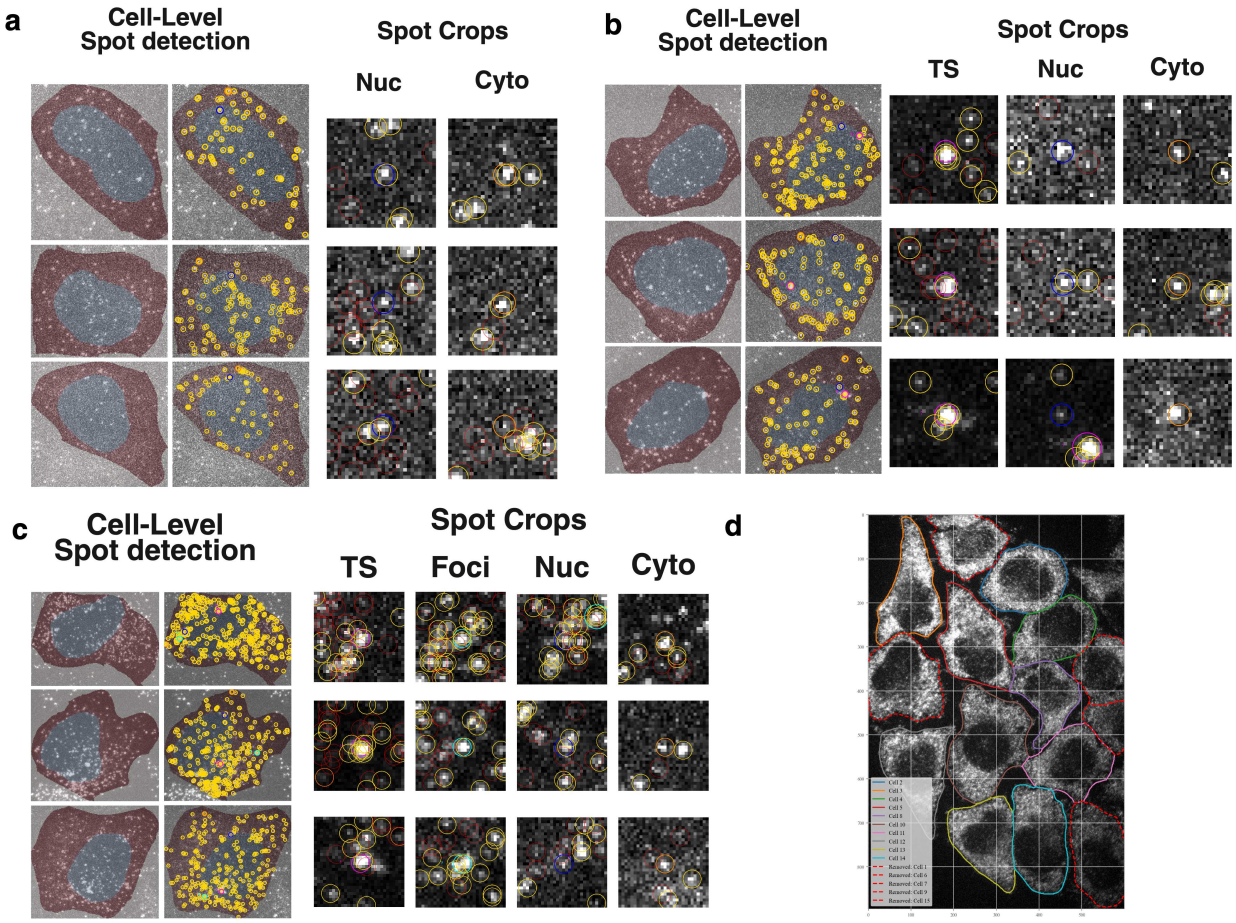


Figure 2.11: Segmentation and smFISH spot detection for single-cell *DUSP1* quantification. Representative *DUSP1* smiFISH images across selected times and Dex concentrations, shown with DAPI and 10 µm scale bars. These images illustrate the range of transcriptional responses used for single-cell quantification. **(a)** Cell-level spot detection in cells without transcription sites or foci. For each example, both nuclear and cytoplasmic CellPose masks are displayed over the smiFISH image, with detected *DUSP1* mRNA spots shown in gold. The accompanying spot crops show nuclear and cytoplasmic detections, with red circles marking low-SNR candidates removed during filtering. **(b)** Cell-level spot detection in cells containing transcription sites. Nuclear and cytoplasmic masks are displayed together with the detected *DUSP1* spots, including transcription-site detections. Spot crops illustrate transcription sites, nuclear mRNA spots, and cytoplasmic mRNA spots used for downstream quantification. **(c)** Cell-level spot detection in cells containing both transcription sites and cytoplasmic foci. Nuclear and cytoplasmic masks are shown alongside the full set of detected spots. Spot crops include transcription sites, cytoplasmic foci, nuclear mRNA spots, and cytoplasmic mRNA spots, with removed low-SNR candidates indicated in red. **(d)** Representative field of view with *GAPDH*-based cytoplasmic segmentation and removal of border-touching or partial cells. Each color denotes a unique cell used for downstream analysis.

Table 2.1: Per-cell variability of GR fluorescence by Dex concentration and stimulation time. Mean intensities are reported in arbitrary units after background correction. CV is the coefficient of variation across single cells, pooled across biological replicas. n is the number of cells per condition.

Dex	Time		Nuclear GR		Cytoplasmic GR		N/C ratio	
(nM)	(min)	n	mean	CV (%)	mean	CV (%)	mean	CV (%)
0	0	430	2979	14.6	2858	16.5	1.05	11.2
1	10	326	2977	17.1	2783	17.0	1.08	11.8
1	30	308	3116	16.8	2670	18.6	1.18	13.0
1	50	350	3090	17.0	2500	17.8	1.25	12.4
1	75	323	3031	15.5	2278	15.1	1.34	12.2
1	120	338	3223	16.1	2168	15.1	1.50	12.9
1	180	301	3517	16.6	2059	17.1	1.72	11.0
10	10	300	3000	16.6	2012	13.0	1.50	13.3
10	30	282	4149	18.1	1730	10.6	2.40	16.2
10	50	279	4372	16.7	1515	9.2	2.90	16.3
10	75	270	4506	18.6	1376	8.0	3.26	13.3
10	120	320	4538	12.9	1402	12.0	3.26	12.7
10	180	317	4115	14.7	1305	18.9	3.21	15.3
100	10	319	4247	15.5	1370	12.4	3.12	12.9
100	30	309	4816	15.6	1367	14.0	3.53	10.8
100	50	311	5463	16.3	1567	12.2	3.50	14.8
100	75	277	4459	17.3	1407	12.3	3.17	11.1
100	120	314	4266	13.7	1450	9.3	2.96	15.4
100	180	298	4106	13.2	1409	8.0	2.92	11.7

channel 3D TIFF images and associated log files were parsed to identify fields of view, time points, and channels. Masks for nuclei and cytoplasm, if precomputed, were unpacked and aligned to their respective channels. All image data were stored as `float32` Dask arrays, rechunked for efficient processing, and saved to disk along with acquisition metadata in JSON format embedded within the HDF5 file.

Cellpose segmentation. Segmentation of nuclei and cell boundaries was performed using the Cellpose deep learning framework, with custom pretrained models for nuclear DAPI and cytoplasmic smiFISH GAPDH-Cy3 channels [140]. Nuclear masks were generated from the DAPI channel, while cytoplasmic masks were segmented from the corresponding GAPDH smiFISH channel (Figure 2.3a). Model parameters (diameter, flow threshold, probability threshold, and minimum

object size) were optimized for each sub-cellular compartment. Segmentation results were post-processed to ensure one-to-one alignment between nuclear and cytoplasmic masks (Figure 2.11d).

Spot detection and BigFISH thresholding. Initial RNA spot detection was performed using BigFISH [118], operating on the *DUSP1*-Cy5 smiFISH channel. Detected coordinates were annotated with per-spot properties including voxel-based size, signal intensity, and a computed signal-to-noise ratio (SNR) using the `compute_snr_spots` function. For each field of view, spot coordinates were mapped to individual cells and classified as nuclear or cytoplasmic using segmentation masks. Clusters corresponding to transcription sites or large cytoplasmic foci were identified and later included in single-molecule counts. For each smiFISH channel, an empirical detection threshold was selected by analyzing a random subset of up to 50 images. Spot intensity distributions were used to compute descriptive statistics (minimum, maximum, median, mean, and quartiles), from which a per-dataset threshold was chosen. In most datasets, the mean threshold value was applied; for specific noisier datasets, fixed percentile values (25th, 75th, or 90th) were used instead to improve robustness.

SNR-based spot filtering. Spot quality control was based on two complementary criteria: an absolute SNR cutoff requiring SNR $\geq$ `abs_threshold`, and a compartment-specific SNR

$$\mathrm{MG_SNR} = \frac{\mathrm{signal} - \mu_{\mathrm{compartment}}}{\sigma_{\mathrm{compartment}}}, \tag{2.1}$$

where $\mu_{\mathrm{compartment}}$ and $\sigma_{\mathrm{compartment}}$ are the mean and standard deviation of intensity within the nuclear or cytoplasmic mask of the same cell. All analyses used the `mg_abs` method (`mg_threshold` $= 3$, `abs_threshold` $= 6$): a spot was retained if it passed the MG SNR threshold (`MG_pass`) or, for spots with $1 \leq \mathrm{MG_SNR} \leq$ `mg_threshold`, if its absolute SNR exceeded `abs_threshold`. This fallback prevents rejection of real spots in cells with highly variable background. Spots failing both criteria were excluded from downstream quantification and recorded separately for quality review.

Cell-level quantification. Raw spot, cluster, and cell-property data were loaded and concatenated across all imaging slides for each experimental replicate using a combined dataset manager,

with per-spot SNR metrics computed via `SNRAnalysis` and annotated with an absolute SNR flag and a compartment-specific MG SNR value (Equation 2.1). Cells touching image borders were excluded at the filtering stage. To ensure consistent cell identity across replicates, unique cell, spot, and cluster identifiers were offset by a replicate-specific numeric prefix prior to concatenation.

Using the filtered spot list, the `DUSP1Measurement` pipeline aggregated single-molecule counts to the cell level across two quality filters: `absolute` (SNR $\geq$ `abs_threshold`) and `MG_SNR` (compartment-specific SNR $\geq$ `mg_threshold`). Each filter yielded total, nuclear, and cytoplasmic spot counts per cell.

TS and cytoplasmic foci were identified from nuclear and cytoplasmic clusters, respectively, subject to a minimum cluster size of four spots. Clusters falling below this threshold were excluded from TS and foci counts but tracked via diagnostic fields (`n_ts_lt_min`, `n_foci_lt_min`). For valid TS, the largest and second-largest cluster sizes were also recorded (`largest_ts`, `second_largest_ts`).

Additional per-cell metrics included nuclear and cytoplasmic area; mean and standard deviation of nuclear, cytoplasmic, and whole-cell intensities; and experimental metadata (time, Dex concentration, replicate, FOV). This pipeline was applied identically to all *DUSP1* experimental replicates. Cell-level results were saved alongside the filtered spot, cluster, and cell property tables for downstream analysis.

2.5 Computational modeling and alternative model discrimination

We used the Stochastic System Identification Toolkit (SSIT) (`https://github.com/MunskyGroup/SSIT/` [126]) to define, solve, and fit the GR-mediated *DUSP1* transcription (Dex-GR-*DUSP1*) model. Scripts to reproduce all analyses are found at [`https://github.com/MunskyGroup/Ron_et_al_2026`], and are briefly described below.

2.5.1 Modeling framework and inference

All models in this chapter are continuous-time Markov processes governed by the CME 1.5.1, in which the system state is the vector of integer molecule counts and each reaction j is specified by a propensity w_j and a stoichiometry vector $\boldsymbol{s}_j$ giving the net change in counts when reaction j fires. The full model comprises six species: inactive gene copies (`offGene`), active gene copies (`onGene`), cytoplasmic GR (`cytGR`), nuclear GR (`nucGR`), nuclear *DUSP1* mRNA (`rNuc`), and cytoplasmic *DUSP1* mRNA (`rCyt`); the mechanistic TTP extension (Section 2.5.6) adds further species. Reactions are numbered consistently with the graphical abstract (Figure 2.1b) and the mechanistic schematic (Figure 2.15): reactions 1–5 govern cytoplasmic GR production and degradation and GR nucleocytoplasmic transport and nuclear degradation; reactions 6–10 govern *DUSP1* promoter switching, transcription, nuclear export, and cytoplasmic decay; and reactions 11–18 extend the model to resolve TTP. The module-specific reactions and propensities are given in Sections 2.5.3 through 2.5.6.

Time-varying input signals

Three deterministic signals enter the propensities. They are evaluated at the current time t (in minutes), with $t = 0$ the moment of dexamethasone addition. The dexamethasone signal driving nuclear import is

$$I_{\mathrm{Dex}}(t) = D_0\, e^{-\gamma_{\mathrm{Dex}}\,(t-\tau_{\mathrm{elong}})}, \tag{2.2}$$

the phenomenological TTP activity is

$$I_{\mathrm{TTP}}(t) = \begin{cases} 1 & t \le 0, \\ 1 + TTP_1\,\dfrac{t^{\eta}}{t^{\eta} + t_{\mathrm{TTP}}^{\eta}} & t > 0, \end{cases} \tag{2.3}$$

and the triptolide transcriptional shut-off is

$$I_{\mathrm{TPL}}(t) = \begin{cases} 1 & t \leq \tau_{\mathrm{elong}} + t_{\mathrm{TPL}}, \\ e^{-k_{\mathrm{TPL}}\,(t-\tau_{\mathrm{elong}}-t_{\mathrm{TPL}})} & t > \tau_{\mathrm{elong}} + t_{\mathrm{TPL}}. \end{cases} \tag{2.4}$$

In the GR-only models $\tau_{\mathrm{elong}} = 0$. In the absence of triptolide $t_{\mathrm{TPL}} \to \infty$, so that $I_{\mathrm{TPL}} \equiv 1$.

CME solutions

Solutions to the time-varying CME were obtained using Finite State Projection (FSP) [123] and the Stochastic Simulation Algorithm (SSA) [141], implemented in the SSIT [126]. The GR model (nuclear and cytoplasmic GR) was solved directly by FSP. For comparison to nascent and nuclear *DUSP1* mRNA distributions, an approximate hybrid analysis was used in which `cytGR` and `nucGR` were propagated as deterministic ODEs that fed into an FSP solution for the gene states and mRNA. All ODE and FSP analyses assumed probability distributions corresponding to steady state under $\mathrm{Dex} = 0\,\mathrm{nM}$ at $t = 0$. SSA analyses were initialized at the steady-state ODE mean at $t = -500\,\mathrm{min}$ and evolved to approximate steady state at $t = 0$. The hybrid ODE-FSP approximation was verified against SSA simulations for nuclear mRNA (median KS-test $p = 0.07$ over 1000 simulations), with small deviations at the right tail as expected from the deterministic treatment of the GR signal.

Likelihood and Bayesian inference

After solving the CME by FSP or hybrid ODE-FSP, the resulting probability distributions were used to estimate parameters by likelihood maximization and sampling of their Bayesian posterior distributions. For a model M with parameter vector θ, the solution gives the probability $P_M(\mathbf{x} \mid t, \theta)$ of each discrete molecular state $\mathbf{x}$ at time t. Experimental observations were compared to the corresponding model-predicted distributions for the measured species. For cells indexed by c and time points indexed by t_j, the likelihood of the data $\mathcal{D} \equiv \{d_{c,j}\}$ was computed as the product of

the model probabilities assigned to the observed counts,

$$L_{\mathcal{D}}(\theta; M) = \prod_j \prod_c P_M \left(X = d_{c,j} \mid t_j, \theta\right), \tag{2.5}$$

or equivalently as the summed log-likelihood,

$$\log L_{\mathcal{D}}(\theta; M) = \sum_j \sum_c \log P_M \left(X = d_{c,j} \mid t_j, \theta\right). \tag{2.6}$$

When multiple measured quantities were linked to model species, such as nuclear mRNA counts or GR localization, the relevant marginal distribution was extracted from the full CME solution before evaluating the likelihood. Independent Gaussian priors were placed on the $\log_{10}$-transformed parameters, giving the log-posterior

$$\log P(\theta \mid \mathcal{D}, M) = \log L_{\mathcal{D}}(\theta; M) + \log P(\theta). \tag{2.7}$$

For the full model in the final estimation phase, direct likelihood maximization using the FSP is intractable, and we instead combine SSA trajectories for `rCyt` and `rNuc` with FSP analysis of nascent RNA and minimize the loss

$$\begin{aligned} \mathrm{Loss}(\theta; M) = &\alpha_1 \left(\sum_j n_c(t_j) \left| \mathrm{CDF}_M(t_j, \theta) - \mathrm{CDF}_{\mathcal{D}}(t_j) \right|_1 \right)_{\mathrm{Nuc}} \\ &+ \left(\sum_j n_c(t_j) \left| \mathrm{CDF}_M(t_j, \theta) - \mathrm{CDF}_{\mathcal{D}}(t_j) \right|_1 \right)_{\mathrm{Cyt}} \\ &+ \left(\alpha_2 \log L_{\mathcal{D}}(\theta; M)\right)_{\mathrm{TS}} + \log P(\theta), \end{aligned} \tag{2.8}$$

where $\mathrm{CDF}_M(t_j, \theta)$ and $\mathrm{CDF}_{\mathcal{D}}(t_j)$ are the cumulative distribution functions of the model and data at time t_j, and $n_c(t_j)$ is the number of cells measured at each time. To allow the nuclear, cytoplasmic, and transcription-site terms to be combined on a common scale, the heuristic factors

α_1 and α_2 were chosen so that the variance of each term over 100 simulated datasets was equal to one: α_1 from the nuclear mRNA term, and α_2.

Fit-and-predict pipeline

Parameters were estimated in stages, each conditioned on the parameters fixed in the previous stage:

1. **GR model selection and fit.** The eight GR transport, synthesis, and degradation parameters were identified by full FSP-based maximum a posteriori (MAP) estimation (Equation 2.7) against single-cell ICC data at 1, 10, and 100 nM Dex.
2. ***DUSP1* nuclear and transcription-site fit.** Using the fixed GR parameters, the nine promoter-switching, transcription, and nuclear-export parameters were estimated by hybrid ODE (GR) and FSP (nascent and nuclear *DUSP1*) MAP estimation from measurements at 100 nM Dex.
3. ***DUSP1* cytoplasmic fit.** Holding the GR parameters fixed, all remaining parameters were expanded and updated using 10,000 SSA trajectories per parameter set for approximate Bayesian computation on the marginal distributions of nascent, nuclear, and cytoplasmic *DUSP1* mRNA at 100 nM Dex, with Metropolis-Hastings sampling of the combined objective (Equation 2.8).
4. **TPL fit and final selection.** The transcriptional inhibition rate k_{TPL} was estimated from the nuclear mRNA distributions following TPL application, and the final *DUSP1* model was selected.
5. **Predictive validation.** The fully parameterized model was tested by predicting held-out Dex concentrations and TPL timings without refitting.

2.5.2 Parameter glossary

Each parameter is listed with its symbol, description (units), and the corresponding reaction in the mechanistic-model schematic (Figure 2.15).

Glucocorticoid receptor (GR).

k_g GR (cytoplasmic) synthesis rate (min^{-1}) — reaction 1

γ_{GRcyt} cytoplasmic GR degradation rate (min^{-1}) — reaction 2

k_{cn0} basal cyto→nuc import rate (min^{-1}) — reaction 3

k_{cn1} Dex-dependent import rate (min^{-1}) — reaction 3

M_{Dex} half-saturation of Dex import (nM) — reaction 3

k_{nc} GR nuclear export rate (min^{-1}) — reaction 4

γ_{GRnuc} nuclear GR degradation rate (min^{-1}) — reaction 5

D_0 Dex dose / input amplitude (nM) — input $I_{\text{Dex}}(t)$

γ_{Dex} Dex signal decay rate (min^{-1}) — input $I_{\text{Dex}}(t)$

k_{nc1} Dex modulation of export (min^{-1}) — GR Dex-export model only

***DUSP1* transcription.**

$k_{on,0}$ basal gene activation rate (min^{-1}) — reaction 6

$k_{on,1}$ nucGR-dependent activation rate (min^{-1}) — reaction 6

k_{off} basal gene inactivation rate (min^{-1}) — reaction 7

m_{koff} nucGR modulation of inactivation (molecules^{-1}) — reaction 7

$k_{r,off}$ leak / off-state transcription rate (min^{-1}) — reaction 8

$k_{r,on,0}$ basal on-state transcription rate (min^{-1}) — reaction 8

$k_{r,on,1}$ nucGR-dependent transcription rate (min^{-1}) — reaction 8

Cytoplasmic *DUSP1* mRNA.

$k_{Nuc2Cyt}$ *DUSP1* mRNA nuclear export rate (min^{-1}) — reaction 9

$k_{degCyt,0}$ basal cytoplasmic degradation rate (min^{-1}) — reaction 10a

$k_{degCyt,1}$ TTP-bound (enhanced) degradation rate (min^{-1}) — reaction 10c

k_{DTTP} TTP–mRNA binding saturation (molecules) — semi-mechanistic I_{TTP} model

TTP_1 max fold-change in TTP activity (unitless) — input $I_{\text{TTP}}(t)$

t_{TTP} half-max time for TTP activity (min) — input $I_{\text{TTP}}(t)$

η Hill coefficient, TTP time-dependence (unitless) — input $I_{\mathrm{TTP}}(t)$

Mechanistic TTP module (extended model).

$k_{on,1}^{\mathrm{TTP}}$ nucGR-dependent TTP-gene activation (min^{-1}) — reaction 11

k_{off}^{TTP} TTP-gene inactivation (min^{-1}) — reaction 12

$k_{r,on}^{\mathrm{TTP}}$ TTP transcription rate (min^{-1}) — reaction 13

$k_{Nuc2Cyt}^{\mathrm{TTP}}$ TTP mRNA nuclear export (min^{-1}) — reaction 14

k_{tl} TTP translation rate (min^{-1}) — reaction 15

γ_p TTP protein degradation (min^{-1}) — reaction 18

k_b TTP protein–mRNA binding rate (min^{-1}) — reactions 10b, 16

k_u TTP protein–mRNA unbinding rate (min^{-1}) — reactions $10\mathrm{b}^{-1}$, 16^{-1}

η_{TTP} Hill coefficient, TTP–mRNA binding (unitless) — reactions 10b, 16

γ_0^{TTP} basal TTP mRNA degradation (min^{-1}) — reaction 17

2.5.3 GR transport and model discrimination

GR model. The GR module tracks two species, cytoplasmic GR (`cytGR`) and nuclear GR (`nucGR`), with initial condition $(\texttt{cytGR}, \texttt{nucGR}) = (24, 1)$. GR transport and turnover are described by five reactions, numbered as in Figure 2.1b: cytoplasmic GR production (reaction 1), cytoplasmic GR degradation (reaction 2), import from cytoplasm to nucleus (reaction 3), export from nucleus to cytoplasm (reaction 4), and nuclear GR degradation (reaction 5). The dexamethasone input $I_{\mathrm{Dex}}(t)$ (Equation 2.2) drives transport through Michaelis-Menten kinetics, so that Dex-induced import (or, in the export model, export inhibition) saturates at high concentrations. The selected "Nuc + Cyt Deg" model, in which Dex drives import and GR is degraded in both

compartments (Figure 2.2b), contains all five reactions:

$$(1)\quad \varnothing \to GR_{\mathrm{cyt}}:\ w_1 = k_g \qquad \text{(cytoplasmic GR production)}$$

$$(2)\quad GR_{\mathrm{cyt}} \to \varnothing:\ w_2 = \gamma_{\mathrm{GRcyt}}\, GR_{\mathrm{cyt}} \qquad \text{(cytoplasmic GR degradation)}$$

$$(3)\quad GR_{\mathrm{cyt}} \to GR_{\mathrm{nuc}}:\ w_3 = \Big(k_{cn0} + (t>0)\, k_{cn1}\, \tfrac{I_{\mathrm{Dex}}(t)}{M_{\mathrm{Dex}}+I_{\mathrm{Dex}}(t)}\Big) GR_{\mathrm{cyt}} \qquad \text{(Dex-induced import)}$$

$$(4)\quad GR_{\mathrm{nuc}} \to GR_{\mathrm{cyt}}:\ w_4 = k_{nc}\, GR_{\mathrm{nuc}} \qquad \text{(nuclear export)}$$

$$(5)\quad GR_{\mathrm{nuc}} \to \varnothing:\ w_5 = \gamma_{\mathrm{GRnuc}}\, GR_{\mathrm{nuc}} \qquad \text{(nuclear GR degradation)}$$

Here $(t>0)$ is a switch equal to 1 for $t>0$ and 0 otherwise, so the Dex-dependent import term is active only after Dex addition.

Candidate models. Four candidate architectures were compared (Figure 2.2b, Figure 2.12). They differ only in where GR is degraded and in whether Dex acts on import or on export:

- **Nuc + Cyt Deg** (selected; Dex import with γ_{GRnuc} and γ_{GRcyt}; 8 parameters): all reactions 1–5.
- **Cyt Deg** (Dex import with γ_{GRcyt}; 7 parameters): set $\gamma_{\mathrm{GRnuc}} = 0$, removing reaction 5.
- **Nuc Deg** (Dex import with γ_{GRnuc}; 7 parameters): set $\gamma_{\mathrm{GRcyt}} = 0$, removing reaction 2.
- **Dex Export** (Dex inhibits export, with γ_{GRnuc} and γ_{GRcyt}; 8 parameters): keep reactions 1, 2, 5 and replace reactions 3–4 below.

In the Dex Export model, Dex inhibits nuclear export rather than enhancing import, and reactions 3–4 become

$$(3)\quad GR_{\mathrm{cyt}} \to GR_{\mathrm{nuc}}:\ w_3 = k_{cn0}\, GR_{\mathrm{cyt}}$$

$$(4)\quad GR_{\mathrm{nuc}} \to GR_{\mathrm{cyt}}:\ w_4 = \max\Big(0,\ k_{nc} - (t>0)\, k_{nc1}\, \tfrac{I_{\mathrm{Dex}}(t)}{M_{\mathrm{Dex}}+I_{\mathrm{Dex}}(t)}\Big) GR_{\mathrm{nuc}}.$$

Model discrimination. Each candidate was fit independently to the single-cell ICC data at 1, 10, and 100 nM Dex by maximum a posteriori estimation, and the four were ranked by log-posterior, AIC, BIC, and an approximate Bayes factor (Table 2.2). Schematics, single-cell distributions, and temporal trajectories for the three rejected variants are shown in Figure 2.12. The

compartment-specific Nuc + Cyt Deg model achieved the highest log-posterior and the lowest BIC and was retained for all subsequent analyses, remaining favored even after penalizing its additional degradation parameter and favored over every alternative by a decisive margin in both BIC and the approximate Bayes factor (Table 2.2). The biological interpretation of this outcome is developed in Section 2.2.2.

Table 2.2: Comparison of alternative GR transport and degradation models. Larger (less negative) log-posterior values indicate better agreement with the single-cell ICC data. ΔLogP, ΔAIC, and ΔBIC are reported relative to the selected Nuc + Cyt Deg (Dex Import) model. Approximate Bayes factors (aBF) are computed from ΔBIC. See also Figure 2.12.

	Import, $\gamma_{\mathrm{nuc}}, \gamma_{\mathrm{cyt}}$	Import, γ_{cyt}	Import, γ_{nuc}	Export, $\gamma_{\mathrm{nuc}}, \gamma_{\mathrm{cyt}}$
Num. parameters	8	7	7	8
$\log(\mathrm{MAP}/\mathrm{MAP}_{\mathrm{best}})$	0	-913	-128	-19194
$\mathrm{AIC} - \mathrm{AIC}_{\mathrm{best}}$	0	1825	253	38388
$\mathrm{BIC} - \mathrm{BIC}_{\mathrm{best}}$	0	1818	246	38388
$\log(\mathrm{aBF}_{\mathrm{BIC}})$	0	-909	-123	-19194

2.5.4 *DUSP1* transcription and model discrimination

Transcription model. The nuclear *DUSP1* module adds three species to the GR model: the inactive and active promoter states, $Gene_{\mathrm{Off}}$ and $Gene_{\mathrm{On}}$, and nuclear *DUSP1* mRNA, $DUSP1_{\mathrm{nuc}}$ (`rNuc`), with initial condition $(Gene_{\mathrm{Off}}, Gene_{\mathrm{On}}, DUSP1_{\mathrm{nuc}}) = (2, 0, 5)$. The two alleles switch between OFF and ON states, transcribe nascent mRNA, and export it to the cytoplasm through reactions 6–9, with nuclear GR entering as the time-varying input $GR_{\mathrm{nuc}}(t)$ taken from the fitted GR model. The full (superset) propensities are

$$(6)\quad Gene_{\mathrm{Off}} \to Gene_{\mathrm{On}} : w_6 = \left(k_{on,0} + k_{on,1}\, GR_{\mathrm{nuc}}\right) Gene_{\mathrm{Off}} \qquad \text{(promoter activation)}$$

$$(7)\quad Gene_{\mathrm{On}} \to Gene_{\mathrm{Off}} : w_7 = \frac{k_{off}}{1 + m_{koff}\, GR_{\mathrm{nuc}}}\, Gene_{\mathrm{On}} \qquad \text{(promoter inactivation)}$$

$$(8)\quad \varnothing \to DUSP1_{\mathrm{nuc}} : w_8 = \left(k_{r,off} + (k_{r,on,0} + k_{r,on,1}\, GR_{\mathrm{nuc}})\, Gene_{\mathrm{On}}\right) I_{\mathrm{TPL}}(t) \qquad \text{(transcription)}$$

$$(9)\quad DUSP1_{\mathrm{nuc}} \to DUSP1_{\mathrm{cyt}} : w_9 = k_{Nuc2Cyt}\, DUSP1_{\mathrm{nuc}} \qquad \text{(nuclear export)}$$

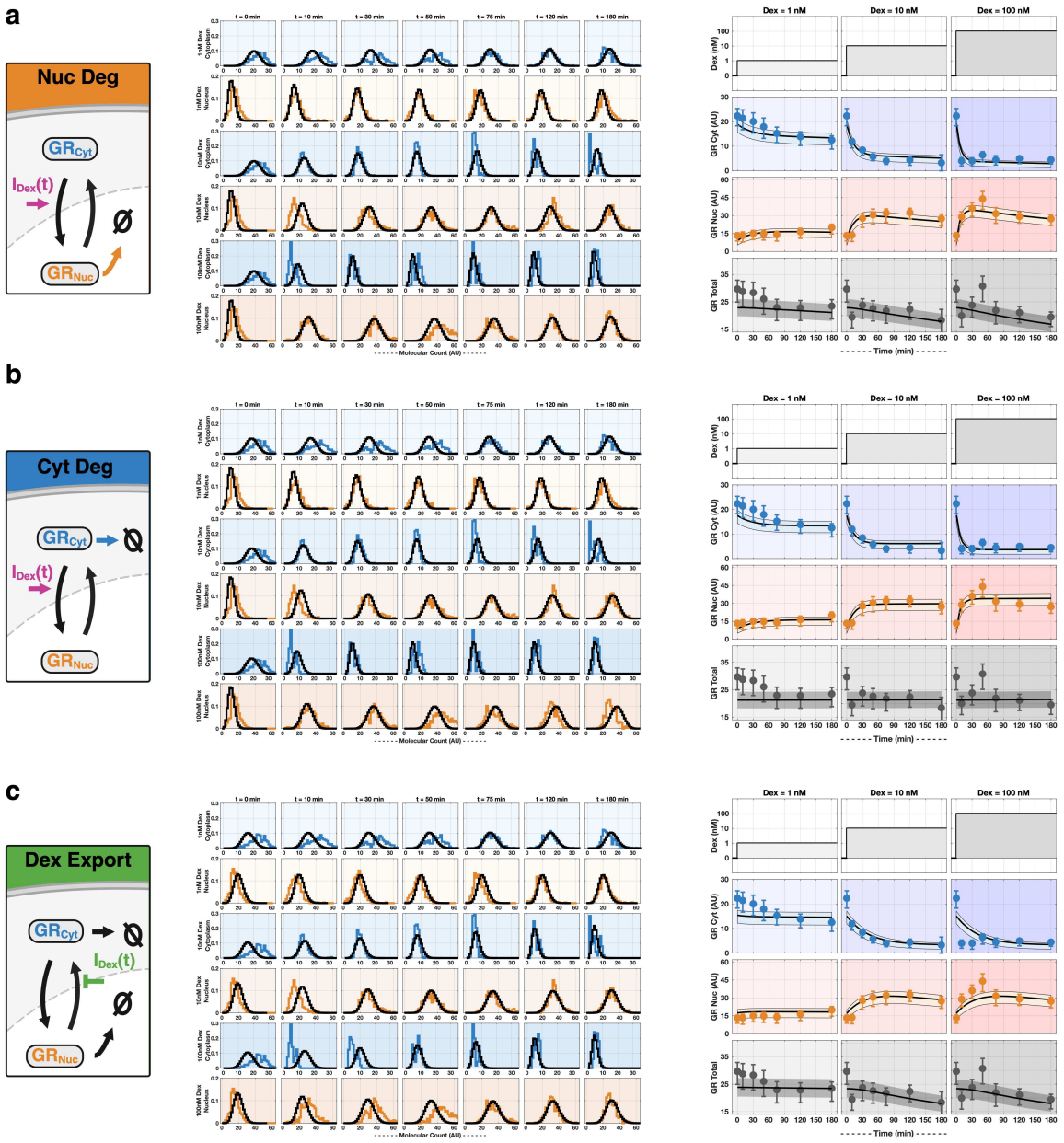


Figure 2.12: GR transport and degradation models evaluated using single-cell ICC data. **(a)** Nuclear degradation (Nuc Deg) model, in which GR is removed from the nuclear compartment. From left to right, the reaction schematic with import driven by $I_{\mathrm{Dex}}(t)$; single-cell distributions of GR molecular count for cytoplasm and nucleus at 1, 10, and 100 nM Dex across time points ($t = 0$, 10, 30, 50, 75, 120, and 180 min), with measured distributions colored and shaded by compartment (cytoplasm, blue; nucleus, orange) and model predictions overlaid as black lines; and temporal trajectories at Dex = 1, 10, and 100 nM showing the imposed $I_{\mathrm{Dex}}(t)$ input, $\mathrm{GR}_{\mathrm{Cyt}}$, $\mathrm{GR}_{\mathrm{Nuc}}$, and total GR. **(b)** Cytoplasmic degradation (Cyt Deg) model, in which $\mathrm{GR}_{\mathrm{Cyt}}$ is degraded, shown with the same panel layout as (a). **(c)** Dex-modulated export (Dex Export) model, in which $I_{\mathrm{Dex}}(t)$ inhibits GR nuclear export with degradation from both compartments, shown with the same panel layout as (a). In all distribution panels, data are colored and shaded by Dex concentration and model fits are black lines. In all trajectory panels, data points and bars denote the median $\pm$ IQR, and black lines with shading denote the model fit and its uncertainty.

Transcription (reaction 8) is gated by the triptolide input $I_{\mathrm{TPL}}(t)$ (Equation 2.4), which equals one in the absence of TPL. Transcriptional elongation was treated as a fixed deterministic delay τ_{elong} following initiation: this delay sets the accumulation time for nascent mRNA at the transcription site and the lag between the GR input and the release of mature mRNA, so that mature mRNA released at time t is controlled by GR_{nuc} at time $t - \tau_{\mathrm{elong}}$. The model assumes two *DUSP1* alleles per cell, consistent with the observation that 98.9% of cells contained zero, one, or two detectable transcription sites. In the nuclear-only fits, reaction 9 is treated as removal from the nuclear pool ($DUSP1_{\mathrm{nuc}} \rightarrow \varnothing$); in the full model it transfers mRNA to the cytoplasmic species (Section 2.5.5).

Candidate models. Nuclear GR can act at three points in this network: promoter activation ($k_{on,1}$), promoter inactivation (m_{koff}), and the on-state transcription rate ($k_{r,on,1}$). Five candidate models (M1–M5; Figure 2.13) retain different subsets of these couplings, holding the others at zero:

- **M1 – Repression:** GR_{nuc} slows promoter inactivation only (m_{koff} free; $k_{on,1} = k_{r,on,1} = 0$).
- **M2 – Activation:** GR_{nuc} accelerates promoter activation only ($k_{on,1}$ free; $m_{koff} = k_{r,on,1} = 0$).
- **M3 – Production:** GR_{nuc} raises the transcription rate only ($k_{r,on,1}$ free; $k_{on,1} = m_{koff} = 0$).
- **M4 – General Activation:** GR_{nuc} accelerates activation, slows inactivation, and raises transcription ($k_{on,1}$, m_{koff}, $k_{r,on,1}$ all free).
- **M5 – Dual Regulation:** GR_{nuc} accelerates activation and slows inactivation ($k_{on,1}$, m_{koff} free; $k_{r,on,1} = 0$), with the basal off-state leak removed ($k_{r,off} = 0$), so reaction 8 reduces to $w_8 = k_{r,on,0}\, Gene_{\mathrm{On}}\, I_{\mathrm{TPL}}(t)$.

Models M1–M4 retain the low basal off-state transcription rate $k_{r,off}$; M5 is a reduction of M4 that removes both $k_{r,off}$ and $k_{r,on,1}$.

Model discrimination. Each model was fit to the 100 nM Dex smiFISH data for nuclear mRNA counts and transcription-site intensity by MAP estimation, and ranked by log-posterior, AIC, BIC, and an approximate Bayes factor (Table 2.3, Figure 2.13). Models in which GR_{nuc} acts through promoter activation ($k_{on,1}$) strongly outperformed the k_{off}-only (M1) and k_r-only (M3)

variants, identifying increased burst frequency as the dominant mechanism. The dual-regulation model M5, in which GR_{nuc} both accelerates promoter activation and slows inactivation, achieved the lowest BIC and was retained for the cytoplasmic and full-model analyses. The biological interpretation is developed in Section 2.2.4.

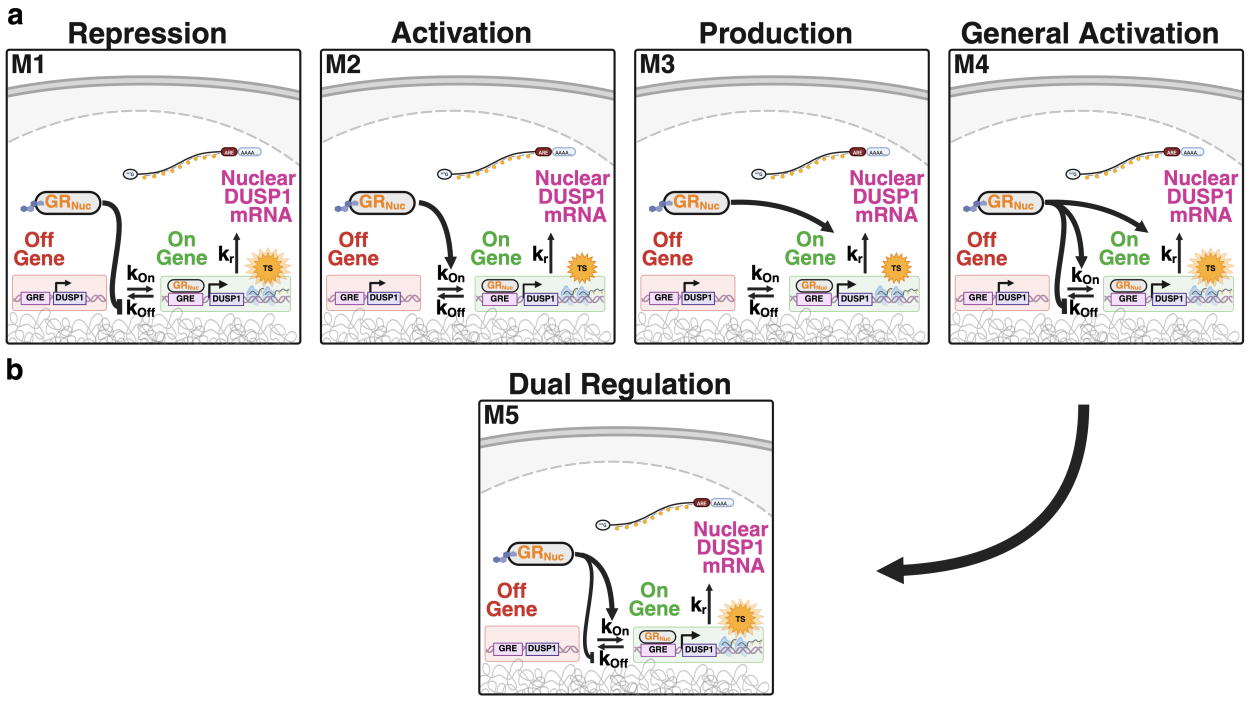


Figure 2.13: Alternative models of GR-dependent *DUSP1* transcriptional regulation. Schematic representation of promoter-level models describing how nuclear GR (GR_{nuc}) regulates *DUSP1* transcriptional bursting. The promoter transitions between OFF and ON states with rates k_{on} and k_{off} and produces nascent transcripts at rate k_r when active. GR-dependent regulation is implemented through modulation of individual or combined parameters across models M1–M5. Log-likelihood contributions from nuclear mRNA (Nuc), transcription sites (TS), and the combined dataset (Total), along with the Bayesian Information Criterion (BIC), are reported below each schematic. **(a) M1, Repression:** GR inhibits k_{off}, stabilizing the ON state. **(b) M2, Activation:** GR increases k_{on}. **(c) M3, Production:** GR directly increases the transcription rate k_r. **(d) M4, General Activation:** GR modulates k_{on}, k_{off}, and k_r. **(e) M5, Dual Regulation:** GR modulates k_{on} and k_{off} with no basal off-state transcription. Models in which GR modulates k_{on} (M2, M4, M5) substantially outperform k_{off}-only (M1) and k_r-only (M3) regulation, consistent with a dominant role for GR-driven burst-frequency control.

Table 2.3: Comparison of alternative *DUSP1* nuclear promoter-regulation models (M1–M5). Log-posterior ratios $\log(\mathrm{MAP}/\mathrm{MAP}_{\mathrm{best}})$ are reported separately for nuclear mRNA (Nuc), transcription-site intensity (TS), and the combined dataset (Tot); ΔAIC, ΔBIC, and the approximate log Bayes factor are relative to the best model (M5). Less negative values indicate better agreement. The dual-regulation model M5 was selected (see Figure 2.13).

	M1	M2	M3	M4	M5
GR-modulated	k_{off}	k_{on}	k_r	$k_{\mathrm{on}}, k_{\mathrm{off}}, k_r$	$k_{\mathrm{on}}, k_{\mathrm{off}}$
Num. parameters	7	7	7	9	8
$\log(\mathrm{MAP}/\mathrm{MAP}_{\mathrm{best}})_{\mathrm{Nuc}}$	-54	-16	-218	-0	0
$\log(\mathrm{MAP}/\mathrm{MAP}_{\mathrm{best}})_{\mathrm{TS}}$	-90	0	-132	-11	-11
$\log(\mathrm{MAP}/\mathrm{MAP}_{\mathrm{best}})_{\mathrm{Tot}}$	-133	-5	-339	-0	0
$\mathrm{AIC} - \mathrm{AIC}_{\mathrm{best}}$	264	9	676	2	0
$\mathrm{BIC} - \mathrm{BIC}_{\mathrm{best}}$	258	2	669	8	0
$\log(\mathrm{BF}_{\mathrm{approx}})$	-129	-1	-335	-4	0

2.5.5 *DUSP1* cytoplasmic regulation and model discrimination

Cytoplasmic model. The cytoplasmic module adds one species, cytoplasmic *DUSP1* mRNA ($DUSP1_{\mathrm{cyt}}$, `rCyt`), with initial condition $DUSP1_{\mathrm{cyt}} = 0$. It is produced by nuclear export (reaction 9, the same $k_{Nuc2Cyt}$ process introduced in Section 2.5.4, now tracking the cytoplasmic product) and removed by degradation (reaction 10):

$$(9) \quad DUSP1_{\mathrm{nuc}} \rightarrow DUSP1_{\mathrm{cyt}} : \; w_9 = k_{Nuc2Cyt}\, DUSP1_{\mathrm{nuc}} \quad \text{(nuclear export)}$$

$$(10) \quad DUSP1_{\mathrm{cyt}} \rightarrow \varnothing : \; w_{10} = w_{\mathrm{deg}} \quad \text{(cytoplasmic degradation)}$$

The four candidate models differ only in the degradation propensity w_{deg}. Writing $r_{\mathrm{cyt}} \equiv DUSP1_{\mathrm{cyt}}$, free mRNA degrades at the basal rate $k_{degCyt,0}$ and TTP-bound mRNA at the enhanced rate $k_{degCyt,1}$, so

$$w_{\mathrm{deg}} = k_{degCyt,0}\, r_{\mathrm{cyt}} + (k_{degCyt,1} - k_{degCyt,0})\, r^*_{\mathrm{cyt}}, \tag{2.9}$$

where r^*_{cyt} is the TTP-bound mRNA, obtained from a rapid-equilibrium binding assumption. In the mechanistic model (Section 2.5.6), reaction 10 is resolved into basal decay (reaction 10a), reversible TTP binding (reaction 10b), and catalyzed decay (reaction 10c).

Saturating TTP-bound term. Total cytoplasmic mRNA $r_{\mathrm{cyt}} = r_{\mathrm{cyt,F}} + r^*_{\mathrm{cyt}}$ splits into free and TTP-bound pools, and total TTP $TTP_{\mathrm{tot}} = TTP_{\mathrm{F}} + r^*_{\mathrm{cyt}}$ into free and mRNA-bound pools. Assuming rapid reversible binding of free mRNA and free TTP,

$$r_{\mathrm{cyt,F}} + TTP_{\mathrm{F}} \underset{k_-}{\overset{k_+}{\rightleftharpoons}} r^*_{\mathrm{cyt}}, \tag{2.10}$$

the equilibrium balance $k_+\, r_{\mathrm{cyt,F}}\, TTP_{\mathrm{F}} = k_-\, r^*_{\mathrm{cyt}}$ defines the dissociation constant

$$k_{DTTP} \equiv \frac{k_-}{k_+} = \frac{r_{\mathrm{cyt,F}}\, TTP_{\mathrm{F}}}{r^*_{\mathrm{cyt}}} = \frac{(r_{\mathrm{cyt}} - r^*_{\mathrm{cyt}})(TTP_{\mathrm{tot}} - r^*_{\mathrm{cyt}})}{r^*_{\mathrm{cyt}}}. \tag{2.11}$$

Rearranging gives a quadratic in r^*_{cyt},

$$r^*_{\mathrm{cyt}}{}^2 - (r_{\mathrm{cyt}} + TTP_{\mathrm{tot}} + k_{DTTP})\, r^*_{\mathrm{cyt}} + r_{\mathrm{cyt}}\, TTP_{\mathrm{tot}} = 0, \tag{2.12}$$

whose physical (smaller) root is

$$r^*_{\mathrm{cyt}}(r_{\mathrm{cyt}}, TTP_{\mathrm{tot}}) = \tfrac{1}{2}\Big[(r_{\mathrm{cyt}} + TTP_{\mathrm{tot}} + k_{DTTP}) - \sqrt{(r_{\mathrm{cyt}} + TTP_{\mathrm{tot}} + k_{DTTP})^2 - 4\, r_{\mathrm{cyt}}\, TTP_{\mathrm{tot}}}\Big]. \tag{2.13}$$

The total TTP is either held constant or follows the time-varying signal $I_{\mathrm{TTP}}(t)$ (Equation 2.3).

Candidate models. The four candidate decay models combine these choices with Equation 2.9:

- **Model 1 – Basal first-order degradation:** no TTP binding ($r^*_{\mathrm{cyt}} = 0$), so $w_{\mathrm{deg}} = k_{degCyt,0}\, r_{\mathrm{cyt}}$.
- **Model 2 – Saturable, no time-varying induction:** Equation 2.13 with TTP_{tot} fixed at its basal value 1, so $w_{\mathrm{deg}} = k_{degCyt,0}\, r_{\mathrm{cyt}} + (k_{degCyt,1} - k_{degCyt,0})\, r^*_{\mathrm{cyt}}(r_{\mathrm{cyt}},\, 1)$.
- **Model 3 – Time-varying input, no saturation:** bound mRNA approximated as $I_{\mathrm{TTP}}(t)\, r_{\mathrm{cyt}}$, so $w_{\mathrm{deg}} = k_{degCyt,0}\, r_{\mathrm{cyt}} + (k_{degCyt,1} - k_{degCyt,0})\, I_{\mathrm{TTP}}(t)\, r_{\mathrm{cyt}}$.

- **Model 4 – Time-varying, saturable (selected):** Equation 2.13 with $TTP_{\mathrm{tot}} = I_{\mathrm{TTP}}(t)$, so $w_{\mathrm{deg}} = k_{degCyt,0}\, r_{\mathrm{cyt}} + (k_{degCyt,1} - k_{degCyt,0})\, r^{*}_{\mathrm{cyt}}(r_{\mathrm{cyt}},\, I_{\mathrm{TTP}}(t))$.

Model discrimination. The four decay models were fit jointly with the selected nuclear module (M5) to the 100 nM Dex smiFISH data using SSA trajectories and approximate Bayesian computation, with the combined objective evaluated against nuclear and cytoplasmic mRNA marginals and transcription-site intensity (Table 2.4, Figure 2.14). All four models reproduced the mean nuclear and cytoplasmic mRNA trajectories, but only the time-varying, saturable Model 4 reproduced the variance dynamics and variance-mean relationships in both compartments; the simpler models systematically misestimated either nuclear or cytoplasmic variability. Model 4 also gave the smallest total fit and prediction errors of the four phenomenological models (Table 2.4), and was therefore selected. A fully mechanistic TTP network (Section 2.5.6) reproduces the same data and corroborates this choice. The biological interpretation is developed in Section 2.2.6.

Table 2.4: Fit and prediction errors across cytoplasmic *DUSP1* degradation models. Each column is a cytoplasmic decay mechanism paired with the selected nuclear model (M5): Linear Constant (Model 1, first-order), Nonlinear Constant (Model 2, saturable), Linear Time-Varying (Model 3, time-varying), Nonlinear Time-Varying (Model 4, time-varying and saturable; selected), and Detailed Mechanistic (the full TTP network, Section 2.5.6). Values are $\log(\mathrm{MAP}/\mathrm{MAP}_{\mathrm{best}})$ per dataset; less negative is better. Fit datasets were used for inference; prediction datasets were held out.

Data set	Linear Constant	Nonlinear Constant	Linear Time-Varying	Nonlinear Time-Varying	Detailed Mechanistic
Nuc/Cyt, 100 nM Dex (fit)	-126	-210	-102	0	-3
TS, 100 nM Dex (fit)	-3	-1	-2	0	-0
Nuc/Cyt, 0 min TPL (fit)	-17	-26	-30	-12	0
Total fit error	$\mathbf{-146}$	$\mathbf{-237}$	$\mathbf{-134}$	$\mathbf{-12}$	$\mathbf{-3}$
Nuc/Cyt, 0.3 nM Dex (predict)	-22	-23	-43	-17	0
Nuc/Cyt, 1.0 nM Dex (predict)	-31	-57	-35	-15	0
Nuc/Cyt, 10 nM Dex (predict)	-43	-76	-47	-2	0
TS, 0.3 nM Dex (predict)	-0	-0	-0	0	-4
TS, 1.0 nM Dex (predict)	-1	-0	0	-0	-2
TS, 10 nM Dex (predict)	-1	-2	-1	0	-0
Nuc/Cyt, 20 min TPL (predict)	-11	-37	-7	0	-1
Nuc/Cyt, 75 min TPL (predict)	-1	-8	-5	0	-1
Nuc/Cyt, 150 min TPL (predict)	-22	-38	-20	0	-10
Nuc/Cyt, 180 min TPL (predict)	-6	-26	-8	-8	0
Total prediction error	$\mathbf{-139}$	$\mathbf{-269}$	$\mathbf{-165}$	$\mathbf{-41}$	$\mathbf{-19}$

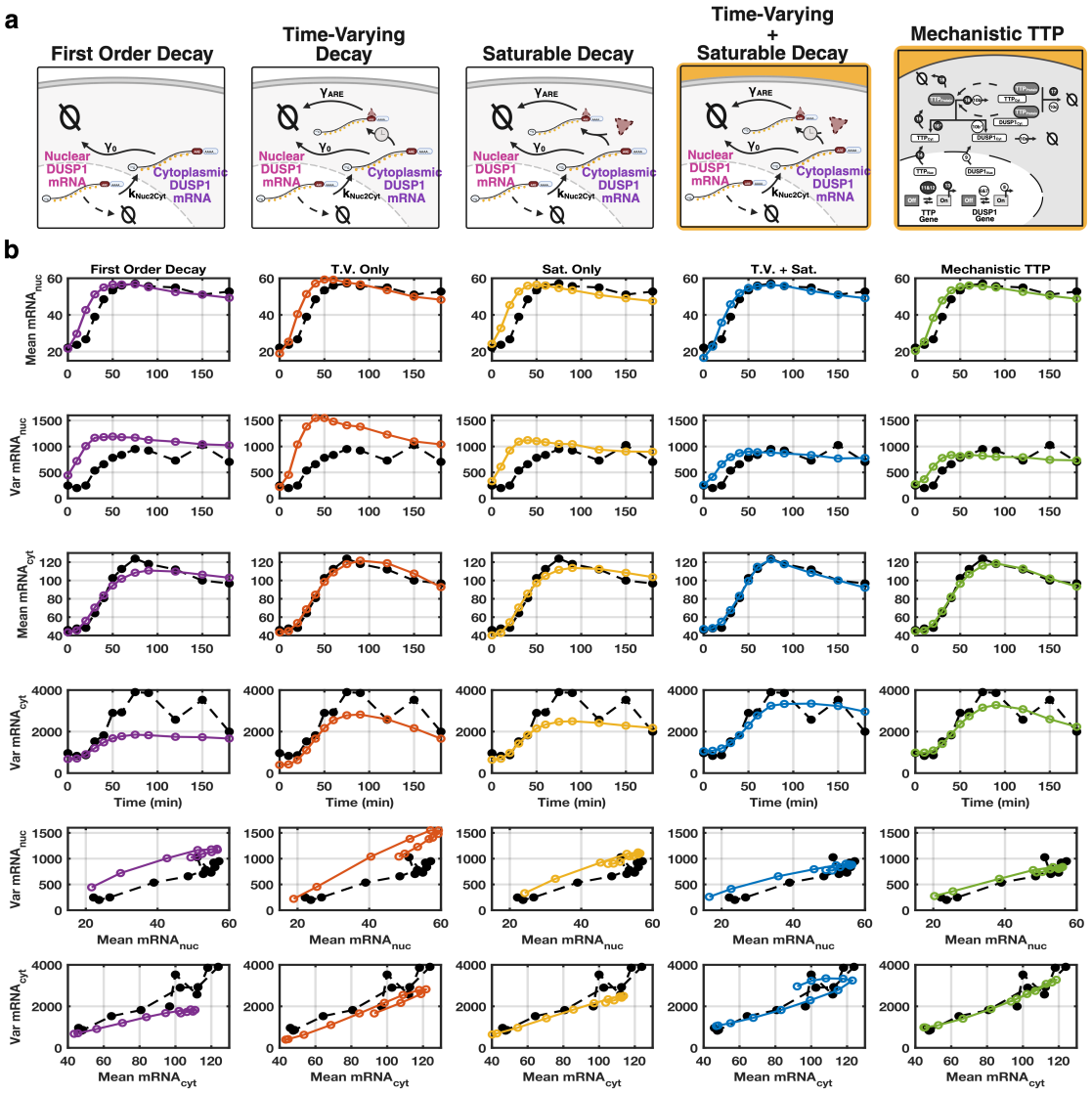


Figure 2.14: Alternative models of cytoplasmic *DUSP1* mRNA degradation. (a) Five candidate mechanisms for cytoplasmic *DUSP1* mRNA decay (left to right): **First Order Decay** (purple), a constant rate γ_0; **Time-Varying Decay** (orange) and **Saturable Decay** (yellow), each adding an ARE-mediated term γ_{ARE} with either explicit time dependence or abundance-dependent saturation; **Time-Varying + Saturable Decay** (blue), combining both into the phenomenological input $I_{\mathrm{TTP}}(t)$; and the full **Mechanistic TTP** model (green). Gold highlighting indicates the models retained for downstream analyses. **(b)** Model fits (colored open circles) versus single-cell smiFISH data (black dashed lines) for the 100 nM Dex time course. Rows, top to bottom: mean and variance of nuclear *DUSP1* mRNA versus time; mean and variance of cytoplasmic *DUSP1* mRNA versus time; and the variance–mean relationships for nuclear and cytoplasmic mRNA. All five models reproduce the mean trajectories comparably, so means alone do not discriminate among mechanisms. Only the models combining time-varying and saturable ARE-mediated decay (T.V. + Sat. and Mechanistic TTP) reproduce the variance dynamics and variance–mean relationships in both compartments; the First Order, T.V.-only, and Sat.-only models misestimate the nuclear and cytoplasmic variances. The agreement between the semi-mechanistic T.V. + Sat. model and the full Mechanistic TTP model supports $I_{\mathrm{TTP}}(t)$ as a compact, identifiable representation of TTP-driven ARE-dependent mRNA decay.

2.5.6 Full mechanistic GR-DUSP1-TTP network

The semi-mechanistic model of Section 2.5.5 represents ARE-mediated cytoplasmic decay through the phenomenological input $I_{\mathrm{TTP}}(t)$ (Equation 2.3), which reproduces the time-varying, saturable behavior expected of TTP-driven decay without modeling TTP itself. To confirm that this compact term is consistent with the underlying biochemistry, the reaction network was extended to resolve Dex-induced *TTP* expression and TTP-catalyzed mRNA decay explicitly (Figure 2.15).

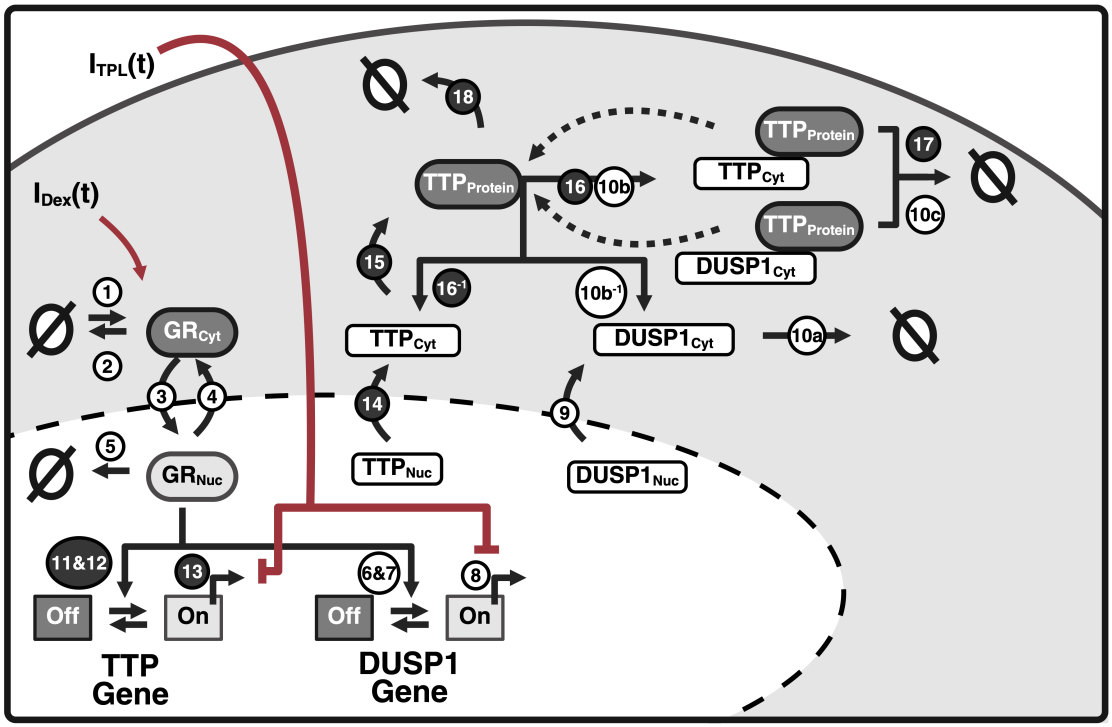


Figure 2.15: Mechanistic model extension incorporating TTP-mediated post-transcriptional regulation. To verify ARE-dependent mRNA decay via $I_{\mathrm{TTP}}(t)$, the semi-mechanistic model was extended to include TTP expression dynamics in response to Dex. New species include ON and OFF TTP gene states, nuclear and cytoplasmic *TTP* mRNA, TTP protein, and transient TTP–mRNA complexes. Nuclear GR promotes *TTP* gene activation (**reaction 11**), followed by transcription (**reaction 13**), nuclear export (**reaction 14**), translation (**reaction 15**), and protein degradation (**reaction 18**), with basal gene deactivation (**reaction 12**). TTP protein catalyzes degradation of both *DUSP1* and *TTP* cytoplasmic mRNA (**reaction 10**a–c, **reaction 17**) without being consumed (dotted line). TPL input, $I_{\mathrm{TPL}}(t)$, inhibits transcription of both *DUSP1* and *TTP*. As *TTP* mRNA and protein were not directly measured, their dynamics are inferred through their effects on *DUSP1* mRNA distributions.

Extended species. The mechanistic model adds the *TTP* gene ON and OFF states, nuclear and cytoplasmic *TTP* mRNA (TTP_{nuc}, TTP_{cyt}), TTP protein (TTP_{prot}), and the transient TTP–mRNA complexes formed on cytoplasmic *DUSP1* and *TTP* transcripts. Because *TTP* mRNA and protein were not measured directly, their dynamics are constrained only indirectly, through their effect on the measured *DUSP1* mRNA distributions.

Extended reactions. Nuclear GR drives the TTP module in parallel with its action on *DUSP1*, and TTP protein then closes a negative-feedback loop onto both transcripts:

- ***TTP* expression (reactions 11–15, 18):** GR_{nuc}-dependent *TTP* gene activation (reaction 11, $k_{on,1}^{\mathrm{TTP}}$) with basal inactivation (reaction 12, k_{off}^{TTP}); *TTP* transcription (reaction 13, $k_{r,on}^{\mathrm{TTP}}$), inhibited by $I_{\mathrm{TPL}}(t)$ as for *DUSP1*; nuclear export (reaction 14, $k_{Nuc2Cyt}^{\mathrm{TTP}}$); translation (reaction 15, k_{tl}); and TTP protein degradation (reaction 18, γ_p). Basal *TTP* mRNA decay proceeds at rate γ_0^{TTP}.
- **TTP-catalyzed *DUSP1* decay (reactions 10a–10c):** basal first-order decay of cytoplasmic *DUSP1* mRNA is retained (reaction 10a, $k_{degCyt,0}$); TTP protein binds cytoplasmic *DUSP1* mRNA reversibly to form a transient complex (reaction 10b, forward k_b, reverse k_u, cooperativity η_{TTP}); the complex either dissociates or proceeds to catalyzed degradation, releasing the TTP protein (reaction 10c, $k_{degCyt,1}$).
- **TTP autoregulation (reactions 16–17):** TTP protein binds cytoplasmic *TTP* mRNA (reaction 16, k_b/k_u, η_{TTP}) and catalyzes its degradation (reaction 17), imposing the same ARE-mediated negative feedback on its own transcript.

In every binding reaction the TTP protein is released rather than consumed, so it acts catalytically. Reactions 10a–10c resolve the lumped cytoplasmic degradation (reaction 10) of the semi-mechanistic model into its basal and TTP-dependent components; the inferred mechanistic parameters are reported in Section 2.5.8.

Verification. The close agreement between the semi-mechanistic and fully mechanistic models for both the mean and the variance of nuclear and cytoplasmic *DUSP1* mRNA (Figure 2.14b; Table 2.4) confirms that the phenomenological input $I_{\mathrm{TTP}}(t)$ is a faithful and identifiable surrogate

for the explicit TTP regulatory circuit. Because the mechanistic extension adds ten parameters that are constrained only indirectly by *DUSP1* data, the semi-mechanistic model is retained for all downstream analyses, with the mechanistic network serving as a biophysical consistency check rather than as the primary inference model.

2.5.7 Parameter uncertainty quantification

The three final models were fit sequentially: the compartment-specific GR model first, then the *DUSP1* nuclear and transcription-site model using the inferred GR dynamics, and finally the cytoplasmic *DUSP1* model using the fitted GR and nuclear parameters. For each of these models, point estimates (MAP/MLE) were complemented by full posterior uncertainty quantification using Metropolis–Hastings (MH) Markov chain Monte Carlo sampling.

Method. Sampling was performed in $\log_{10}$ parameter space, with the target density given by the same combined objective used for inference: the FSP likelihood over the measured single-cell distributions, the transcription-site likelihood, and the log-priors over the free parameters; for the cytoplasmic model, stochastic simulation with approximate Bayesian computation supplied the nuclear and cytoplasmic mRNA marginals. Posterior samples were summarized in linear scale as the posterior mean and standard deviation for every parameter (reported for the GR model in Table 2.5, for the semi-mechanistic model in Table 2.7, and for the mechanistic model in Table 2.8) and visualized two ways: pairwise joint distributions, in which each panel shows the density of MH samples for a parameter pair with a 95% confidence ellipse, and single-parameter marginal posteriors, in which a histogram and kernel-density estimate of the samples are overlaid on the prior. Across all three models the marginal posteriors are substantially narrower than their priors, indicating that the parameters are well constrained by the single-cell data, while the joint distributions reveal the expected correlations among kinetically coupled parameters.

2.5.8 Shared parameters and final parameter inventory

This section consolidates the inferred parameters for the three final models. The compartment-specific GR model supplies the GR transport dynamics that drive every downstream module

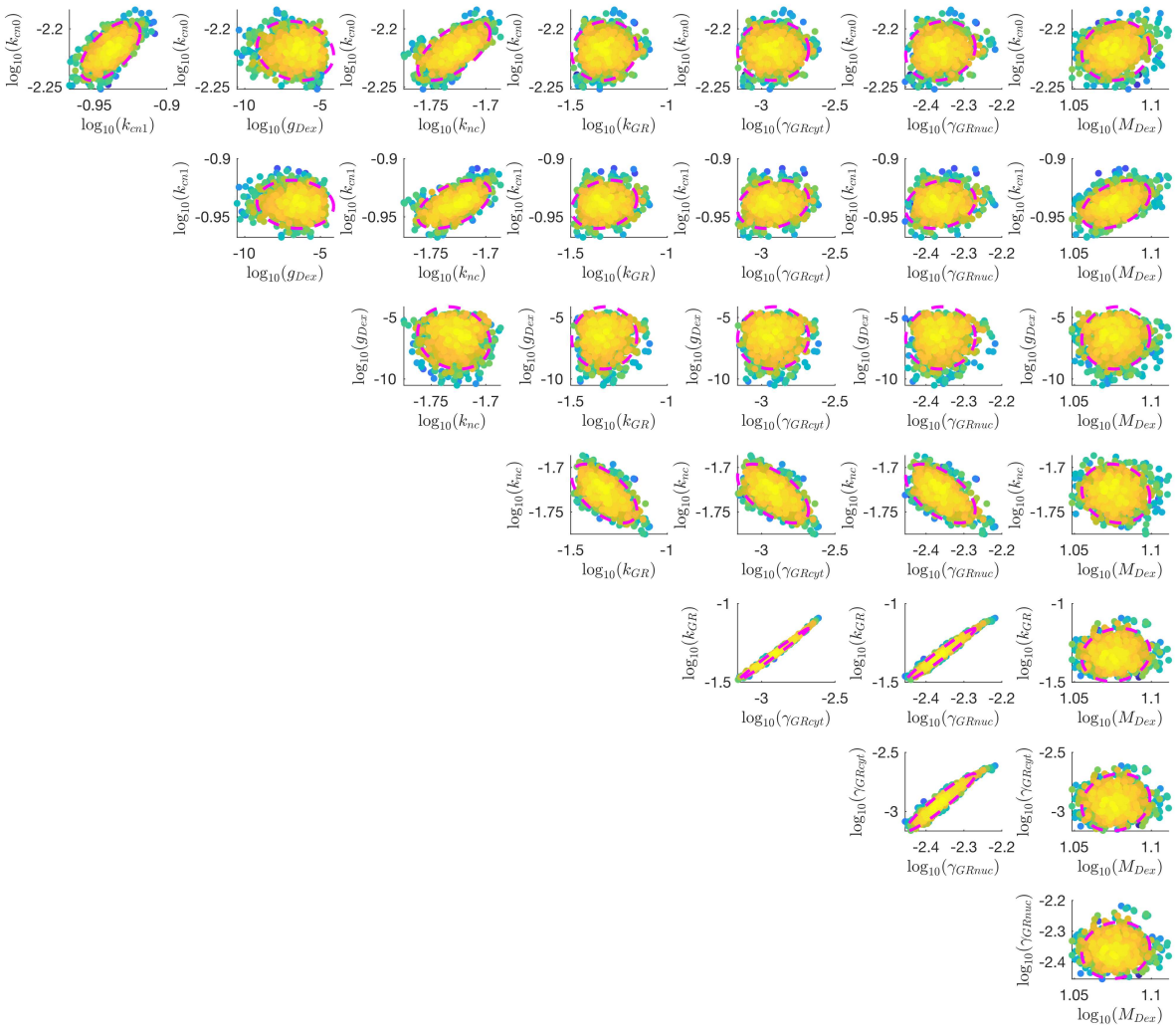


Figure 2.16: Joint posterior distribution for the compartment-specific GR model. Uncertainty quantification for the chosen GR model, obtained by Metropolis–Hastings MCMC sampling. Each subplot shows the pairwise joint distribution of MCMC samples for two model parameters (in $\log_{10}$ space), with points colored by sample density. The magenta dashed ellipse marks the 95% confidence interval.

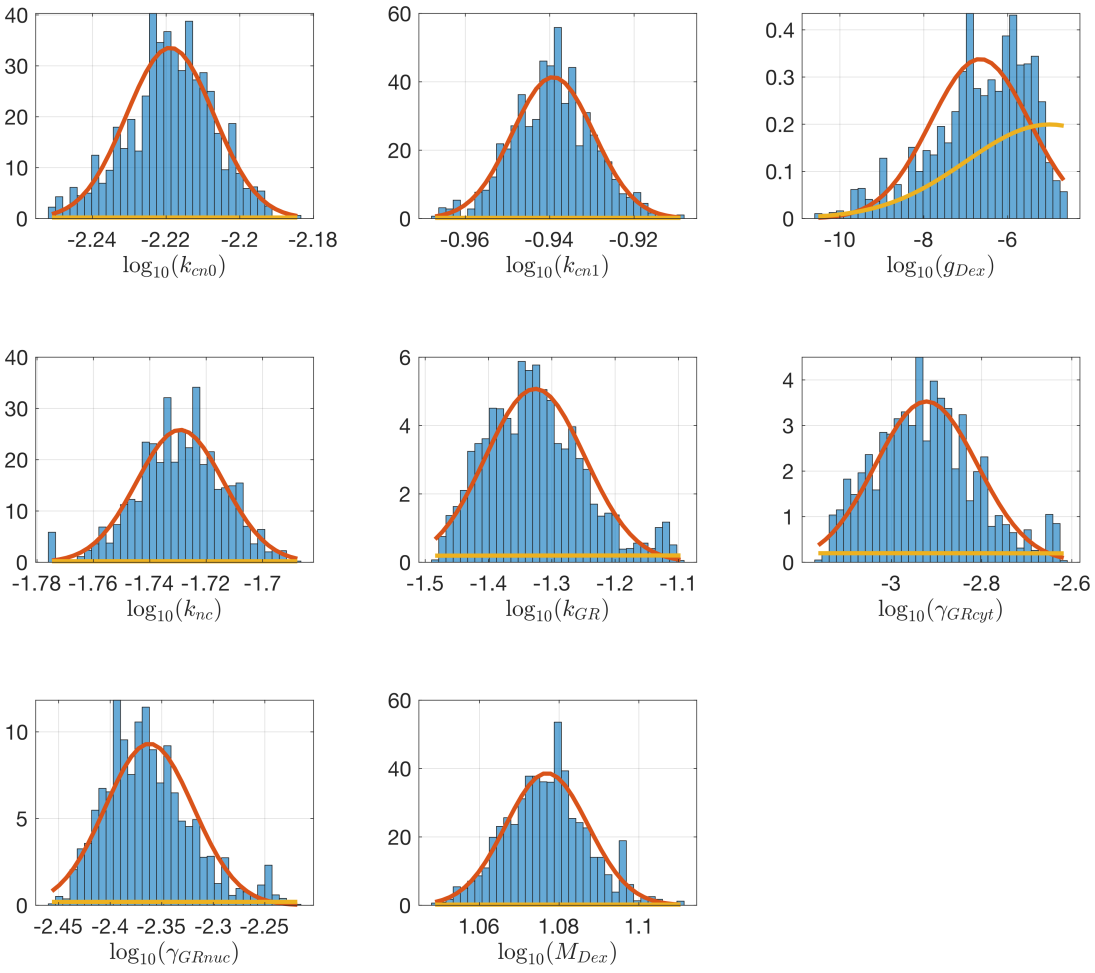


Figure 2.17: Marginal posterior distributions for the compartment-specific GR model. Single-parameter marginal posteriors for the chosen GR model, obtained by Metropolis–Hastings MCMC sampling. Each panel shows one model parameter (in $\log_{10}$ space): the blue histogram is the distribution of MCMC samples, the red curve is a kernel density estimate of the marginal posterior, and the gold curve is the prior.

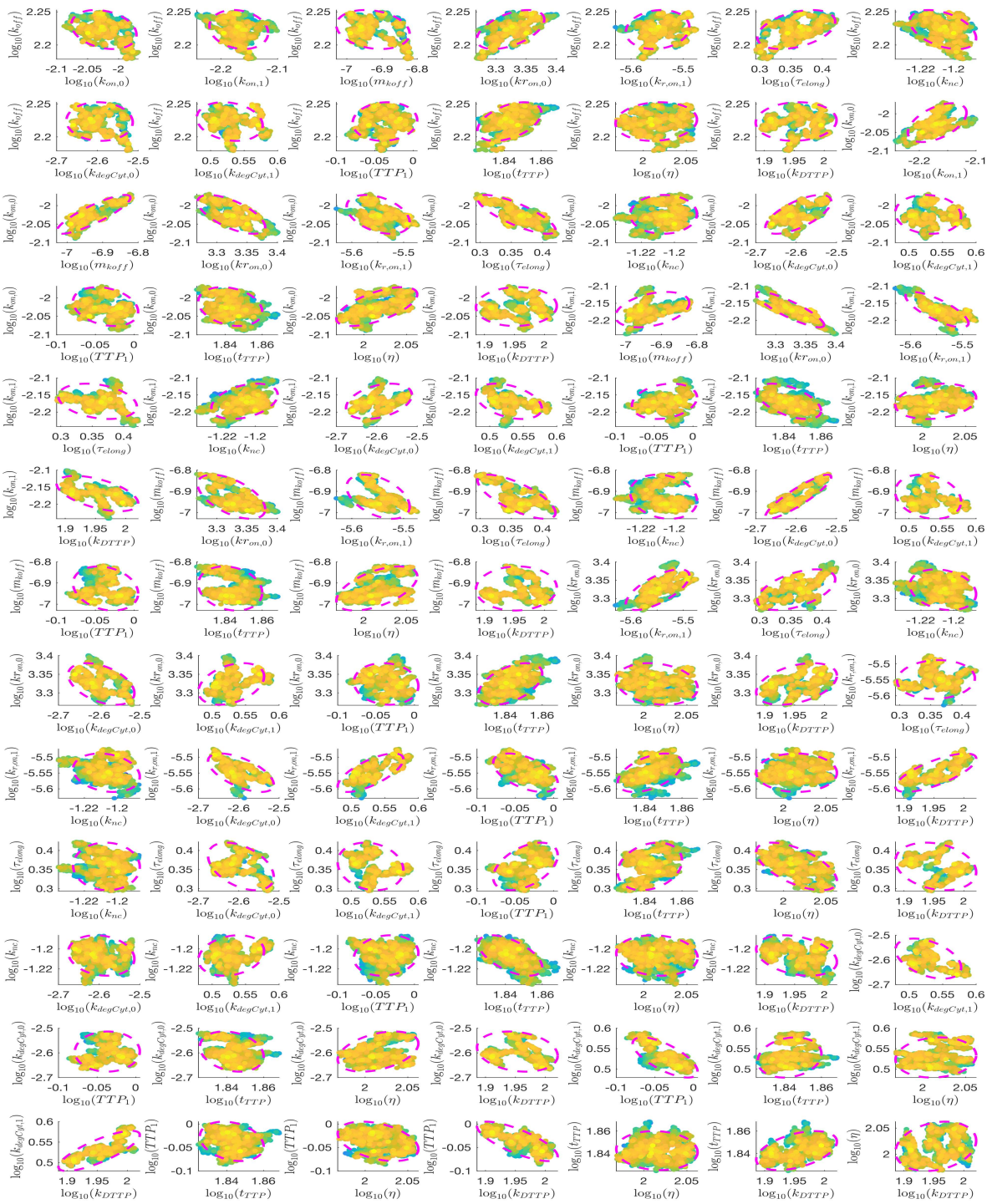


Figure 2.18: Joint posterior distribution for the semi-mechanistic *DUSP1* model. Uncertainty quantification for the semi-mechanistic *DUSP1* model, obtained by Metropolis–Hastings MCMC sampling. Each subplot shows the pairwise joint distribution of MCMC samples for two model parameters (in $\log_{10}$ space), with points colored by sample density. The magenta dashed ellipse marks the 95% confidence interval.

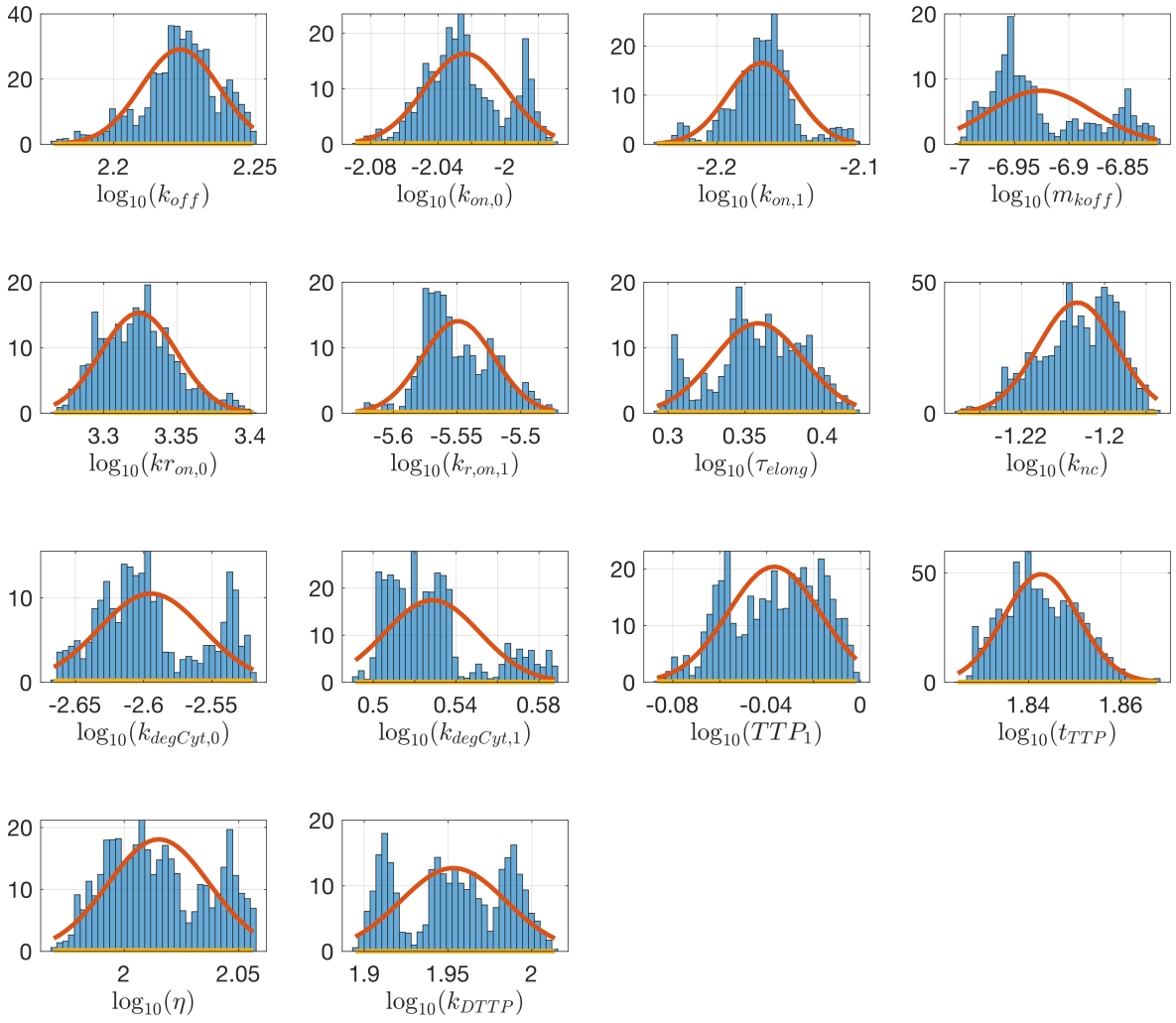


Figure 2.19: Marginal posterior distributions for the semi-mechanistic *DUSP1* model. Single-parameter marginal posteriors for the semi-mechanistic *DUSP1* model, obtained by Metropolis–Hastings MCMC sampling. Each panel shows one model parameter (in $\log_{10}$ space): the blue histogram is the distribution of MCMC samples, the red curve is a kernel density estimate of the marginal posterior, and the gold curve is the prior.

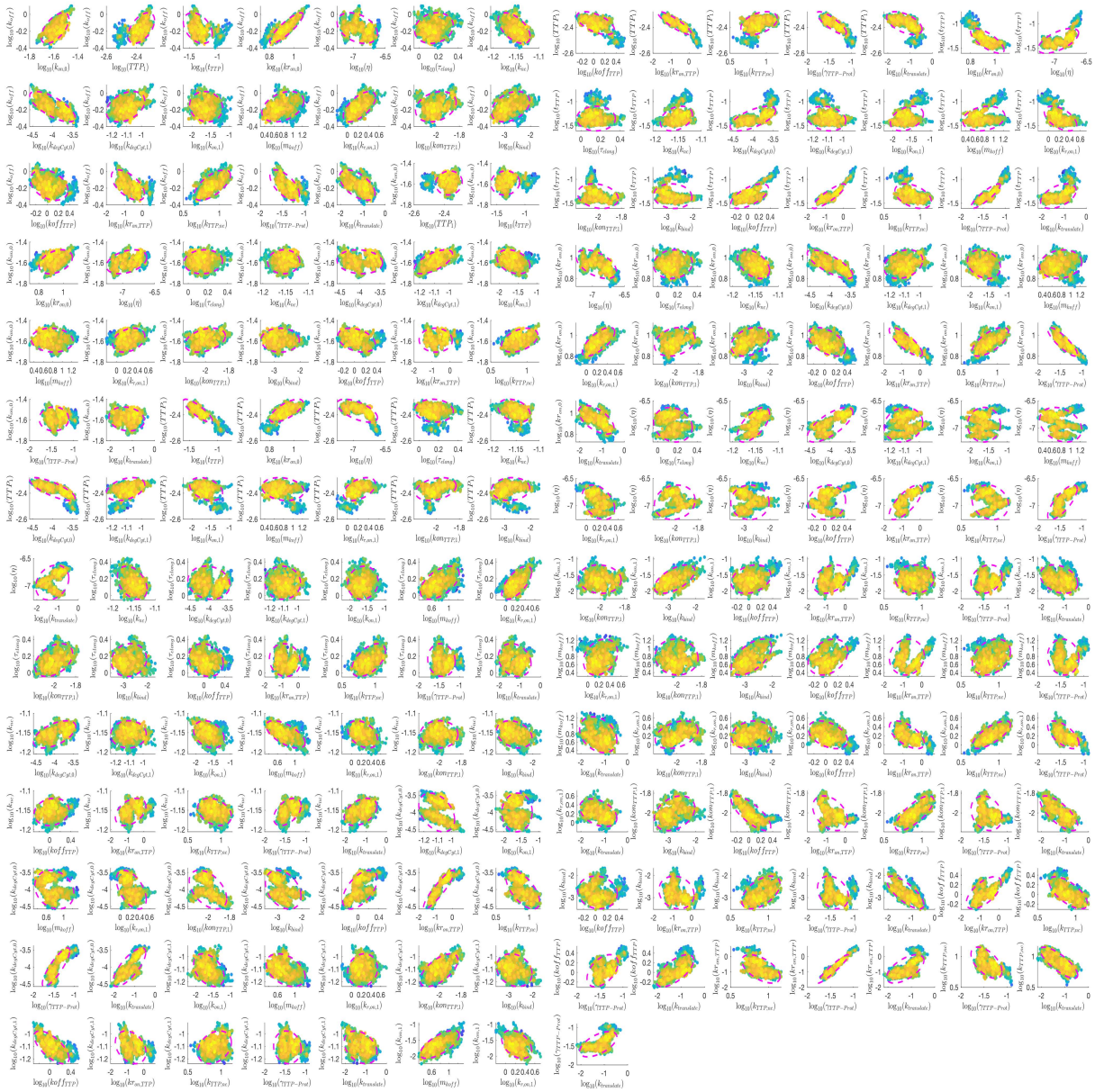


Figure 2.20: Joint posterior distribution for the mechanistic *DUSP1* model. Uncertainty quantification for the mechanistic *DUSP1* model, obtained by Metropolis–Hastings MCMC sampling. Each subplot shows the pairwise joint distribution of MCMC samples for two model parameters (in $\log_{10}$ space), with points colored by sample density. The magenta dashed ellipse marks the 95% confidence interval.

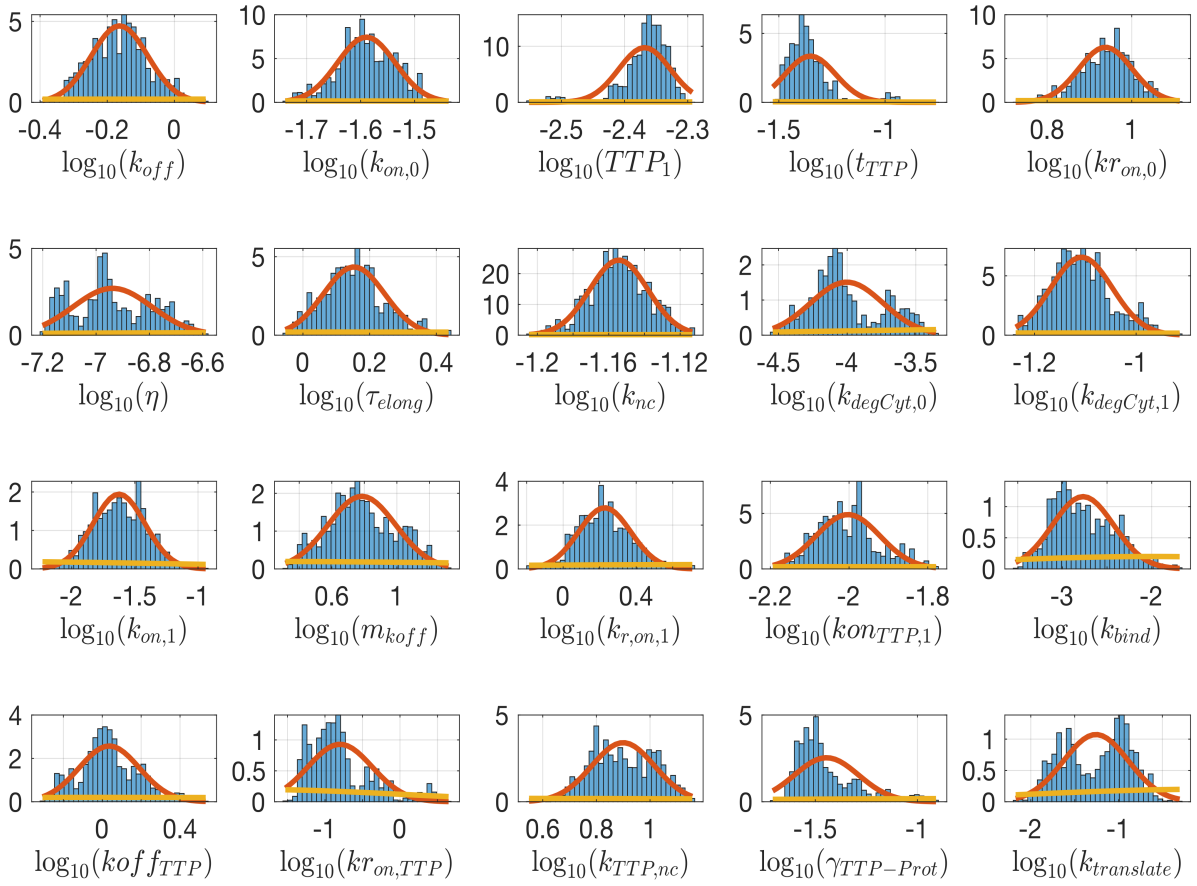


Figure 2.21: Marginal posterior distributions for the mechanistic *DUSP1* model. Single-parameter marginal posteriors for the mechanistic *DUSP1* model, obtained by Metropolis–Hastings MCMC sampling. Each panel shows one model parameter (in $\log_{10}$ space): the blue histogram is the distribution of MCMC samples, the red curve is a kernel density estimate of the marginal posterior, and the gold curve is the prior.

(Table 2.5). The *DUSP1* parameters are then compared across model structures, from nuclear-only fits to the full semi-mechanistic and mechanistic models (Table 2.6). Finally, the posterior mean and standard deviation from Metropolis–Hastings sampling are reported for the selected semi-mechanistic model (Table 2.7) and for the mechanistic model (Table 2.8); in each case the maximum-likelihood column reproduces the corresponding point estimates in Table 2.6, now with their inferred uncertainties.

Table 2.5: Inferred parameters for the compartment-specific GR model. Maximum-likelihood estimates and posterior mean ± standard deviation from Metropolis–Hastings sampling (linear scale). The Dex clearance rate γ_{Dex} is effectively zero, indicating negligible glucocorticoid degradation over the experiment.

Description (units)	**Parameter**	**MLE**	**Posterior mean ± STD**
GR import, basal (min^{-1})	k_{cn0}	6.02×10^{-3}	$6.04 \times 10^{-3} \pm 1.65 \times 10^{-4}$
GR import, Dex-dependent (min^{-1})	k_{cn1}	1.15×10^{-1}	$1.15 \times 10^{-1} \pm 2.56 \times 10^{-3}$
Dex clearance rate (min^{-1})	γ_{Dex}	6.76×10^{-7}	$1.66 \times 10^{-6} \pm 3.15 \times 10^{-6}$
GR nuclear export (min^{-1})	k_{nc}	1.88×10^{-2}	$1.87 \times 10^{-2} \pm 6.61 \times 10^{-4}$
GR synthesis, cytoplasmic (min^{-1})	k_g	4.82×10^{-2}	$4.80 \times 10^{-2} \pm 9.20 \times 10^{-3}$
GR degradation, cytoplasmic (min^{-1})	γ_{GRcyt}	1.24×10^{-3}	$1.24 \times 10^{-3} \pm 3.42 \times 10^{-4}$
GR degradation, nuclear (min^{-1})	γ_{GRnuc}	4.40×10^{-3}	$4.37 \times 10^{-3} \pm 4.47 \times 10^{-4}$
Michaelis constant, Dex import (nM)	M_{Dex}	1.17×10^{1}	$1.19 \times 10^{1} \pm 2.84 \times 10^{-1}$

Table 2.6: Inferred *DUSP1*- and TTP-related parameter values across model variants. The two nuclear columns are nuclear-only fits (general activation, all GR couplings free; and activation only, k_{on} coupling). The semi-mechanistic column is the selected full model (nuclear module plus the time-varying, saturable cytoplasmic decay of Equation 2.13); the mechanistic column adds the explicit TTP network (Figure 2.15). Em-dashes (—) indicate parameters absent from that model. Symbols follow the chapter glossary.

Description (units)	**Parameter**	**Nuclear** (gen. act.)	**Nuclear** (k_{on} only)	**Semi-mechanistic**	**Mechanistic**
DUSP1 nuclear module					
Basal gene inactivation rate (min^{-1})	k_{off}	1.83×10^{0}	1.73×10^{0}	6.99×10^{1}	6.11×10^{-1}
Basal gene activation rate (min^{-1})	$k_{\text{on},0}$	1.63×10^{-2}	1.00×10^{-2}	4.06×10^{-3}	3.55×10^{-2}
nucGR-dependent gene activation rate (min^{-1})	$k_{\text{on},1}$	3.11×10^{-3}	3.63×10^{-3}	6.97×10^{-3}	3.48×10^{-3}
nucGR modulation of inactivation (molecules^{-1})	m_{koff}	1.74×10^{-2}	—	2.25×10^{-7}	7.86×10^{-2}
Basal *DUSP1* transcription rate (min^{-1})	$k_{r,\text{on},0}$	1.77×10^{1}	2.08×10^{1}	8.80×10^{2}	6.79×10^{0}
nucGR-dependent *DUSP1* transcription rate (min^{-1})	$k_{r,\text{on},1}$	9.97×10^{-6}	—	4.42×10^{-7}	2.44×10^{-7}
DUSP1 elongation time (min)	τ_{elong}	2.67×10^{0}	2.67×10^{0}	1.76×10^{0}	1.36×10^{0}
DUSP1 nuclear export rate (min^{-1})	k_{Nuc2Cyt}	3.17×10^{-2}	3.16×10^{-2}	6.07×10^{-2}	7.12×10^{-2}
DUSP1 cytoplasmic degradation (semi-mechanistic; see Equation 2.13)					
Basal *DUSP1* mRNA degradation rate (min^{-1})	$k_{\text{degCyt},0}$	—	—	1.58×10^{-3}	5.07×10^{-4}
Max TTP-dependent degradation rate (min^{-1})	$k_{\text{degCyt},1}$	—	—	3.53×10^{0}	8.74×10^{-2}

Continued on next page

(Table 2.6 continued)

Description (units)	**Parameter**	**Nuclear** (gen. act.)	**Nuclear** (k_{on} only)	**Semi-mechanistic**	**Mechanistic**
Max fold-change in TTP-mediated degradation	TTP_1	—	—	1.02×10^{0}	—
Half-max time for TTP activity (min)	t_{TTP}	—	—	6.82×10^{1}	—
Hill coefficient, TTP time-dependence	η	—	—	2.68×10^{1}	—
TTP–mRNA binding saturation (molecules)	k_{DTTP}	—	—	1.07×10^{2}	—
TTP module (mechanistic only; see Figure 2.15)					
nucGR-dependent TTP gene activation rate (min^{-1})	$k_{\mathrm{on,1}}^{\mathrm{TTP}}$	—	—	—	2.10×10^{-2}
TTP gene inactivation rate (min^{-1})	$k_{\mathrm{off}}^{\mathrm{TTP}}$	—	—	—	2.26×10^{0}
TTP transcription rate (min^{-1})	$k_{r,\mathrm{on}}^{\mathrm{TTP}}$	—	—	—	1.02×10^{0}
TTP nuclear export rate (min^{-1})	$k_{\mathrm{Nuc2Cyt}}^{\mathrm{TTP}}$	—	—	—	1.17×10^{-2}
Basal TTP mRNA degradation rate (min^{-1})	γ_0^{TTP}	—	—	—	2.09×10^{-3}
TTP translation rate (min^{-1})	k_{tl}	—	—	—	6.65×10^{-1}
TTP protein degradation rate (min^{-1})	γ_p	—	—	—	1.42×10^{0}
TTP–mRNA binding rate (min^{-1} mol^{-1})	k_b	—	—	—	4.21×10^{0}
TTP–mRNA unbinding rate (min^{-1})	k_u	—	—	—	4.11×10^{-2}

Continued on next page

(Table 2.6 continued)

Description (units)	**Parameter**	**Nuclear** (gen. act.)	**Nuclear** (k_{on} only)	**Semi-mechanistic**	**Mechanistic**
Hill coefficient, TTP–mRNA binding	η_{TTP}	—	—	—	7.48×10^{-2}

Table 2.7: Posterior parameters for the selected semi-mechanistic *DUSP1* model. Maximum-likelihood estimates and posterior mean ± standard deviation from Metropolis–Hastings sampling (linear scale). The MLE column matches the semi-mechanistic column of Table 2.6.

Description (units)	Parameter	MLE	Posterior mean ± STD
Basal gene inactivation rate (min^{-1})	k_{off}	6.99×10^{1}	$7.77 \times 10^{1} \pm 1.96 \times 10^{1}$
Basal gene activation rate (min^{-1})	$k_{\text{on},0}$	4.06×10^{-3}	$7.00 \times 10^{-3} \pm 2.40 \times 10^{-3}$
nucGR-dependent gene activation rate (min^{-1})	$k_{\text{on},1}$	6.97×10^{-3}	$6.82 \times 10^{-3} \pm 2.79 \times 10^{-4}$
nucGR modulation of inactivation (molecules^{-1})	m_{koff}	2.25×10^{-7}	$1.24 \times 10^{-7} \pm 8.00 \times 10^{-8}$
Basal *DUSP1* transcription rate (min^{-1})	$k_{r,\text{on},0}$	8.80×10^{2}	$9.80 \times 10^{2} \pm 2.20 \times 10^{2}$
nucGR-dependent *DUSP1* transcription rate (min^{-1})	$k_{r,\text{on},1}$	4.42×10^{-7}	$8.56 \times 10^{-7} \pm 5.22 \times 10^{-7}$
DUSP1 elongation time (min)	τ_{elong}	1.76×10^{0}	$1.89 \times 10^{0} \pm 3.15 \times 10^{-1}$
DUSP1 nuclear export rate (min^{-1})	k_{Nuc2Cyt}	6.07×10^{-2}	$6.16 \times 10^{-2} \pm 2.65 \times 10^{-3}$
Basal *DUSP1* mRNA degradation rate (min^{-1})	$k_{\text{degCyt},0}$	1.58×10^{-3}	$9.30 \times 10^{-4} \pm 2.82 \times 10^{-4}$
Max TTP-dependent degradation rate (min^{-1})	$k_{\text{degCyt},1}$	3.53×10^{0}	$4.05 \times 10^{0} \pm 6.15 \times 10^{-1}$
Max fold-change in TTP-mediated degradation	TTP_1	1.02×10^{0}	$9.00 \times 10^{-1} \pm 1.16 \times 10^{-1}$
Half-max time for TTP activity (min)	t_{TTP}	6.82×10^{1}	$6.86 \times 10^{1} \pm 1.44 \times 10^{0}$
Hill coefficient, TTP time-dependence	η	2.68×10^{1}	$2.68 \times 10^{1} \pm 8.46 \times 10^{0}$
TTP–mRNA binding saturation (molecules)	k_{DTTP}	1.07×10^{2}	$1.15 \times 10^{2} \pm 1.26 \times 10^{1}$

The experiments, models, and predictions presented in this chapter constitute a complete study of acute Dex-driven GR transport and *DUSP1* mRNA regulation. As of this writing, the corresponding manuscript is in final preparation, with a preprint to be posted within the coming week and submission for peer review to follow at Nature, Science, or Cell, or one of their associated journals. The next chapter steps back from these specific findings to place them in their broader biological and methodological context, abstracts the approach into a reusable workflow, and sets out the outstanding questions and future experiments that build directly on the system characterized here.

Table 2.8: Posterior parameters for the mechanistic *DUSP1*–TTP model. Maximum-likelihood estimates and posterior mean ± standard deviation from Metropolis–Hastings sampling (linear scale). The MLE column matches the mechanistic column of Table 2.6. Symbols follow the chapter glossary; the underlying data file's symbol column was misaligned and is corrected here.

Description (units)	Parameter	MLE	Posterior mean ± STD
DUSP1 nuclear and cytoplasmic module			
Basal gene inactivation rate (min^{-1})	k_{off}	6.11×10^{-1}	$9.05 \times 10^{-1} \pm 1.96 \times 10^{-1}$
Basal gene activation rate (min^{-1})	$k_{\mathrm{on},0}$	3.55×10^{-2}	$3.67 \times 10^{-2} \pm 8.34 \times 10^{-3}$
nucGR-dependent gene activation rate (min^{-1})	$k_{\mathrm{on},1}$	3.48×10^{-3}	$4.08 \times 10^{-3} \pm 6.41 \times 10^{-4}$
nucGR modulation of inactivation ($\mathrm{molecules}^{-1}$)	m_{koff}	7.86×10^{-2}	$5.71 \times 10^{-2} \pm 2.28 \times 10^{-2}$
Basal *DUSP1* transcription rate (min^{-1})	$k_{r,\mathrm{on},0}$	6.79×10^{0}	$9.81 \times 10^{0} \pm 1.83 \times 10^{0}$
nucGR-dependent *DUSP1* transcription rate (min^{-1})	$k_{r,\mathrm{on},1}$	2.44×10^{-7}	$1.47 \times 10^{-7} \pm 5.60 \times 10^{-8}$
DUSP1 elongation time (min)	τ_{elong}	1.36×10^{0}	$1.48 \times 10^{0} \pm 3.32 \times 10^{-1}$
DUSP1 nuclear export rate (min^{-1})	k_{Nuc2Cyt}	7.12×10^{-2}	$7.25 \times 10^{-2} \pm 2.52 \times 10^{-3}$
Basal *DUSP1* mRNA degradation rate (min^{-1})	$k_{\mathrm{degCyt},0}$	5.07×10^{-4}	$8.34 \times 10^{-5} \pm 4.11 \times 10^{-5}$
Max TTP-dependent degradation rate (min^{-1})	$k_{\mathrm{degCyt},1}$	8.74×10^{-2}	$1.12 \times 10^{-1} \pm 1.71 \times 10^{-2}$
TTP module			
nucGR-dependent TTP gene activation rate (min^{-1})	$k_{\mathrm{on},1}^{\mathrm{TTP}}$	2.10×10^{-2}	$3.06 \times 10^{-2} \pm 1.84 \times 10^{-2}$
TTP gene inactivation rate (min^{-1})	$k_{\mathrm{off}}^{\mathrm{TTP}}$	2.26×10^{0}	$6.33 \times 10^{0} \pm 3.75 \times 10^{0}$
TTP transcription rate (min^{-1})	$k_{r,\mathrm{on}}^{\mathrm{TTP}}$	1.02×10^{0}	$2.23 \times 10^{0} \pm 1.06 \times 10^{0}$
TTP nuclear export rate (min^{-1})	$k_{\mathrm{Nuc2Cyt}}^{\mathrm{TTP}}$	1.17×10^{-2}	$1.26 \times 10^{-2} \pm 3.33 \times 10^{-3}$
Basal TTP mRNA degradation rate (min^{-1})	γ_0^{TTP}	2.09×10^{-3}	$2.13 \times 10^{-3} \pm 2.24 \times 10^{-3}$
TTP translation rate (min^{-1})	k_{tl}	6.65×10^{-1}	$6.05 \times 10^{-1} \pm 1.62 \times 10^{-1}$
TTP protein degradation rate (min^{-1})	γ_p	1.42×10^{0}	$3.28 \times 10^{-1} \pm 3.99 \times 10^{-1}$
TTP–mRNA binding rate ($\mathrm{min}^{-1}\ \mathrm{mol}^{-1}$)	k_b	4.21×10^{0}	$9.65 \times 10^{0} \pm 3.78 \times 10^{0}$
TTP–mRNA unbinding rate (min^{-1})	k_u	4.11×10^{-2}	$2.90 \times 10^{-2} \pm 1.26 \times 10^{-2}$
Hill coefficient, TTP–mRNA binding	η_{TTP}	7.48×10^{-2}	$3.51 \times 10^{-2} \pm 2.59 \times 10^{-2}$

Chapter 3

Synthesis, Outstanding Questions, and Future Directions

3.1 Synthesis

The central result of this dissertation is a quantitative, mechanistic, and predictive model of Dex-driven GR transport and *DUSP1* mRNA regulation in HeLa cells during the first three hours of stimulation, inferred entirely from endogenous single-cell measurements. The model identifies nuclear GR degradation as the dominant mechanism of receptor clearance, GR-dependent increases in the promoter activation rate k_{on} as the dominant driver of transcriptional induction (with negligible contribution from the transcription rate k_{r}, and a modest possible contribution from decreases in k_{off} that the current data cannot definitively resolve), and time-varying, saturable ARE-mediated decay (consistent with TTP) as the dominant mechanism of cytoplasmic mRNA clearance. With these mechanisms in place, the fully parameterized model quantitatively predicts joint nuclear and cytoplasmic mRNA distributions, transcription site activity, and dose response behavior across seven orders of magnitude of Dex concentration and across acute transcriptional inhibition with TPL, all without refitting.

These conclusions describe the acute response. Three hours is the regime in which the underlying regulatory architecture (GR translocation, promoter switching, transcription, and decay) is most cleanly identifiable, but it is not the regime that is most clinically relevant. GCs are administered chronically in asthma, COPD, and a range of autoimmune and inflammatory diseases, and the clinical limitations of long-term GC therapy (acquired resistance and side-effect accumulation) develop over days to weeks rather than the hours studied here [7, 23]. The mechanisms that dominate at three hours may not be the mechanisms that dominate at twenty-four. In particular, reported recruitment of p300 to the *DUSP1* locus [134] raises the specific possibility that sus-

tained signaling stabilizes the active promoter state through decreases in k_{off}, shifting regulation from a burst-frequency mode toward a combined burst-frequency and burst-duration mode. The acute-phase model and parameters reported here provide the quantitative baseline against which any such shift can be measured, and the workflow used to obtain them transfers directly to longer time courses (Section 3.4).

A second limitation, distinct from the acute regime discussed above, concerns the cell line itself. All experiments in this work were performed in HeLa cells, an immortalized cervical adenocarcinoma line that is aneuploid and carries a substantially rearranged genome relative to normal human cells [131]. Aberrant copy number and chromatin state at the *DUSP1* locus and across the GR and MAPK signaling machinery can shift the very quantities this framework infers, so the specific rate constants and model rankings reported in Chapter 2 should be read as properties of this cell line under these conditions, and both the inferred parameters and the favored mechanisms are expected to change across cell types as gene dosage, chromatin accessibility, and cofactor and ARE-binding-protein abundance vary. The goal of this work was not to catalog the parameters of GR–*DUSP1* regulation specific to HeLa cells, but to establish that an integrated single-cell measurement and stochastic modeling framework can resolve and predict these processes at all; testing whether the specific mechanisms generalize to non-transformed primary and disease-relevant cells is a direct and important extension (Section 3.4).

Beyond the specific biology, the broader contribution of this work is the framework itself. The combination of endogenous ICC and smiFISH measurements, stochastic models solved with the CME, and likelihood-based discrimination between alternative mechanistic hypotheses can be applied to almost any signal-activated gene regulatory system. The remainder of this chapter outlines that framework as a workflow others in the group can follow, summarizes the additional projects I contributed to during my PhD, and identifies a set of accessible next experiments and longer-term directions that build directly on the Dex-GR-*DUSP1*-TTP system.

3.2 A workflow for building predictive single-cell models of signal-activated gene regulation

The work in Chapter 2 can be abstracted into a five-step workflow. Each step has a corresponding software and experimental scaffold that already exists within the group, which should substantially lower the cost of applying it to new systems.

1. Quantify the endogenous response at the single-cell level. The starting point is fixed-cell ICC and/or smiFISH measurements of the endogenous targets of interest, with sufficient time points and stimulation conditions to constrain both means and full distributions. Endogenous measurements avoid the confounds of overexpression, reporter constructs, and integration site effects, and they provide direct access to the cell-to-cell variability that constrains stochastic models [31, 115]. The DUSP1AnalysisManager and AngelFISH pipelines developed during this work provide a reusable template for segmentation, spot detection, SNR-based filtering, and per-cell quantification.

2. Sketch a minimal mechanistic model and enumerate alternatives. Rather than building one large model, the approach taken here was to define a minimal set of species and reactions, then enumerate biologically motivated alternative hypotheses for each step (Dex modulating import versus export; degradation in one compartment versus both; GR acting through k_{on}, k_{off}, or k_r; first-order versus saturable versus time-varying decay). Enumerating alternatives up front makes it possible to discriminate between mechanisms using data, rather than committing to a single architecture based on prior assumptions.

3. Solve and fit using the SSIT. The SSIT [126] provides FSP solutions of the CME, hybrid ODE-FSP integration for upstream deterministic species, and SSA/ABC routines for cases where FSP is impractical (such as the cytoplasmic mRNA module). Likelihood-based fitting against full distributions, rather than means or summary statistics, is essential for identifying mechanisms that differ primarily in the variance structure of the data, as was the case here for the saturable ARE-mediated decay.

4. Discriminate among models using likelihood and BIC, validated by qualitative observations. Likelihood ratios and BIC differences provide quantitative ranking of competing models, but these should be cross-checked against qualitative features of the data that the chosen model must reproduce. In this work, the saturable, time-varying decay model was favored both by BIC and by the qualitative observation that cytoplasmic mRNA variability is larger than nuclear mRNA variability at late times, a feature that simpler models cannot reproduce.

5. Validate by predicting held-out conditions without refitting. The strongest test of any mechanistic model is its ability to predict the outcome of perturbations it was not fit to. In Chapter 2, predictions across 1 nM and 10 nM Dex, a seven-order-of-magnitude Dex titration, and dual Dex-TPL stimulation provided this test. Future applications of this workflow should reserve at least one perturbation or concentration as a held-out validation condition from the start.

Applied consistently, this workflow yields models that are not only descriptive but predictive, and that can be used to design follow-up experiments rather than simply rationalize existing ones.

3.3 Methodological refinements to strengthen future applications

The workflow above is general, but the specific implementation in Chapter 2 carries methodological limitations that should be addressed in any future application. Each of the refinements below was identified during this work, has a clear implementation path within the group's existing infrastructure, and would strengthen both the conclusions of Chapter 2 and the experiments proposed in Section 3.4.

Paired intronic and exonic smiFISH probe sets for transcription site quantification. The *DUSP1* smiFISH probe set used in Chapter 2 targets only exonic sequence, so transcription sites are recovered as bright nuclear clusters whose integrated intensity reports the number of nascent transcripts rather than through a dedicated nascent-RNA channel. This conflates TS signal with closely spaced mature nuclear mRNA at high expression and limits the ability to distinguish k_{on}- from k_{off}-driven changes in burst structure. A paired probe set in which intronic probes (one fluo-

rescent channel) directly label nascent transcripts and exonic probes (a second channel) label both nascent and mature mRNA would provide an unambiguous TS mask, allow direct measurement of nascent-only TS intensity, and substantially improve identifiability of k_{on} versus k_{off} in the model selection step (Step 4 of the workflow).

Joint ICC and smiFISH in the same cell. The current implementation measures nuclear GR (by ICC) and *DUSP1* mRNA (by smiFISH) in parallel samples drawn from the same conditions but not from the same cells. The model therefore fits marginal distributions of each species and infers their joint behavior through the shared upstream signal rather than from direct measurement. Sequential ICC-then-smiFISH protocols, which preserve both protein epitopes and mRNA integrity, would yield true single-cell joint distributions of GR localization and *DUSP1* transcript counts. This would tighten the constraints on the GR-to-promoter coupling, allow direct measurement of the GR-DUSP1 correlation as a function of dose and time, and enable model fits against the full joint distribution rather than its marginals.

Automated multiwell acquisition with fluorescent bead intensity standards. Throughput in this work was limited by manual acquisition on individual coverslips, and absolute intensity comparisons across imaging sessions relied on within-session controls rather than an external reference. Two changes would address both limitations. First, mounting samples in multiwell imaging slides with automated stage scanning would allow many conditions, replicates, and controls to be acquired in a single session under matched optical conditions, reducing session-to-session variability and substantially increasing the number of single cells per condition. Second, imaging fluorescent bead standards (such as TetraSpeck beads) at the start of each session in each channel provides an external intensity reference against which both spot intensities and ICC signals can be normalized across days, microscopes, and probe batches. Together these changes would convert TS intensity and ICC nuclear GR measurements from session-relative to session-absolute quantities, allowing direct comparison across experiments and across collaborating groups.

These refinements are not required to reproduce the conclusions of Chapter 2, but they would substantially reduce the uncertainty bands on the inferred parameters, sharpen the discrimination

among competing mechanistic models, and lower the experimental cost of applying the workflow to the systems proposed in the following section.

3.4 Immediate extensions and low-hanging fruit

Several experimental extensions of the Dex-GR-*DUSP1*-TTP system are now technically straightforward and would substantially strengthen or extend the conclusions of Chapter 2.

Paired intronic and exonic *DUSP1* smiFISH for TS quantification. The methodological case for paired intronic and exonic probes is given in Section 3.3. Applied to *DUSP1* across the same time courses and Dex concentrations used in Chapter 2, this measurement would replace integrated exonic intensity with a dedicated nascent-RNA TS channel. The resulting data would directly test whether *DUSP1* transcriptional induction is driven primarily by increases in burst frequency (k_{on}) or also includes meaningful contributions from extended burst duration (decreases in k_{off}), and would substantially tighten the parameter estimates and uncertainty bounds on both rates.

Extended Dex stimulation time courses. Sustained Dex stimulation beyond three hours would test the boundary between the acute regulatory architecture characterized in Chapter 2 and the chronic regime relevant to long-term GC pharmacology. smiFISH and ICC time courses extended to 24, 48, and 72 hours would specifically test whether k_{on} remains the dominant regulated rate or whether k_{off} stabilization (consistent with reported p300 recruitment to the *DUSP1* locus [134]) becomes a substantial contributor at later times. The acute-phase parameters reported in Chapter 2 provide the $t < 3\,\mathrm{h}$ initial condition for any such extended time course, and the existing TS-intensity and burst-frequency analyses transfer without modification. Combined with the paired intronic and exonic probes described above, these experiments would also directly resolve whether the dominant regulated rate changes with prolonged stimulation.

Testing additional glucocorticoid ligands. Dexamethasone was used throughout Chapter 2 as a high-affinity, well-characterized reference ligand, but the clinical landscape of GC therapy includes lower-affinity natural and synthetic GCs (e.g., prednisolone, the active metabolite of

prednisone) and the developing class of selective glucocorticoid receptor agonists and modulators (SEGRAMs) designed to dissociate transactivation from transrepression for improved side-effect profiles [50]. Repeating the core time-course and dose-response measurements with these ligands would test whether the inferred GR transport and *DUSP1* regulatory parameters scale predictably with ligand affinity or whether ligand-specific effects (altered nuclear retention, phosphorylation status, or cofactor recruitment) emerge. This extension converts the model from a Dex-specific description into a quantitative platform for comparing ligands directly relevant to clinical GC pharmacology.

Direct measurement of TTP. The mechanistic TTP network proposed in Chapter 2 is currently inferred indirectly through its effects on *DUSP1* mRNA distributions. Direct ICC measurements of TTP protein across the same Dex stimulation conditions would test the model's predictions for the regulatory circuit (Figure 2.1a) and provide independent constraints on the TTP module parameters in Table 2.6.

smiFISH for *TTP* and other early-response GC-induced genes. smiFISH against *TTP* mRNA would directly test the inferred dynamics of the TTP transcriptional response and provide a second ARE-containing transcript whose decay can be modeled in parallel with *DUSP1*. Additional early-response GC-induced genes (*GILZ*, *NFKBIA*, and others) would test the generality of the GR-dependent burst frequency mechanism inferred for *DUSP1* and would allow direct comparison of promoter responses to the same upstream GR signal.

Testing the model in medically relevant cell types. HeLa cells provided a clean and well-characterized testbed, but the clinical relevance of the Dex-GR-*DUSP1*-TTP axis lies in airway epithelial and immune contexts [7, 23, 37]. Repeating the core ICC and smiFISH measurements in BEAS-2B, A549, or primary airway epithelial cells would test whether the inferred mechanisms and parameters generalize, or whether cell-type-specific chromatin and signaling context produces quantitatively different regulatory architectures [91].

Live-cell measurement of MKP1 translation and *DUSP1* mRNA decay. The current model is parameterized entirely from fixed-cell measurements and therefore provides a time-averaged de-

scription of translation and degradation rather than direct observation of individual events. Two complementary live-cell single-molecule techniques would resolve these processes at the resolution at which they occur. Nascent chain tracking (NCT) [142, 143] uses fluorescently labeled antibody fragments that bind nascent epitope tags on the growing polypeptide, allowing translation to be imaged in real time on individual mRNAs. The TREAT system [144] uses a dual-color stem-loop architecture in which intact transcripts display both colors while degradation intermediates retain only the 3′-stabilized end, allowing individual mRNA decay events to be localized in space and time. Both labels can be combined within a single *DUSP1* reporter that preserves the 3′ UTR ARE, enabling simultaneous measurement of nascent MKP1 translation and *DUSP1* mRNA decay on the same molecule. This would directly test whether ARE-mediated degradation is coupled to translation status, provide per-event rate constants that convert the current time-varying cytoplasmic decay function from a phenomenological fit into a mechanistically anchored rate law, and measure MKP1 protein production dynamics that the present mRNA-only model cannot access. The infrastructure for NCT-based imaging is established within the group through prior shared-author work [143], and the same construct design would extend the multiplexed NCT framework developed there into a regulated, signal-responsive system.

3.5 Additional contributions during this PhD

Beyond the work presented in Chapter 2, three additional efforts during this PhD contributed to the broader research and training activities of the group.

Shared-author work on multiplexed nascent chain tracking. I contributed to Raymond et al. (2023) [143], which combines stochastic mechanistic simulation with machine learning to design single-color multiplexed NCT experiments and demonstrates that, in principle, as many as seven mRNA species can be distinguished within a single cell using only two fluorescent tags. My contribution was experimental validation of the multiplexed NCT approach, including plasmid preparation, bead-loading of cells with fluorescent labeling reagents, and live-cell microscopy. Additional validation experiments were performed that were not included in the published manuscript.

Teaching at the q-bio summer school. I served as a lecturer at the q-bio summer school, where I delivered a lecture on fluorescence techniques used in single-cell experimentation and led both fixed-cell and live-cell microscopy demonstrations on a HiLo microscope. The course material drew directly on the experimental and analytical methods developed during this dissertation.

Undergraduate mentoring and protocol development. I trained multiple undergraduate students in mammalian cell culture, fixed-cell experimentation (ICC, smiFISH), and live-cell experimentation (NCT), and authored standard operating procedures for each fixed-cell technique that are now used as training and reference documents within the lab.

Bibliography

[1] David Furman, Judith Campisi, Eric Verdin, Pedro Carrera-Bastos, Sasha Targ, Claudio Franceschi, Luigi Ferrucci, Derek W. Gilroy, Alessio Fasano, Gary W. Miller, Andrew H. Miller, Alberto Mantovani, Cornelia M. Weyand, Nir Barzilai, Jorg J. Goronzy, Thomas A. Rando, Rita B. Effros, Alejandro Lucia, Nicole Kleinstreuer, and George M. Slavich. Chronic inflammation in the etiology of disease across the life span. *Nature Medicine*, 25(12):1822–1832, December 2019.

[2] C. Nathan and A. Ding. Nonresolving inflammation. *Cell*, 140:871–882, 2010.

[3] H.B. Fleit. Chronic Inflammation. In *Pathobiology of Human Disease*, pages 300–314. Elsevier, 2014.

[4] Roma Pahwa, Amandeep Goyal, and Ishwarlal Jialal. Chronic Inflammation. *Pathobiology of Human Disease: A Dynamic Encyclopedia of Disease Mechanisms*, pages 300–314, August 2023. ISBN: 9780123864567.

[5] P.J. Barnes. Glucocorticosteroids: current and future directions. *Br. J. Pharmacol*, 163:29–43, 2011.

[6] Lukasz S. Wylezinski, Jamieson D. Gray, Julia B. Polk, Andrew J. Harmata, and Charles F. Spurlock. Illuminating an Invisible Epidemic: A Systemic Review of the Clinical and Economic Benefits of Early Diagnosis and Treatment in Inflammatory Disease and Related Syndromes. *Journal of Clinical Medicine*, 8(4):493, April 2019.

[7] Robert Newton, Suharsh Shah, Mohammed O. Altonsy, and Antony N. Gerber. Glucocorticoid and cytokine crosstalk: Feedback, feedforward, and co-regulatory interactions determine repression or resistance. *Journal of Biological Chemistry*, 292(17):7163–7172, April 2017.

[8] Mariana Cifuentes, Hugo E. Verdejo, Pablo F. Castro, Alejandro H. Corvalan, Catterina Ferreccio, Andrew F. G. Quest, Marcelo J. Kogan, and Sergio Lavandero. Low-Grade Chronic Inflammation: a Shared Mechanism for Chronic Diseases. *Physiology*, 40(1):4–25, January 2025.

[9] Karen T. Feehan and Derek W. Gilroy. Is Resolution the End of Inflammation? *Trends in Molecular Medicine*, 25(3):198–214, March 2019.

[10] Stefanie Luecke, Katherine M. Sheu, and Alexander Hoffmann. Stimulus-specific responses in innate immunity: Multilayered regulatory circuits. *Immunity*, 54(9):1915–1932, September 2021.

[11] Maya E. Kotas and Ruslan Medzhitov. Homeostasis, Inflammation, and Disease Susceptibility. *Cell*, 160(5):816–827, February 2015.

[12] Andrew R. Clark and Jonathan L.E. Dean. The control of inflammation via the phosphorylation and dephosphorylation of tristetraprolin: a tale of two phosphatases. *Biochemical Society Transactions*, 44(5):1321–1337, October 2016.

[13] Jeremy C. Burton, William Antoniades, Jennifer Okalova, Morgan M. Roos, and Neil J. Grimsey. Atypical p38 Signaling, Activation, and Implications for Disease. *International Journal of Molecular Sciences 2021, Vol. 22, Page 4183*, 22(8):4183, April 2021.

[14] Jiahuai Han, Jianfeng Wu, and John Silke. An overview of mammalian p38 mitogen-activated protein kinases, central regulators of cell stress and receptor signaling. *F1000Research*, 9:653, June 2020.

[15] Jiahui Wang, Yongjian Liu, Yushi Guo, Cen Liu, Yuping Yang, Xiaoxiao Fan, Hongliu Yang, Yonggang Liu, and Tao Ma. Function and inhibition of P38 MAP kinase signaling: Targeting multiple inflammation diseases. *Biochemical Pharmacology*, 220:115973, February 2024.

[16] Alexander Plotnikov, Eldar Zehorai, Shiri Procaccia, and Rony Seger. The MAPK cascades: Signaling components, nuclear roles and mechanisms of nuclear translocation. *Biochimica et Biophysica Acta - Molecular Cell Research*, 1813(9):1619–1633, September 2011.

[17] Corrado Pelaia, Alessandro Vatrella, Angela Sciacqua, Rosa Terracciano, and Girolamo Pelaia. Role of p38-mitogen-activated protein kinase in COPD: pathobiological implications and therapeutic perspectives. *Expert Review of Respiratory Medicine*, 14(5):485–491, May 2020.

[18] Corrado Pelaia, Alessandro Vatrella, Luca Gallelli, Nicola Lombardo, Angela Sciacqua, Rocco Savino, and Girolamo Pelaia. Role of p38 mitogen-activated protein kinase in asthma and COPD: Pathogenic aspects and potential targeted therapies. *Drug Design, Development and Therapy*, 15:1275–1284, 2021.

[19] Galia Maik-Rachline, Elder Zehorai, Tamar Hanoch, John Blenis, and Rony Seger. The nuclear translocation of the kinases p38 and JNK promotes inflammation-induced cancer. *Science Signaling*, 11(525), April 2018.

[20] Galia Maik-Rachline, Lucia Lifshits, and Rony Seger. Nuclear P38: Roles in Physiological and Pathological Processes and Regulation of Nuclear Translocation. *International Journal of Molecular Sciences 2020, Vol. 21, Page 6102*, 21(17):6102, August 2020.

[21] Adrián Martínez-Limón, Manel Joaquin, María Caballero, Francesc Posas, and Eulàlia de Nadal. The p38 pathway: From biology to cancer therapy. *International Journal of Molecular Sciences*, 21(6), March 2020.

[22] Ying Liao, Xiaoxing Wang, Mei Huang, James P. Tam, and Ding Xiang Liu. Regulation of the p38 mitogen-activated protein kinase and dual-specificity phosphatase 1 feedback loop modulates the induction of interleukin 6 and 8 in cells infected with coronavirus infectious bronchitis virus. *Virology*, 420(2):106–116, November 2011.

[23] Jessica Hoppstädter and Alaina J. Ammit. Role of dual-specificity phosphatase 1 in glucocorticoid-driven antiinflammatory responses. *Frontiers in Immunology*, 10(JUN), 2019.

[24] Christopher J. Caunt and Stephen M. Keyse. Dual-specificity MAP kinase phosphatases (MKPs): Shaping the outcome of MAP kinase signalling. *FEBS Journal*, 280(2):489–504, January 2013.

[25] Fuwei Yang, Li-Jie Zhao, Qinli Xu, and Jianhui Zhao. The journey of p38 MAP kinase inhibitors: From bench to bedside in treating inflammatory diseases. *European Journal of Medicinal Chemistry*, 280:116950, December 2024.

[26] Gianfranco Umberto Meduri, Djillali Annane, Marco Confalonieri, George P. Chrousos, Bram Rochwerg, Amanda Busby, Barbara Ruaro, and Bernd Meibohm. Pharmacological principles guiding prolonged glucocorticoid treatment in ARDS. *Intensive Care Medicine*, 46(12):2284–2296, 2020.

[27] Sean G. Kirk, Lobelia Samavati, and Yusen Liu. MAP kinase phosphatase-1, a gatekeeper of the acute innate immune response. *Life sciences*, 241:117157, January 2020.

[28] SM Abraham and AR Clark. Dual-specificity phosphatase 1: a critical regulator of innate immune responses. *Biochem Soc Trans*, 34, 2006.

[29] Andrew R. Clark. Anti-inflammatory functions of glucocorticoid-induced genes. *Molecular and Cellular Endocrinology*, 275(1-2):79–97, September 2007.

[30] J. D. O'Neil, A. J. Ammit, and A. R. Clark. MAPK p38 regulates inflammatory gene expression via tristetraprolin: Doing good by stealth. *International Journal of Biochemistry and Cell Biology*, 94:6–9, January 2018.

[31] Brian Munsky, Gregor Neuert, and Alexander van Oudenaarden. Using gene expression noise to understand gene regulation. *Science*, 336(6078):183–187, April 2012.

[32] Brian Munsky, Zachary Fox, and Gregor Neuert. Integrating single-molecule experiments and discrete stochastic models to understand heterogeneous gene transcription dynamics. *Methods*, 85:12–21, September 2015.

[33] SM Abraham, T Lawrence, A Kleiman, P Warden, and M Medghalchi. Antiinflammatory effects of dexamethasone are partly dependent on induction of dual specificity phosphatase 1. *J Exp Med*, 203, 2006.

[34] Pavan Prabhala, Kristin Bunge, Qi Ge, and Alaina J. Ammit. Corticosteroid-Induced MKP-1 Represses Pro-Inflammatory Cytokine Secretion by Enhancing Activity of Tristetraprolin (TTP) in ASM Cells. *Journal of Cellular Physiology*, 231(10):2153–2158, 2016. _eprint: https://onlinelibrary.wiley.com/doi/pdf/10.1002/jcp.25327.

[35] Christopher Tiedje, Manuel D. Diaz-Muñoz, Philipp Trulley, Helena Ahlfors, Kathrin Laaß, Perry J. Blackshear, Martin Turner, and Matthias Gaestel. The RNA-binding protein TTP is a global post-transcriptional regulator of feedback control in inflammation. *Nucleic Acids Research*, 44(15):7418–7440, September 2016.

[36] Suharsh Shah, Elizabeth M. King, Ambika Chandrasekhar, and Robert Newton. Roles for the mitogen-Activated protein kinase (MAPK) phosphatase, DUSP1, in feedback control of inflammatory gene expression and repression by dexamethasone. *Journal of Biological Chemistry*, 289(19):13667–13679, 2014.

[37] Zeyad Muazzen, Walid Moghrabi, Tala Bakheet, Linah Mahmoud, Maher Al-Saif, Khalid S. A. Khabar, and Edward G. Hitti. Global analysis of the abundance of AU-rich mRNAs in response to glucocorticoid treatment. *Scientific Reports*, 14(1), January 2024.

[38] Marina Lasa, Sonya M. Abraham, Christine Boucheron, Jeremy Saklatvala, and Andrew R. Clark. Dexamethasone Causes Sustained Expression of Mitogen-Activated Protein Kinase (MAPK) Phosphatase 1 and Phosphatase-Mediated Inhibition of MAPK p38. *Molecular and Cellular Biology*, 22(22):7802–7811, November 2002.

[39] Katinka Albrecht, Johanna Callhoff, Matthias Schneider, and Angela Zink. High variability in glucocorticoid starting doses in patients with rheumatoid arthritis: observational data from an early arthritis cohort. *Rheumatology International*, 35(8):1377–1384, August 2015.

[40] Yuanrui Zhao, Zhun Yao, Song Xu, Lan Yao, and Zhui Yu. Glucocorticoid therapy for acute respiratory distress syndrome: Current concepts. *Journal of Intensive Medicine*, 2024.

[41] Ian S. deSouza, Nicole Anthony, Henry Thode, Robert Allen, Jane Belyavskaya, Jessica Koos, and Adam Singer. Effectiveness and Safety of Pharmacologic Therapies for Migraine in the Emergency Department: A Systematic Review and Bayesian Network Meta-analysis. *Annals of Emergency Medicine*, 85(4):313–329, April 2025.

[42] Nida Qadir, Sarina Sahetya, Laveena Munshi, Charlotte Summers, Darryl Abrams, Jeremy Beitler, Giacomo Bellani, Roy G. Brower, Lisa Burry, Jen-Ting Chen, Carol Hodgson, Catherine L. Hough, Francois Lamontagne, Anica Law, Laurent Papazian, Tai Pham, Eileen Rubin, Matthew Siuba, Irene Telias, Setu Patolia, Dipayan Chaudhuri, Allan Walkey, Bram Rochwerg, and Eddy Fan. An Update on Management of Adult Patients with Acute Respiratory Distress Syndrome: An Official American Thoracic Society Clinical Practice Guideline. *American Journal of Respiratory and Critical Care Medicine*, 209(1):24–36, January 2024.

[43] The RECOVERY Collaborative Group. Dexamethasone in Hospitalized Patients with Covid-19. *New England Journal of Medicine*, 384(8):693–704, February 2021.

[44] Chang Kon Kim. Glucocorticoid Insensitivity in Severe Asthma: Underlying Molecular Mechanisms, Challenges, and Emerging Therapies. *Archives of Internal Medicine Research*, 8(2), 2025.

[45] Peter J. Barnes and Ian M. Adcock. Glucocorticoid resistance in inflammatory diseases. *The Lancet*, 373(9678):1905–1917, 2009.

[46] Heike Schäcke, Wolf Dietrich Döcke, and Khusru Asadullah. Mechanisms involved in the side effects of glucocorticoids. *Pharmacology & Therapeutics*, 96(1):23–43, October 2002.

[47] Sabine Vettorazzi, Denis Nalbantoglu, J. Christof M. Gebhardt, and Jan Tuckermann. A guide to changing paradigms of glucocorticoid receptor function—a model system for genome regulation and physiology. *The FEBS Journal*, 289(19):5718–5743, October 2022.

[48] Sofie Vandevyver, Lien Dejager, and Claude Libert. Comprehensive overview of the structure and regulation of the glucocorticoid receptor. *Endocrine Reviews*, 35(4):671–693, August 2014.

[49] Steven Timmermans, Jolien Souffriau, and Claude Libert. A general introduction to glucocorticoid biology. *Frontiers in Immunology*, 10(JULY), 2019.

[50] Ekaterina A. Lesovaya, Daria Chudakova, Gleb Baida, Ekaterina M. Zhidkova, Kirill I. Kirsanov, Marianna G. Yakubovskaya, and Irina V. Budunova. The long winding road to the safer glucocorticoid receptor (GR) targeting therapies. *Oncotarget*, 13(1):408, 2022.

[51] Emyr Bakker, Kun Tian, Luciano Mutti, Constantinos Demonacos, Jean-Marc Schwartz, and Marija Krstic-Demonacos. Insight into glucocorticoid receptor signalling through interactome model analysis. *PLOS Computational Biology*, 13(11):e1005825, November 2017.

[52] Christoph Kleinschnitz, ; Kinga Blecharz, Timo Kahles, Tobias Schwarz, ; Peter Kraft, Kerstin Göbel, Sven G Meuth, Malgorzata Burek, Thomas Thum, Guido Stoll, and Carola Förster. Acquired Glucocorticoid Resistance Due to Homologous Glucocorticoid Receptor Downregulation: A Modern Look at an Age-Old Problem. *Cells 2021, Vol. 10, Page 2529*, 10(10):2529, September 2021.

[53] Jack Lockett, Warrick J Inder, and Vicki L Clifton. The Glucocorticoid Receptor: Isoforms, Functions, and Contribution to Glucocorticoid Sensitivity. *Endocrine Reviews*, 45(4):593–624, August 2024.

[54] Lisa M. Sevilla, Alba Jiménez-Panizo, Andrea Alegre-Martí, Eva Estébanez-Perpiñá, Carme Caelles, and Paloma Pérez. Glucocorticoid Resistance: Interference between the Glucocorticoid Receptor and the MAPK Signalling Pathways. *International Journal of Molecular Sciences 2021, Vol. 22, Page 10049*, 22(18):10049, September 2021.

[55] Diana A. Stavreva, David A. Garcia, Gregory Fettweis, Prabhakar R. Gudla, George F. Zaki, Vikas Soni, Andrew McGowan, Geneva Williams, Anh Huynh, Murali Palangat, R. Louis Schiltz, Thomas A. Johnson, Diego M. Presman, Matthew L. Ferguson, Gianluca Pegoraro, Arpita Upadhyaya, and Gordon L. Hager. Transcriptional Bursting and Co-bursting Regulation by Steroid Hormone Release Pattern and Transcription Factor Mobility. *Molecular cell*, 75(6):1161–1177.e11, September 2019.

[56] Steven Robertson, Janet P. Hapgood, and Ann Louw. Glucocorticoid receptor concentration and the ability to dimerize influence nuclear translocation and distribution. *Steroids*, 78(2):182–194, February 2013.

[57] Gal Haimovich and Jeffrey E. Gerst. Single-molecule Fluorescence in situ Hybridization (smFISH) for RNA Detection in Adherent Animal Cells. *Bio-protocol*, 8(21):e3070, November 2018.

[58] Jonathan Rosen and Jeffrey N. Miner. The search for safer glucocorticoid receptor ligands. *Endocrine Reviews*, 26(3):452–464, May 2005.

[59] Federico Monczor, Antonia Chatzopoulou, Carlos Daniel Zappia, René Houtman, Onno C. Meijer, and Carlos P. Fitzsimons. A Model of Glucocorticoid Receptor Interaction With Coregulators Predicts Transcriptional Regulation of Target Genes. *Frontiers in Pharmacology*, 10, March 2019.

[60] Laura Van Moortel, Jonathan Thommis, Brecht Maertens, An Staes, Dorien Clarisse, Delphine De Sutter, Claude Libert, Onno C. Meijer, Sven Eyckerman, Kris Gevaert, and Karolien De Bosscher. Novel assays monitoring direct glucocorticoid receptor protein

activity exhibit high predictive power for ligand activity on endogenous gene targets. *Biomedicine & Pharmacotherapy*, 152:113218, August 2022.

[61] Mahita Kadmiel and John A. Cidlowski. Glucocorticoid receptor signaling in health and disease. *Trends in Pharmacological Sciences*, 34(9):518–530, September 2013.

[62] Sivapriya Ramamoorthy and John A. Cidlowski. Corticosteroids. Mechanisms of Action in Health and Disease. *Rheumatic Disease Clinics of North America*, 42(1):15–31, 2016.

[63] D Raddatz, M Henneken, T Armbrust, and G Ramadori. Subcellular distribution of glucocorticoid receptor in cultured rat and human liver-derived cells and cell lines: Influence of dexamethasone. *Hepatology*, 24(4):928–933, 1996. _eprint: https://onlinelibrary.wiley.com/doi/pdf/10.1002/hep.510240429.

[64] Sofie Vandevyver, Lien Dejager, and Claude Libert. On the Trail of the Glucocorticoid Receptor: Into the Nucleus and Back. *Traffic*, 13(3):364–374, March 2012.

[65] Martin Stortz, Diego M. Presman, Luciana Bruno, Paolo Annibale, Maria V. Dansey, Gerardo Burton, Enrico Gratton, Adali Pecci, and Valeria Levi. Mapping the Dynamics of the Glucocorticoid Receptor within the Nuclear Landscape. *Scientific Reports 2017 7:1*, 7(1):1–14, July 2017.

[66] David A Garcia, Gregory Fettweis, Diego M Presman, Ville Paakinaho, Christopher Jarzynski, Arpita Upadhyaya, and Gordon L Hager. Power-law behavior of transcription factor dynamics at the single-molecule level implies a continuum affinity model. *Nucleic Acids Research*, 49(12):6605–6620, February 2021.

[67] Timothy J. Stasevich and James G. McNally. Assembly of the transcription machinery: Ordered and stable, random and dynamic, or both? *Chromosoma*, 120(6):533–545, December 2011.

[68] Christy J. Fryer and Trevor K. Archer. Chromatin remodelling by the glucocorticoid receptor requires the BRG1 complex. *Nature*, 393(6680):88–91, May 1998.

[69] Andrew D. Wallace and John A. Cidlowski. Proteasome-mediated Glucocorticoid Receptor Degradation Restricts Transcriptional Signaling by Glucocorticoids. *Journal of Biological Chemistry*, 276(46):42714–42721, November 2001.

[70] Aishwarya Iyer-Bierhoff, Martin Wieczorek, Sina Marielle Peter, Dima Ward, Martin Bens, Sabine Vettorazzi, Karl-Heinz Guehrs, Jan P. Tuckermann, and Thorsten Heinzel. Acetylation-induced proteasomal degradation of the activated glucocorticoid receptor limits hormonal signaling. *iScience*, 27(2):108943, 2024.

[71] Guang Chen, Shidong Lv, Laura E. Pascal, and Zhou Wang. Regulation of glucocorticoid receptor nuclear localization in prostate cancer cells. *The Journal of Pharmacology and Experimental Therapeutics*, 392(5):103577, May 2025.

[72] Robert H. Oakley, Jeffrey C. Webster, Madhabananda Sar, C. Richard Parker, Jr., and John A. Cidlowski. Expression and Subcellular Distribution of the β-Isoform of the Human Glucocorticoid Receptor*. *Endocrinology*, 138(11):5028–5038, November 1997.

[73] Minna E. Kubin, Päivi M. Hägg, Nina Kokkonen, Juha P. Väyrynen, Kirsi-Maria Haapasaari, Jyri Moilanen, Matti Kallioinen, Tiina Hurskainen, and Kaisa Tasanen. Glucocorticoid receptors GRα and GRβ are expressed in inflammatory dermatoses. *European journal of dermatology: EJD*, 26(1):21–27, 2016.

[74] Md. Mojahidur Hasan and Sehreen Tory. Association between glucocorticoid receptor beta and steroid resistance: A systematic review. *Immunity, Inflammation and Disease*, 12(1):e1137, 2024. _eprint: https://onlinelibrary.wiley.com/doi/pdf/10.1002/iid3.1137.

[75] Emily R. Weikum, Matthew T. Knuesel, Eric A. Ortlund, and Keith R. Yamamoto. Glucocorticoid receptor control of transcription: precision and plasticity via allostery. *Nature Reviews Molecular Cell Biology*, 18(3):159–174, March 2017.

[76] David A. Garcia, Thomas A. Johnson, Diego M. Presman, Gregory Fettweis, Kaustubh Wagh, Lorenzo Rinaldi, Diana A. Stavreva, Ville Paakinaho, Rikke A.M. Jensen, Susanne

Mandrup, Arpita Upadhyaya, and Gordon L. Hager. An intrinsically disordered region-mediated confinement state contributes to the dynamics and function of transcription factors. *Molecular cell*, 81(7):1484–1498.e6, April 2021.

[77] Zhen Wang, Weiwei Chen, Evelyn Kono, Thoa Dang, and Michael J. Garabedian. Modulation of Glucocorticoid Receptor Phosphorylation and Transcriptional Activity by a C-Terminal-Associated Protein Phosphatase. *Molecular Endocrinology*, 21(3):625–634, March 2007.

[78] Andrew D. Wallace, Yan Cao, Sindhu Chandramouleeswaran, and John A. Cidlowski. Lysine 419 Targets Human Glucocorticoid Receptor for Proteasomal Degradation. *Steroids*, 75(12):1016–1023, December 2010.

[79] Zhen Wang, Jeremy Frederick, and Michael J. Garabedian. Deciphering the Phosphorylation "Code" of the Glucocorticoid Receptor in Vivo. *Journal of Biological Chemistry*, 277(29):26573–26580, July 2002.

[80] Yoshitoshi Kasuya, Pier Lorenzo Puri, Lisa Zeyen, Ole Morten Seternes, and Ingvild Mikkola. Crosstalk between p38 MAPK and GR Signaling. *International Journal of Molecular Sciences 2022, Vol. 23, Page 3322*, 23(6):3322, March 2022.

[81] Amy J. Galliher-Beckley and John A. Cidlowski. Emerging roles of glucocorticoid receptor phosphorylation in modulating glucocorticoid hormone action in health and disease. *IUBMB Life*, 61(10):979–986, October 2009.

[82] Kazuhiro Ito, Satoshi Yamamura, Sarah Essilfie-Quaye, Borja Cosio, Misako Ito, Peter J. Barnes, and Ian M. Adcock. Histone deacetylase 2–mediated deacetylation of the glucocorticoid receptor enables NF-κB suppression. *The Journal of Experimental Medicine*, 203(1):7, January 2006.

[83] Robert J. G. Haché, Raymond Tse, Terry Reich, Joanne G. A. Savory, and Yvonne A. Lefebvre. Nucleocytoplasmic Trafficking of Steroid-free Glucocorticoid Receptor *. *Journal of Biological Chemistry*, 274(3):1432–1439, January 1999.

[84] M. Itoh, M. Adachi, H. Yasui, M. Takekawa, H. Tanaka, and K. Imai. Nuclear export of glucocorticoid receptor is enhanced by c-Jun N-terminal kinase-mediated phosphorylation. *Molecular Endocrinology*, 16(10):2382–2392, October 2002.

[85] Naima Ismaili and Michael J. Garabedian. Modulation of glucocorticoid receptor function via phosphorylation. *Annals of the New York Academy of Sciences*, 1024:86–101, 2004.

[86] Diana A. Stavreva, Waltraud G. Müller, Gordon L. Hager, Carolyn L. Smith, and James G. McNally. Rapid Glucocorticoid Receptor Exchange at a Promoter Is Coupled to Transcription and Regulated by Chaperones and Proteasomes. *Molecular and Cellular Biology*, 24(7):2682–2697, April 2004.

[87] Kaustubh Wagh, Diana A. Stavreva, Arpita Upadhyaya, and Gordon L. Hager. Transcription Factor Dynamics: One Molecule at a Time. *Annual Review of Cell and Developmental Biology*, 39(Volume 39, 2023):277–305, October 2023.

[88] Steven Robertson, Johann M. Rohwer, Janet P. Hapgood, and Ann Louw. Impact of Glucocorticoid Receptor Density on Ligand-Independent Dimerization, Cooperative Ligand-Binding and Basal Priming of Transactivation: A Cell Culture Model. *PLOS ONE*, 8(5):e64831, May 2013.

[89] Laura Escoter-Torres, Franziska Greulich, Fabiana Quagliarini, Michael Wierer, and Nina Henriette Uhlenhaut. Anti-inflammatory functions of the glucocorticoid receptor require DNA binding. *Nucleic Acids Research*, 48(15):8393–8407, September 2020.

[90] Akhilesh K Nagaich, Dawn A Walker, Ron Wolford, and Gordon L Hager. Rapid Periodic Binding and Displacement of the Glucocorticoid Receptor during Chromatin Remodeling. *Molecular Cell*, 14(2):163–174, April 2004.

[91] Sam John, Peter J Sabo, Robert E Thurman, Myong-Hee Sung, Simon C Biddie, Thomas A Johnson, Gordon L Hager, and John A Stamatoyannopoulos. Chromatin accessibility pre-determines glucocorticoid receptor binding patterns. *Nature Genetics*, 43(3):264–268, March 2011.

[92] Arjun Raj, Charles S. Peskin, Daniel Tranchina, Diana Y. Vargas, and Sanjay Tyagi. Stochastic mRNA synthesis in mammalian cells. *PLoS Biology*, 4(10):1707–1719, 2006.

[93] Bonnie J. Deroo, Claudia Rentsch, Sowmini Sampath, Janel Young, Donald B. DeFranco, and Trevor K. Archer. Proteasomal Inhibition Enhances Glucocorticoid Receptor Transactivation and Alters Its Subnuclear Trafficking. *Molecular and Cellular Biology*, 22(12):4113–4123, June 2002.

[94] Roland Lang, Michael Hammer, and Jörg Mages. DUSP Meet Immunology: Dual Specificity MAPK Phosphatases in Control of the Inflammatory Response. *The Journal of Immunology*, 177(11):7497–7504, December 2006.

[95] Roland Lang and Faizal A.M. Raffi. Dual-specificity phosphatases in immunity and infection: An update. *International Journal of Molecular Sciences*, 20(11), June 2019.

[96] Ana Cuenda and Simon Rousseau. p38 MAP-Kinases pathway regulation, function and role in human diseases. *Biochimica et Biophysica Acta (BBA) - Molecular Cell Research*, 1773(8):1358–1375, August 2007.

[97] J. Simon C. Arthur and Steven C. Ley. Mitogen-activated protein kinases in innate immunity. *Nature Reviews Immunology*, 13(9):679–692, August 2013.

[98] National Center for Biotechnology Information. DUSP1 dual specificity phosphatase 1 [Homo sapiens] (Gene ID: 1843).

[99] Rajesh Gumpena, George T. Lountos, Sreejith Raran-Kurussi, Joseph E. Tropea, Scott Cherry, and David S. Waugh. Crystal structure of the human dual specificity phosphatase 1 catalytic domain. *Protein Science*, 27(2):561–567, February 2018.

[100] Yuki Kuwano, Hyeon Ho Kim, Kotb Abdelmohsen, Rudolf Pullmann, Jennifer L. Martindale, Xiaoling Yang, and Myriam Gorospe. MKP-1 mRNA Stabilization and Translational Control by RNA-Binding Proteins HuR and NF90. *Molecular and Cellular Biology*, 28(14):4562–4575, July 2008.

[101] R Furst, T Schroeder, HM Eilken, MF Bubik, and AK Kiemer. MAPK phosphatase-1 represents a novel anti-inflammatory target of glucocorticoids in the human endothelium. *Faseb J*, 21, 2007.

[102] Daniel Hebenstreit and Pradip Karmakar. Transcriptional bursting: from fundamentals to novel insights. *Biochemical Society Transactions*, 52(4):1695–1702, August 2024.

[103] Adrien Senecal, Brian Munsky, Florence Proux, Nathalie Ly, Floriane E. Braye, Christophe Zimmer, Florian Mueller, and Xavier Darzacq. Transcription factors modulate c-Fos transcriptional bursts. *Cell Reports*, 8(1):75–83, July 2014.

[104] Khalid S.A. Khabar. Post-transcriptional control during chronic inflammation and cancer: A focus on AU-rich elements. *Cellular and Molecular Life Sciences*, 67(17):2937–2955, May 2010.

[105] Seth A. Brooks and Perry J. Blackshear. Tristetraprolin (TTP): Interactions with mRNA and proteins, and current thoughts on mechanisms of action. *Biochimica et Biophysica Acta (BBA) - Gene Regulatory Mechanisms*, 1829(6-7):666–679, June 2013.

[106] Georg Stoecklin, Tiffany Stubbs, Nancy Kedersha, Stephen Wax, William FC Rigby, T. Keith Blackwell, and Paul Anderson. MK2-induced tristetraprolin:14-3-3 complexes prevent stress granule association and ARE-mRNA decay. *The EMBO Journal*, 23(6):1313–1324, March 2004.

[107] Franz Kratochvill, Christian Machacek, Claus Vogl, Florian Ebner, Vitaly Sedlyarov, Andreas R Gruber, Harald Hartweger, Raimund Vielnascher, Marina Karaghiosoff, Thomas

Rülicke, Mathias Müller, Ivo Hofacker, Roland Lang, and Pavel Kovarik. Tristetraprolin-driven regulatory circuit controls quality and timing of mRNA decay in inflammation. *Molecular Systems Biology*, 7(1):560, January 2011.

[108] Suharsh Shah, Elizabeth M. King, Mahmoud M. Mostafa, Mohammed O. Altonsy, and Robert Newton. DUSP1 maintains IRF1 and leads to increased expression of IRF1-dependent genes: A mechanism promoting glucocorticoid insensitivity. *Journal of Biological Chemistry*, 291(41):21802–21816, October 2016.

[109] Simon Lea, Jian Li, Jonathan Plumb, Kate Gaffey, Sarah Mason, Rosie Gaskell, Chris Harbron, and Dave Singh. P38 MAPK and glucocorticoid receptor crosstalk in bronchial epithelial cells. *Journal of Molecular Medicine*, 98(3):361–374, March 2020.

[110] Swati Goel, Fatemeh Saheb Sharif-Askari, Narjes Saheb Sharif Askari, Bushra Madkhana, Ahmad Munzer Alwaa, Bassam Mahboub, Adel M. Zakeri, Elaref Ratemi, Rifat Hamoudi, Qutayba Hamid, and Rabih Halwani. SARS-CoV-2 Switches 'on' MAPK and NFκB Signaling via the Reduction of Nuclear DUSP1 and DUSP5 Expression. *Frontiers in Pharmacology*, 12:631879, April 2021.

[111] Laura Matthews, James Johnson, Andrew Berry, Peter Trebble, Ann Cookson, Dave Spiller, Caroline Rivers, Michael Norman, Mike White, and David Ray. Cell Cycle Phase Regulates Glucocorticoid Receptor Function. *PLOS ONE*, 6(7):e22289, July 2011.

[112] Peter S. Swain, Michael B. Elowitz, and Eric D. Siggia. Intrinsic and extrinsic contributions to stochasticity in gene expression. *Proceedings of the National Academy of Sciences of the United States of America*, 99(20):12795–12800, October 2002.

[113] Joseph Rodriguez, Gang Ren, Christopher R. Day, Keji Zhao, Carson C. Chow, and Daniel R. Larson. Intrinsic Dynamics of a Human Gene Reveal the Basis of Expression Heterogeneity. *Cell*, 176(1-2):213–226.e18, January 2019.

[114] Junyue Cao, Darren A. Cusanovich, Vijay Ramani, Delasa Aghamirzaie, Hannah A. Pliner, Andrew J. Hill, Riza M. Daza, Jose L. McFaline-Figueroa, Jonathan S. Packer, Lena Christiansen, Frank J. Steemers, Andrew C. Adey, Cole Trapnell, and Jay Shendure. Joint profiling of chromatin accessibility and gene expression in thousands of single cells. *Science*, 361(6409):1380–1385, September 2018.

[115] Daniel Kalb, Huy D. Vo, Samantha Adikari, Elizabeth Hong-Geller, Brian Munsky, and James Werner. Visualization and modeling of inhibition of IL-1β and TNF-α mRNA transcription at the single-cell level. *Scientific Reports*, 11(1):13692, July 2021.

[116] Ioannis Lestas, Johan Paulsson, Nicholas E. Ross, and Glenn Vinnicombe. Noise in gene regulatory networks. *IEEE Transactions on Automatic Control*, 53(SPECIAL ISSUE):189–200, 2008.

[117] Nikolay Tsanov, Aubin Samacoits, Racha Chouaib, Abdel Meneem Traboulsi, Thierry Gostan, Christian Weber, Christophe Zimmer, Kazem Zibara, Thomas Walter, Marion Peter, Edouard Bertrand, and Florian Mueller. smiFISH and FISH-quant – a flexible single RNA detection approach with super-resolution capability. *Nucleic Acids Research*, 44(22):e165, December 2016.

[118] Arthur Imbert, Wei Ouyang, Adham Safieddine, Emeline Coleno, Christophe Zimmer, Edouard Bertrand, Thomas Walter, and Florian Mueller. FISH-quant v2: a scalable and modular tool for smFISH image analysis. *RNA*, 28(6):786–795, June 2022.

[119] Julie G. Donaldson. Immunofluorescence Staining. *Current Protocols in Cell Biology*, 69(1):4.3.1–4.3.7, December 2015.

[120] Nickolaus C. Lammer, Humza M. Ashraf, Daniella A. Ugay, Sabrina L. Spencer, Mary A. Allen, Robert T. Batey, and Deborah S. Wuttke. RNA binding by the glucocorticoid receptor attenuates dexamethasone-induced gene activation. *Scientific Reports 2023 13:1*, 13(1):1–15, June 2023. ISBN: 0123456789.

[121] Takamasa Kudo, Stevan Jeknić, Derek N Macklin, Sajia Akhter, Jacob J Hughey, Sergi Regot, and Markus W Covert. Live-cell measurements of kinase activity in single cells using translocation reporters. *Nature Protocols*, 13(1):155–169, January 2018.

[122] Taichiro Tomida, Mutsuhiro Takekawa, and Haruo Saito. Oscillation of p38 activity controls efficient pro-inflammatory gene expression. *Nature Communications 2015 6:1*, 6(1):1–9, September 2015.

[123] Brian Munsky and Mustafa Khammash. The finite state projection algorithm for the solution of the chemical master equation. *Journal of Chemical Physics*, 124(4):44104, January 2006.

[124] Lucy Ham, Megan A. Coomer, Kaan Öcal, Ramon Grima, and Michael P. H. Stumpf. A stochastic vs deterministic perspective on the timing of cellular events. *Nature Communications*, 15(1):5286, June 2024.

[125] Zachary R. Fox and Brian Munsky. The finite state projection based Fisher information matrix approach to estimate information and optimize single-cell experiments. *PLOS Computational Biology*, 15(1):e1006365, 2019. ISBN: 1111111111.

[126] Alex Popinga, Jack Forman, Dmitri Svetlov, Huy Vo, and Brian Munsky. The Stochastic System Identification Toolkit (SSIT) to model, fit, predict, and design experiments. *bioRxiv*, 2026. _eprint: https://www.biorxiv.org/content/early/2026/03/08/2026.02.20.707039.full.pdf.

[127] Daphne Wei-Chen Chen, James T. Lynch, Constantinos Demonacos, Marija Krstic-Demonacos, and Jean Marc Schwartz. Quantitative analysis and modeling of glucocorticoid-controlled gene expression. *Pharmacogenomics*, 11(11):1545–1560, November 2010.

[128] Daphne Wei Chen Chen, Marija Krstic-Demonacos, and Jean Marc Schwartz. Modeling the mechanism of GR/c-Jun/Erg crosstalk in apoptosis of acute lymphoblastic leukemia. *Frontiers in Physiology*, 3 NOV:32341, November 2012.

[129] Christopher James Barry. Modelling the glucocorticoid receptor dimerisation cycle. Master's thesis, Stellenbosch University, 2017.

[130] Vivaswath S Ayyar, Debra C Dubois, Richard R Almon, and William J Jusko. Mechanistic Multi-Tissue Modeling of Glucocorticoid-Induced Leucine Zipper Regulation: Integrating Circadian Gene Expression with Receptor-Mediated Corticosteroid Pharmacodynamics. *THE JOURNAL OF PHARMACOLOGY AND EXPERIMENTAL THERAPEUTICS J Pharmacol Exp Ther*, 363:45–57, 2017.

[131] I. N. Lyapun, B. G. Andryukov, and M. P. Bynina. HeLa Cell Culture: Immortal Heritage of Henrietta Lacks. *Molecular Genetics, Microbiology and Virology*, 34(4):195–200, October 2019.

[132] Daniel R Larson, Christoph Fritzsch, Liang Sun, Xiuhau Meng, David S Lawrence, and Robert H Singer. Direct observation of frequency modulated transcription in single cells using light activation. *eLife*, 2:e00750, September 2013.

[133] Carmen R. Tchen, Joana R. S. Martins, Nasren Paktiawal, Roberta Perelli, Jeremy Saklatvala, and Andrew R. Clark. Glucocorticoid Regulation of Mouse and Human Dual Specificity Phosphatase 1 (DUSP1) Genes. *The Journal of Biological Chemistry*, 285(4):2642–2652, January 2010.

[134] Lauren E. Shipp, Joyce V. Lee, Chi Yi Yu, Miles Pufall, Pili Zhang, Donald K. Scott, and Jen Chywan Wang. Transcriptional Regulation of Human Dual Specificity Protein Phosphatase 1 (DUSP1) Gene by Glucocorticoids. *PLOS ONE*, 5(10):e13754, 2010.

[135] Maike M.K. Hansen, Winnie Y. Wen, Elena Ingerman, Brandon S. Razooky, Cassandra E. Thompson, Roy D. Dar, Charles W. Chin, Michael L. Simpson, and Leor S. Weinberger. A Post-Transcriptional Feedback Mechanism for Noise Suppression and Fate Stabilization. *Cell*, 173(7):1609–1621.e15, June 2018.

[136] Kathleen Smoak and John A. Cidlowski. Glucocorticoids Regulate Tristetraprolin Synthesis and Posttranscriptionally Regulate Tumor Necrosis Factor Alpha Inflammatory Signaling. *Molecular and Cellular Biology*, 26(23):9126–9135, December 2006.

[137] Faoud T Ishmael, Xi Fang, Maria Rosaria Galdiero, Ulus Atasoy, William F C Rigby, Myriam Gorospe, Chris Cheadle, and Cristiana Stellato. Role of the RNA-Binding Protein Tristetraprolin in Glucocorticoid-Mediated Gene Regulation. *The Journal of Immunology*, 180(12):8342–8353, June 2008.

[138] Denis V Titov, Benjamin Gilman, Qing-Li He, Shridhar Bhat, Woon-Kai Low, Yongjun Dang, Michael Smeaton, Arnold L Demain, Paul S Miller, Jennifer F Kugel, James A Goodrich, and Jun O Liu. XPB, a subunit of TFIIH, is a target of the natural product triptolide. *Nature Chemical Biology*, 7(3):182–188, March 2011.

[139] Chanel Avenant, Katharina Ronacher, Elisabeth Stubsrud, Ann Louw, and Janet P. Hapgood. Role of ligand-dependent GR phosphorylation and half-life in determination of ligand-specific transcriptional activity. *Molecular and Cellular Endocrinology*, 327(1):72–88, October 2010.

[140] Carsen Stringer, Tim Wang, Michalis Michaelos, and Marius Pachitariu. Cellpose: a generalist algorithm for cellular segmentation. *Nature Methods 2020 18:1*, 18(1):100–106, December 2020.

[141] Daniel T Gillespie. A general method for numerically simulating the stochastic time evolution of coupled chemical reactions. *Journal of Computational Physics*, 22(4):403–434, December 1976.

[142] Tatsuya Morisaki, Kenneth Lyon, Keith F. DeLuca, Jennifer G. DeLuca, Brian P. English, Zhengjian Zhang, Luke D. Lavis, Jonathan B. Grimm, Sarada Viswanathan, Loren L. Looger, Timothee Lionnet, and Timothy J. Stasevich. Real-time quantification of single RNA translation dynamics in living cells. *Science*, 352(6292):1425–1429, June 2016.

[143] William S. Raymond, Sadaf Ghaffari, Luis U. Aguilera, Eric Ron, Tatsuya Morisaki, Zachary R. Fox, Michael P. May, Timothy J. Stasevich, and Brian Munsky. Using mechanistic models and machine learning to design single-color multiplexed nascent chain tracking experiments. *Frontiers in Cell and Developmental Biology*, 11:1151318, May 2023.

[144] Ivana Horvathova, Franka Voigt, Anna V. Kotrys, Yinxiu Zhan, Caroline G. Artus-Revel, Jan Eglinger, Michael B. Stadler, Luca Giorgetti, and Jeffrey A. Chao. The Dynamics of mRNA Turnover Revealed by Single-Molecule Imaging in Single Cells. *Molecular Cell*, 68(3):615–625.e9, November 2017.